A TEST RIG TO MEASURE THE STATIC LOAD PERFORMANCE OF A WATER LUBRICATED THRUST BEARING

A Thesis

by

MICHAEL ALAN ROHMER

Submitted to the Office of Graduate and Professional Studies of
Texas A&M University
in partial fulfillment of the requirements for the degree of

MASTER OF SCIENCE

Chair of Committee, Luis San Andrés
Committee Members, Yong-Joe Kim
Stefan Hurlebaus
Head of Department, Andreas Polycarpou

December 2015

Major Subject: Mechanical Engineering

ABSTRACT

A thrust bearing test rig experienced a catastrophic failure while operating with gas bearings. After many repairs, the test rig is in operating condition with water-lubricated bearings. Previous work details the failure and several initial repairs and modifications. Further modifications include manufacturing two rotors, repairing the main housing, aligning the motor shaft and test rotor, upgrading the water pipeline system, developing a static load system, installing instrumentation, and developing means of data acquisition. Presently, the revamped system has rotated to a speed of 5 krpm.

Measurements of the free-free mode natural frequencies and lateral mode shapes of the rotor-coupling system show that the rotor and quill shaft operate as a unit. Once assembled, water lubricates the bearings to lift and support the test rotor connected to the motor through its coupling. Impact loads identify the system fundamental natural frequency and damping ratio for operation without rotor speed or active thrust bearings. The flexibility of the quill shaft commands the location of the system lateral natural frequency (~ 93 Hz) and its low damping ratio. XLTRC^2® based predictions agree well with the measured natural frequency and identified damping ratio. The water lubricates the radial bearings to lift the test rotor again as the motor accelerates the rotor to 5 krpm. During this operation, the rotor motion is synchronous and does not excite the first natural frequency. While operating at speeds up to 5 krpm, the system did not reach its first critical speed.

Measurements show the thrust bearing axial clearance increases as the water supply pressure increases, max. 4.14 bar(g), for operation with a constant axial load and at null

or low rotor speed (3 krpm). As the imposed axial load increases, the operating clearance decreases exponentially. The decreasing operating clearance causes an increased flow resistance across the film lands, resulting in a reduced flow rate. As the flow rate decreases, there is a lower pressure drop across each orifice, resulting in an increase in recess pressure. The derived axial stiffness increases as the axial clearance decreases or the water supply pressure increases.

XLHydroThrust® uses the thrust bearing geometry to generate predictions of thrust bearing performance. The predictions accurately describe the influence of the load and supply pressure on the thrust bearing performance; however, there are discrepancies between the magnitudes of the predictions and the magnitudes of the measurements at a high axial load (low axial clearance). The average percent difference between the predicted and measured magnitudes of supply flow rate, flow rate through inner diameter, axial clearance, and recess pressure ratio change from 2% to 47%, 7% to 73%, 25% to 53%, and 7% to 18%, respectively, as the applied axial load increases from its minimum to maximum magnitude. Thus, there is a significant increase in difference between the predicted and measured magnitudes as the applied axial load increases.

Future work includes measurements of static and dynamic load performance of a water lubricated hybrid thrust bearing.

DEDICATION

I thank Dr. San Andrés for giving me the opportunity to work in the Turbomachinery Laboratory and for his countless efforts to make of me a better engineer. I also thank Mr. Scott Wilkinson, Mr. Giovanni Pallini, Mr. Maxime Deslandes, Mr. Travis Cable, Mr. Sung-Hwa Jeung, Mr. Josh Norsworthy, and other coworkers at the Turbomachinery Laboratory for their assistance and encouragement. Finally, I thank my family and fiancé, Amy Bolin, for their support and patience.

NOMENCLATURE

δ	Tilt of thrust collar
R_{out}	Thrust collar outer radius
T	Temperature
ω	Rotor speed
P_a	Ambient pressure
W	Load
L	Journal bearing length
D	Journal bearing diameter
P_S	Water supply pressure
K	Stiffness
R	Radius
C	Axial clearance
C_0	Axial clearance at center of thrust bearing
δ_X	Tilt of thrust collar about *X*-axis
δ_Y	Tilt of thrust collar about *Y*-axis
P_R	Recess pressure
D_{in}	Thrust bearing inner diameter
D_{out}	Thrust bearing outer diameter
D_{orif}	Orifice diameter
A	Thrust bearing area
Q_S	Supply flow rate

Q_{ID}	Flow rate through inner diameter
Re_{ID}	Reynolds number of flow through inner diameter
Re_{OD}	Reynolds number of flow through outer diameter
ρ	Fluid density
μ	Fluid viscosity
Q_{OD}	Flow rate through outer diameter
Q_O	Flow rate through orifice
$N_{pockets}$	Number of pockets
C_d	Empirical discharge coefficient

TABLE OF CONTENTS

Page

LIST OF TABLES

Page

LIST OF FIGURES

Page

INTRODUCTION

In rotating machinery, thrust bearings support axial loads and control shaft position. In turbomachinery, such as centrifugal compressors, axial loads depend on shaft speed, gas composition and physical properties, and operating pressure. The prediction of (impeller shroud) axial loads is largely empirical, creating the need for reliable thrust bearings [1]. To enhance thrust bearing technology, the Texas A&M Turbomachinery Laboratory, funded by USAF (2006-2009), designed and built a thrust bearing test rig to measure the forced performance of water-lubricated thrust bearings operating at high supply pressure and high rotational speed [2]. The measurements from the test hybrid thrust bearings exhibited remarkable correlation with results from a predictive tool [3].

In 2013, the thrust bearing test rig, modified to operate with air lubricated radial bearings, experienced large amplitude vibrations leading to severe damage with loss of parts [4]. The test rig, currently fully revamped to operate with water as a lubricant, will provide reliable experimental results for various types of thrust bearings.

This thesis provides a brief literature review on hydrostatic thrust bearings, a description of the revamping process of the test rig, and measurements made with the test rig during its preliminary operation. As work continues, the test rig will be used to measure the static and dynamic performance of a water lubricated hybrid thrust bearing; and in the future, other thrust bearing types and face seals.

A REVIEW OF HYDROSTATIC THRUST BEARINGS

Background

Hybrid (hydrostatic/hydrodynamic) thrust bearings (HTBs) are common in rotating machinery applications that require a high centering stiffness and accurate rotor positioning, such as precision machine tools, gyroscopes, telescopes, process fluid pumps, and other turbomachinery including cryogenic turbo pumps [5]. HTBs use an externally pressurized fluid to support (without contact) an axial load whereas hydrodynamic thrust bearings rely on shaft rotational speed to generate a hydrodynamic pressure supporting the load. Some other advantages of HTBs include a high load capacity, high damping coefficients, and no contact of bearing surfaces at low surface speeds. The load capacity, stiffness, and damping coefficients of a HTB depend on the lubricant supply pressure and the thrust collar rotational speed. Therefore, if more stiffness or load capacity are required, the supply pressure could be increased (at the expense of an increase in flow rate).

Principle of Operation of a Hydrostatic Bearing

Rowe (1983) [6] describes the principle of operation of hydrostatic bearings. The fluid flow in a hydrostatic bearing overcomes two modes of flow resistance: first, the lubricant flows through a flow restrictor (orifice, capillary, constant flow valve) before coming into a recess, then it flows from the recess across a small clearance film land region. As the clearance decreases, the flow rate reduces, thus reducing the frictional head loss through the orifice. Hence, the recess pressure increases, albeit never to exceed the supply pressure (with the exception of a hydrodynamic pressure in a shallow pocket). As the recess pressure increases, the fluid pressure generates a higher reaction load between the rotor

and bearing causing them to separate. Contrarily, if the axial clearance increases, the flow rate and pressure drop through the orifice also increase causing the recess pressure to decrease. As the recess pressure decreases, the fluid pressure generates a lower reaction load between the rotor and bearing causing the rotor move toward the bearing. It is by this means that a hydrostatic bearing generates a stiffness.

Effects of Geometry and Flow Restriction Type on HTB Performance

The geometry of the recess and the compensating flow element (orifice, capillary, constant flow valve) largely influence the performance of HTBs. Figure 1 shows four common HTB geometries. Sternlicht and Elwell (1960) [7] derive closed form design equations for the flow rate and load capacity of a single circular recess HTB and an annular multi-recess HTB, verifying their accuracy against experimental results. The authors test both a single circular recess HTB and an annular HTB (4 recesses) using various means of flow restriction. The annular HTB has a much higher load capacity and stiffness than the single recess HTB at the same pocket pressure. HTBs with a capillary restriction have the lowest stiffness while HTBs with a constant flow restriction have the highest stiffness. Also, HTBs with a capillary restriction have a load capacity and stiffness that are independent of fluid viscosity, whereas HTBs with a constant flow rate restriction have a load capacity and stiffness that are independent of supply pressure. However, once the HTB with a constant flow restriction begins to exceed its maximum specific load (load/area), the bearing stiffness experiences a sharp cut off where it drops from its peak magnitude to zero.

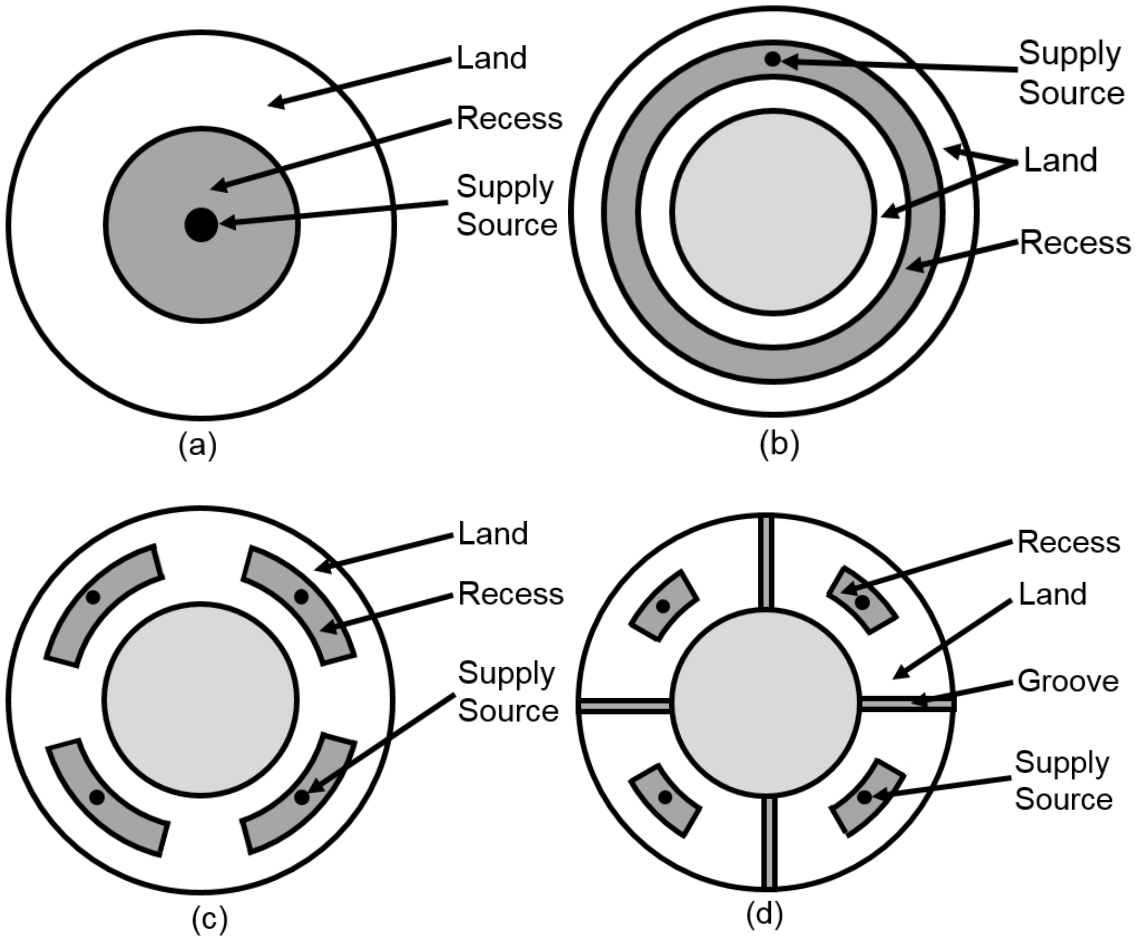

Figure 1. Common recess geometries in HTBs, including: (a) single circular recess thrust bearing, (b) annular groove thrust bearing, (c) annular multi-recess thrust bearing, and (d) multi-pad thrust bearing.

Rowe (1983) [6] calculates the load and flow rate for an incompressible fluid lubricated HTB; analytically for simple geometries such as the single circular recess HTB, and computationally for complex geometries. Rowe [6] shows annular groove HTBs demand a higher flow rate and provide a higher load capacity than a single circular recess HTB. Multi-recess HTBs have a similar load capacity and flow rate as an annular groove

HTB. The multiple recess HTB produces a restoring torque when the rotor and bearing surfaces are not parallel.

Gas Thrust Bearings

Fourka and Bonis (1997) [8] compare the performance of gas HTBs with five types of flow restrictors: recess containing an orifice, inherent type orifice (no recess), multiple inherent type orifices, a porous wall, and porous resistance (porous cylindrical plugs in multiple orifices). The authors seek to use multiple inherent type orifices to achieve the load capacity of a gas HTB with an orifice within a recess while avoiding pneumatic hammer. As the number of inherent type orifices increases, the load capacity increases and the maximum stiffness occurs at a larger film clearance. For a test bearing configuration with 8 to 12 inherent type orifices, the gas HTB achieves its maximum stiffness while only requiring a moderate flow rate. The HTB also achieves the highest stiffness when the inherent type orifices are located at a radius equal to 2/3 of the bearing outer radius. A porous bearing has the highest load capacity followed by the HTB with a recess containing an orifice. However, as the film clearance increases, the load capacity of the HTB with a recess containing an orifice decreases sharply causing it to only be greater than the load capacity of the thrust bearing with the inherent orifices at minute film clearance. The maximum stiffness and required flow rate are lower for the HTB with inherent type orifices than they are for a HTB with a recess containing an orifice; but as the film clearance increases, a HTB with inherent type orifices has a higher stiffness, offering a larger range of clearances for the HTB.

Belforte et. al. (2010) [9] test annular groove HTBs with various recess depth (0, 10, and 20 μm) and operating without shaft rotation. The authors find, that as the recess depth increases, the bearing load capacity, stiffness, and flow rate all increase. Also, the stiffness increases as the supply pressure and feed orifice diameter increase. The maximum stiffness occurs with large recess groove depth at low clearance (10 μm). As the depth of the groove increases, the test rotor-bearing damping ratio decreases and even becomes negative, thus exhibiting unstable behavior. The test rotor-bearing system damping ratio also decreases as the supply pressure increases. The oscillating damped frequency increases with supply pressure and the depth of the annular groove due to the increased stiffness. At large recess depth (20 μm) and high supply pressure (0.82 MPa), the gas HTBs encounter air hammer, a self-excited vibration caused by compressibility of a gas volume trapped the recess. The hammer frequency increases as the supply pressure increases.

High Performance Thrust Bearings for High Speed Applications

Cryogenic fluid turbo pumps operate with high shaft speed and a large pressure difference. A feasible method of rotor support is to implement hybrid (hydrostatic/hydrodynamic) fluid bearings. Hybrid fluid bearings offer an economically attractive and reusable alternative to ultra-precision ceramic ball bearings, as they have no surface speed limitation or *DN* (diameter x rotor speed) limit. The advantages of hybrid bearings enable a turbo pump to be smaller, lighter, and operating with an increase in mechanical efficiency. The following references present test data to validate the performance of high-speed, high-pressure HTBs [10].

San Andrés (2000) [10] performs a bulk-flow analysis to predict the performance of a multi-recess, orifice-compensated, angled injection HTB. The application relates to cryogenic fluid turbo pumps that experience a high shaft speed (180 krpm) and a large pressure difference (550 bar). As the applied load increases, the film clearance decreases causing a decrease in flow rate and increase in recess pressure. The stiffness coefficient has an optimum value when there is a 40% pressure drop across the orifice (recess pressure is 60% of supply pressure). The damping coefficient increases as the clearance decreases or the rotational speed increases while the drag torque increases with either rotational speed or clearance. At high rotor speed and low load, centrifugal flow fluid inertia plays a significant role as it may cause fluid starvation through the bearing inner diameter and suction pressures just downstream of the edge of the recesses. The model accounting for fluid inertia at both the recesses and the film lands shows a higher damping coefficient and a lower dynamic stiffness coefficient than the model only accounting for fluid inertia at the recesses. Fluid inertia on the bearing film land has a large effect on the bearing performance characteristics.

San Andrés (2002) [11] follows with a computational analysis to predict the performance of HTBs with angular misalignment for cryogenic fluid turbo pumps operating at a rotor speed of 180 krpm ($\mathrm{Re}_C = \rho_S \Omega R_{out} C / \mu_S = 33{,}000$) where ρ_S and μ_S are the fluid density and viscosity, Ω is the shaft rotational speed, R_{out} is the bearing outer radius, and C is the nominal axial film clearance). The static and dynamic axial stiffness as well as the static and dynamic moment-angle stiffness coefficients have a peak magnitude when the recess pressure ratio is approximately 0.6. The axial damping

coefficient, the direct moment-tilt angle damping coefficient, and the cross-coupled moment stiffness coefficients slightly increase with load for low to moderate load and then increase rapidly with load for large load due to the large hydrodynamic effect at low clearance. As the misalignment angle increases, variations in recess pressure and film pressure increase, causing the overall mass flow to decrease as less flow exits through the inner diameter. In addition, both moment angle and force axial stiffness coefficients increase as the misalignment angle increases. However, the axial force and the drag torque are largely independent of the collar misalignment angle. The whirl frequency ratio (for conical rotor motions) is equal to 0.5, thus showing HTBs do not offer any added stability when compared to hydrodynamic thrust bearings.

Forsberg (2008) [2] designs and builds a test rig for water-lubricated HTBs and conducts tests with a non-rotating, HTB (8 pockets) operating with a supply pressure ranging from 3.45 bar to 17.24 bar. Figure 2 shows a cross-sectional view of the test rig, with two-flexure pivot, tilting pad radial hydrostatic bearings supporting the test rotor. The test rig uses two HTBs; a test thrust bearing and a slave thrust bearing. Both face the outer side of the thrust collars of the rotor. The slave thrust bearing is affixed rigidly to a bearing support, as shown on the right of Figure 2. A shaker delivers an axial load (static and/or dynamic) to the test thrust bearing through a non-rotating load shaft. Two aerostatic radial bearings support the axial load shaft with minimal friction for controlled displacement along the axial direction. The test thrust bearing, depicted at the center of Figure 2, moves axially to impose a load on the rotor thrust collar. The slave thrust bearing reacts to the imposed axial load [12].

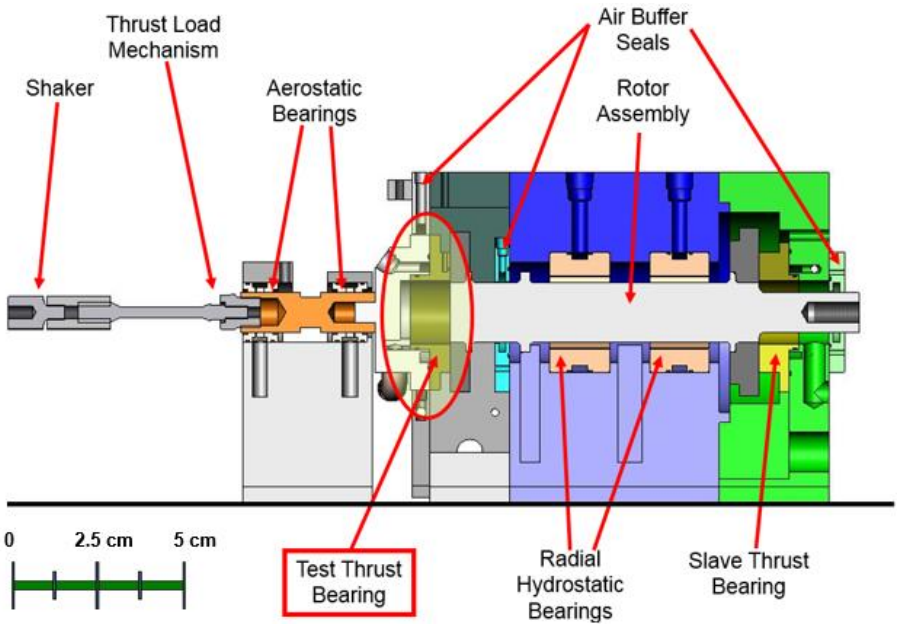

Figure 2. Cross sectional view of thrust bearing test rig. Reprinted from [12].

Forsberg [2] finds that the fluid supply pressure has a small influence on the pocket pressure ratio (ratio of pocket pressure to supply pressure). However, the pocket pressure ratio decreases significantly as the operating clearance increases (due to a smaller load) because the lubricant experiences a higher flow rate leading to a higher pressure drop across the orifice. As the supply pressure increases or the clearance decreases, the HTB develops higher pocket pressures that lead to a higher load capacity and stiffness. Most importantly, the flow rates exiting the bearing through the inner diameter and at the outer diameter are different, which could cause fluid starvation with shaft rotation. The predictions, based on a model in Ref. [11], for both the flow and load agree with measured data within 20%. However, larger discrepancies exist between the predictions and

measurements of axial stiffness because of persistent misalignment of the thrust collar faces.

Ramirez (2008) [13] continues Forsberg's work to test a water-lubricated, 8 pocket HTB (8 pockets) operating at a rotor speed ranging from 7.5 krpm to 17.5 krpm and with a supply pressure ranging from 3.45 bar to 17.24 bar. The rotor speed does not have a large effect on the bearing static stiffness or load capacity, indicating a primarily hydrostatic operation. Similar to the non-rotating condition [1], both the load and the static axial stiffness increase as either the supply pressure increases or the clearance decreases due to the higher recess pressure. Flow rate measurements through the inner diameter show the onset of fluid starvation at high rotor speed and low load due to centrifugal fluid flow acceleration. The measurements of inlet flow rate, discharge flow rate through the inner diameter, load capacity, and recess pressure ratio (ratio of recess pressure to supply pressure) differ from predictions by 1%, 5%, 7%, and 10%, respectively.

Esser (2010) [3] continues performing tests to determine the effect of orifice diameter (1.67 mm, 1.80 mm, 1.93 mm) on the performance of a water lubricated, eight pocket HTB. To this end, Esser conducts tests with the bearing operating at a rotor speed varying from 7.5 krpm to 17.5 krpm, and a supply pressure ranging from 3.45 bar to 17.24 bar. At a given load and supply pressure, the HTB experiences an increase in stiffness and enlarged operating clearance as the orifice diameter increases. While operating at a constant supply pressure, larger orifice diameter and clearance cause the supply flow rate and the exhaust flow rate through the inner diameter to increase, thus mitigating fluid starvation on the bearing inner side. When the orifice diameter increases from 1.80 mm to

1.93 mm, the thrust bearing experiences limited gains in operating clearance and axial stiffness but still requires a much higher flow rate. Overall, the predictions correlate well with measured inlet flow rate, discharge flow rate through the inner diameter, recess pressure, clearance, and axial stiffness coefficient.

San Andrés *et.* al. (2008) [12] report on the test and predictions for the performance of a HTB operating at a rotor speed of 17.5 krpm (surface speed=50 m/s) and a water lubricant supply pressure of 1.72 MPa. At a constant rotor speed, an increase in load or decrease in supply pressure causes a reduction in film clearance and flow rate. On the other hand, with a constant supply pressure, the rotor speed has little influence on the operating clearance. As the rotor speed increases and the bearing supply pressure decreases, less lubricant flows out through the inner diameter of the thrust bearing causing lubricant starvation. Most importantly, with a rotor spinning, while the thrust bearing operates at a constant supply pressure and rotor speed, the discharge flow rate through the inner diameter rapidly decreases when the load decreases (axial clearance increases) due to centrifugal flow effects. Overall, the predictive tool estimates well the inlet flow rate, exhaust flow rate through the inner diameter, load, and film clearance when compared to measured data recorded for increasing load.

REVAMPING THE THRUST BEARING TEST RIG

Appendix A gives a full description of the thrust bearing test rig. Rohmer and San Andrés in a technical report (2014) [4] describe the failure of the test rig when operating with air bearings, as well as initial component repairs or replacements such as coating the original rotor surface, replacing the journal bearings, removing the damaged surface of the slave thrust bearing, and modifying the air buffer seals. Ref. [4] also details the installation of a water supply system to regulate and measure the pressure and flow rate of the water supplied to the radial and axial bearings.

This section describes additional repairs and modifications such as:

- Determining the orthogonality of the thrust collar faces on the original rotor.
- Repairing damaged fastener connections on the housing and air buffer seals.
- Enlarging the pipe diameter of the water manifold.
- Aligning the rotor centerline with the motor shaft centerline.
- Designing a static load system.
- Installing instrumentation and developing means of data acquisition.

Rotor

A 75-μm thick hard chrome coating resurfaces the original rotor surface damaged during the failure [1]. However, the thrust collar faces appear not to be orthogonal with the centerline of the shaft. A simple apparatus helps to gain insight to the severity of the misalignment. Figure 3 shows the original rotor resting on a V-block (precision machining equipment for machining angles); three eddy current sensors face a thrust collar to measure the relative axial displacement at three circumferential locations; and hence, aid

to determine the collar planar orientation relative to the rotor main axis of rotation. Two eddy current sensors face the rotor and measure the lateral displacement at two locations to determine its axis of rotation. The rotor slowly rotates (by hand) to twelve angular positions, at which the eddy current sensors measure the distance to the test thrust collar. The ad-hoc apparatus does not impose an axial restraint that could prevent the gap between the thrust collar and the three eddy current sensors from changing. The measurement only concerns with the relative axial displacement at various circumferential positions to determine the relative planar orientation (tilt about *X* and *Y* axes).

Figure 4 shows the tilt (slope in mm/m) of the test thrust collar about the *X* and *Y* axes vs. angular position. The graph includes the axial slope of the shaft, which, found to be a constant, shows the V-block effectively restrains the rotor from laterally translating while rotating. In Figure 4, the tilt about the *Y*-axis trails the tilt about the *X*-axis by 90° but has equal amplitude (demonstrated by a 90° phase shift of the data in Figure 4). The tilt (δ) of the test thrust collar has a peak-to-peak amplitude of nearly 3 mm/m resulting in a peak-to-peak deviation ($R_{out}\delta$) of 150 μm at the edge of the thrust collar (R_{out} = 5.1 cm). The data shows that the test thrust collar is not perpendicular with the centerline of the rotor, most likely the shaft bent during the failure incident.

The evidence of a bent shaft supported the decision to manufacture another rotor, shown in Figure 5. The new rotor, made entirely of stainless steel to prevent corrosion, has the same basic dimensions as the original rotor. Note that the rotor can be machined as one piece to tighter tolerances than the original rotor (Inconel thrust collars) because it is made of entirely of stainless steel and does not require any assembly. The rotor includes

some minor details for ease of manufacturing and installation, as well as holes (4 mm diameter) for insertion of setscrews that could act as imbalance masses, if needed. The new rotor did not undergo the same orthogonality inspection as it did not experience an event that might cause warping of the shaft. Presently, the newly manufactured rotor is installed in the test rig.

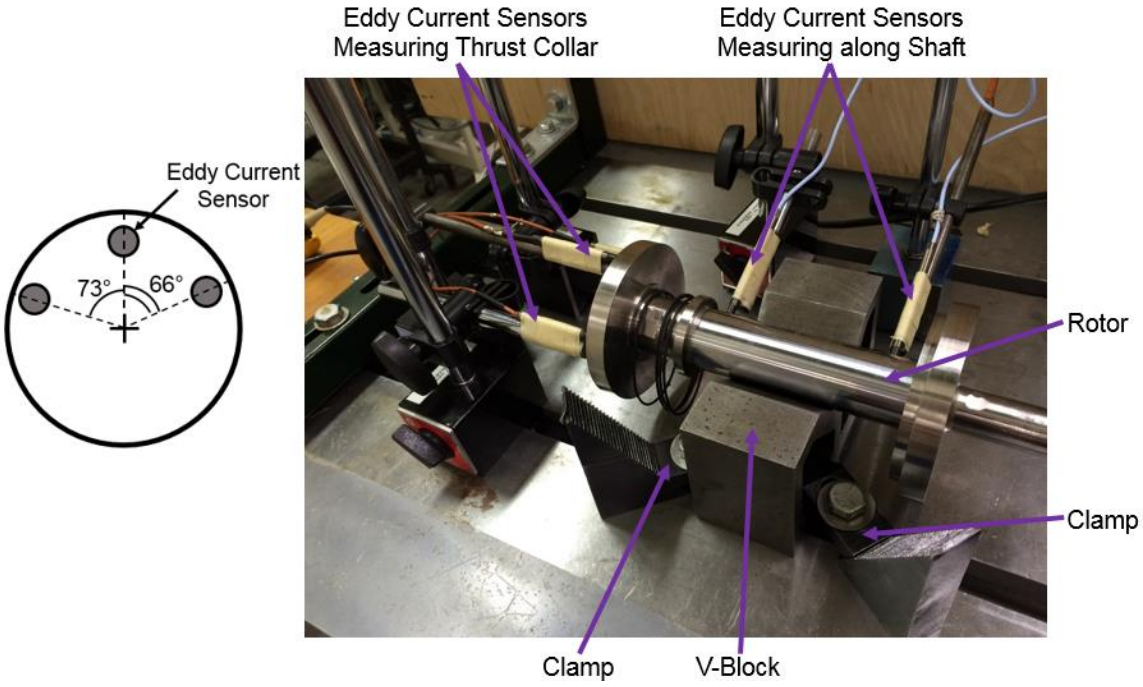

Figure 3. Photograph of rotor resting on a V-block. Three eddy current sensors measure the axial displacement of the test thrust collar at three different locations (shown on inset) to determine its planar orientation. Two eddy current sensors measure the lateral displacement of the shaft to determine its axial orientation.

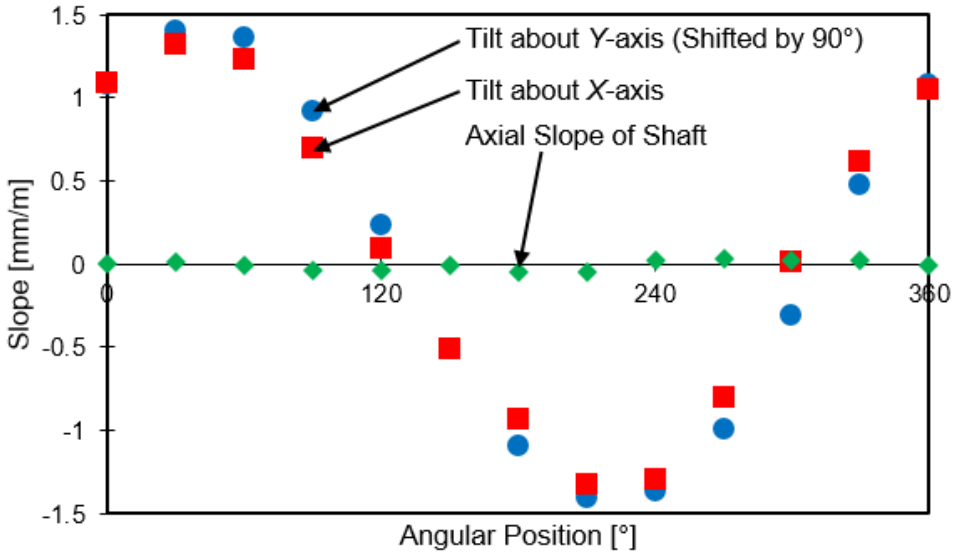

Figure 4. Tilt of the original rotor test thrust collar about the *X* and *Y* axes vs. angular position. The tilt about the *Y*-axis is shifted by 90°. Rotor supported on a V-block. Rotor overall length = 26 cm, thrust collar outer diameter= 10.2 cm.

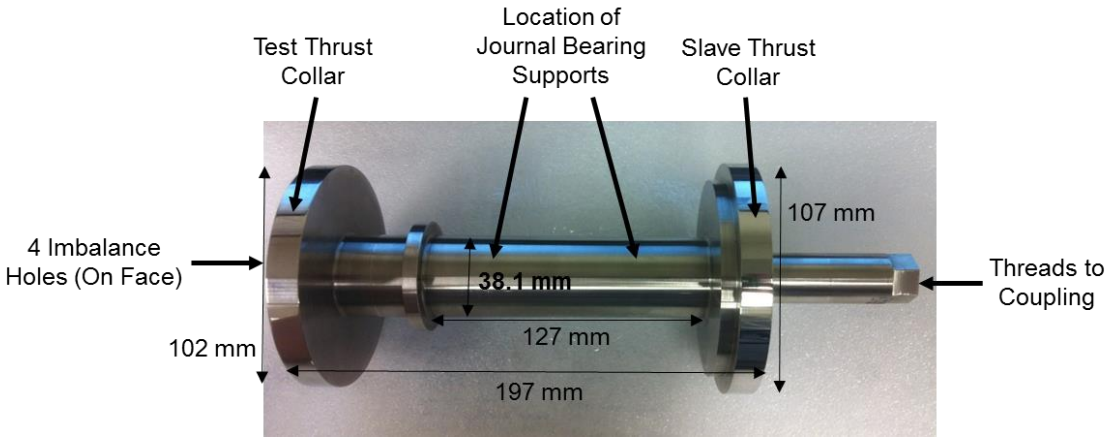

Figure 5. Photograph of manufactured rotor (2014).

Air Buffer Seals and Housing

A technical report (2014) [4] describes the repair of various individual components but does not address the damage to the housing that holds the air buffer seals and eddy

current sensors. Figure 6 shows a photograph of the housing with both an air buffer seal and an eddy current sensor installed. When the air buffer seals sheared off from the housing, the remnants of the bolts remained in the housing. In addition, the contact between the rotor and eddy current sensors induced large stresses on the threads of the housing that kept the eddy current sensors stationary. A drill/tap process removed the remnant material from the threaded holes.

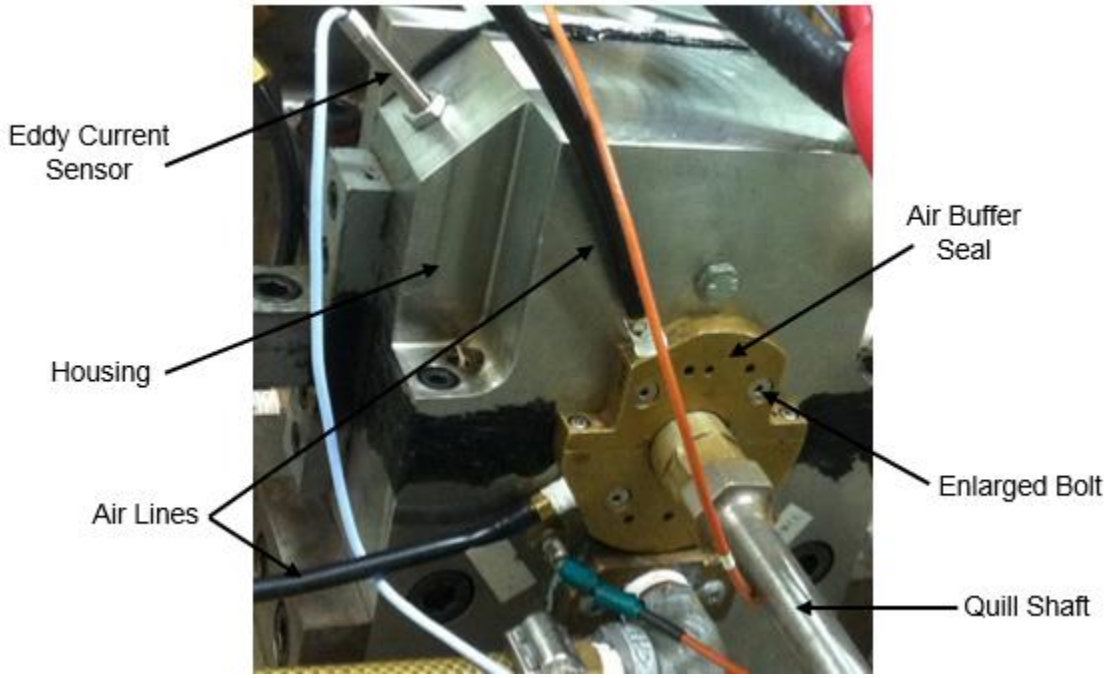

Figure 6. Photograph of air buffer seal and eddy current sensor attached to bearing housing (after repair in 2015).

Water Manifold

Ref. [4] describes the installation of a 6.4 mm (1/4 in.) diameter water manifold to deliver water to the bearings at a regulated pressure. The supply lines, shown in Figure 7,

caused a large pressure drop from the main (house water) delivery source to the supply pressure into the bearings. Fluid frictional losses in the original water manifold are especially apparent when the thrust bearings operate with a large axial clearance that demands of a large fluid flow rate.

Fluid frictional losses in a pipe are proportional to the fluid speed squared. At a constant fluid flow rate, the fluid velocity is inversely proportional to the area; therefore, fluid frictional losses decrease as pipe diameter increases. By increasing the pipe diameter to 19 mm (3/4 in.), the fluid velocity decreases to 11% of its original speed, and the fluid pressure loss across the water manifold drops to 1% of the loss associated with the original water manifold configuration. In order to mitigate frictional losses, evidenced by the significant pressure drop, the water delivery system to the bearings was increased to 19 mm (3/4 in.) pipe diameter, as depicted in Figure 8.

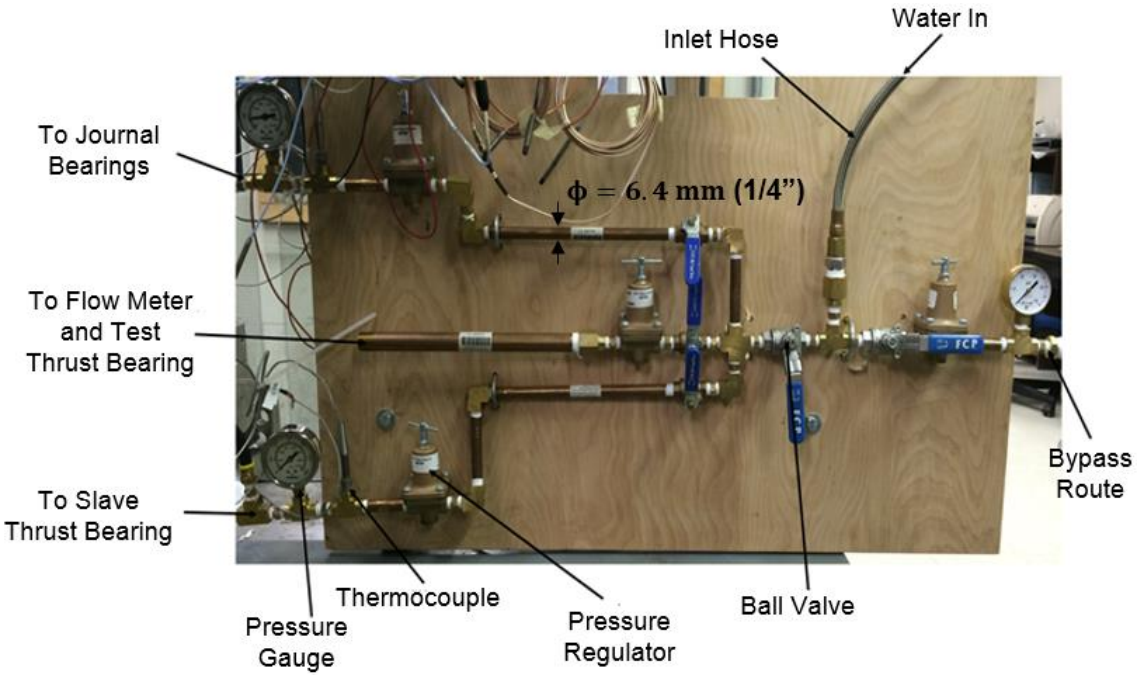

Figure 7. Photograph of original pipelines and manifold for water distribution to bearings (ϕ=6.4 mm [1/4 in.]).

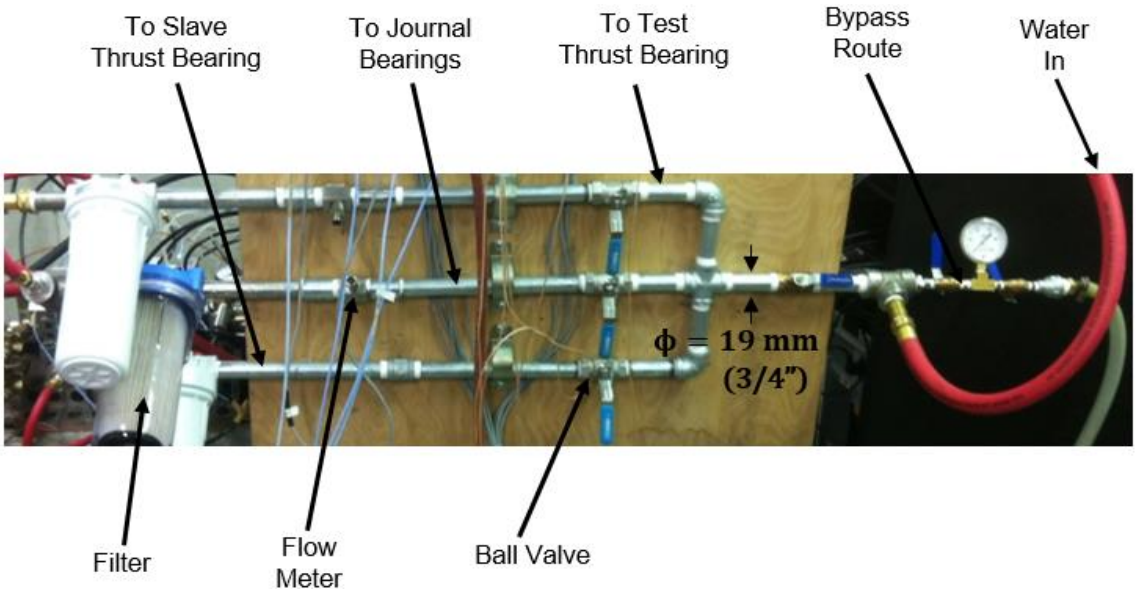

Figure 8. Photograph of modified pipelines and manifold for water distribution to bearings (ϕ=19 mm [3/4 in.]).

Test Rig Assembly

The quill shaft of the coupling threads into the rotor with an installation torque of 278 Nm as per the coupling manufacturer specification. With the quill shaft and rotor connected, the rotor rests on the bottom halves of the radial bearings. Next, the top and bottom halves of the radial bearings fasten to each other, and O-rings wrap around on the bearings' outer diameter. The top part of the journal bearing housing fastens to its bottom, and the slave and test thrust bearing housings fasten to the journal bearing housing to complete the test rig assembly. The test thrust bearing and load shaft make an integral assembly. This assembly slides on two aerostatic bearings that are secured to a pedestal. The quill shaft attaches to the remainder of the coupling, a diaphragm and hub that connect to the drive motor.

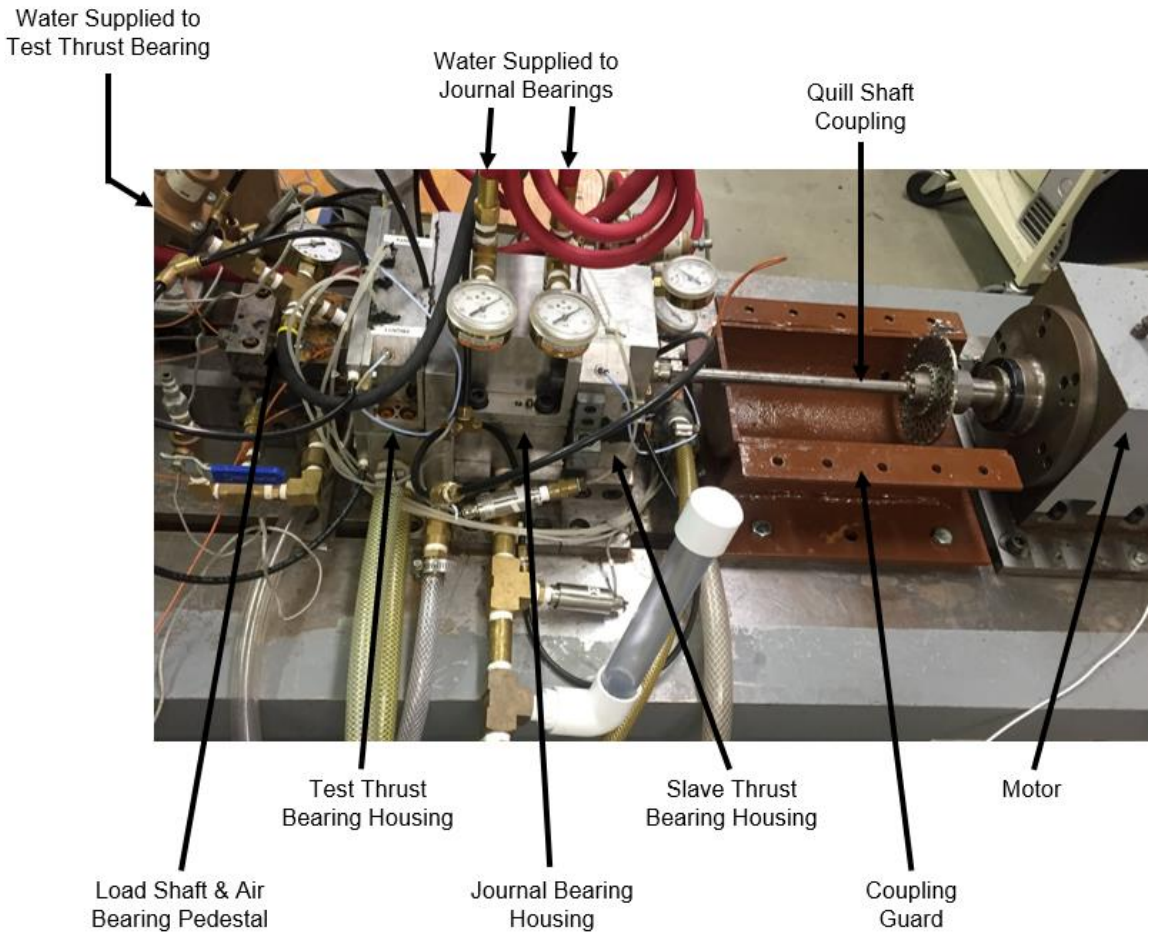

Figure 9. Photograph of the assembled test rig.

Alignment of Motor Shaft and Rotor

With the test rig fully assembled, water at the anticipated operating supply pressure (3.45 bar(g)) feeds the journal bearings and lifts the rotor. Figure 10 shows two tip displacement gauges, mounted on the motor shaft, indicating on the face and rim of the coupling quill shaft. The motor shaft and the rotor slowly turn together (by hand), and the gauges measure the relative displacement of the face and rim at both horizontal and

vertical directions. The displacements on the rim and face determine the offset misalignment and the angular misalignment, respectively. Next, a meticulous process displaces the housing to align the motor shaft centerline to the rotor centerline. Once both centerlines align within tolerance, water at various supply pressure (2 – 6 bar(g)) feeds the journal bearings to ensure the alignment remains within tolerance.

Equation (1) shows the alignment tolerance (A = 0.0105 cm/cm) between the rotor and motor shaft required for the coupling, as per manufacturer specifications,

$$\frac{x}{L} + \frac{y}{M} \leq A \tag{1}$$

Above, x is the total indicator reading on the rim, y is the total indicator reading on the face, M = 33.7 mm is the distance between indicator measurement and shaft centerline, L = 140 mm is the distance between hinge points (specified by coupling vendor), and A is the allowable angular misalignment.

Load System on Test Rig

The rig needs a load system capable of applying static and/or dynamic loads onto the thrust bearing. The electromagnetic shakers will only deliver a dynamic load, hence the need for a separate static load system. Figure 11 shows the static load system designed to allow for the superposition of both a static load and a dynamic load. A threaded rod applies a tensile force on a soft spring to rotate the tip of a bar pivoting about a fulcrum (pivot rod). The other end of the bar, amplifies the input load, pushes on a strain gauge load cell connected to the load shaft that holds the thrust bearing. The static load system allows space for a shaker to apply its dynamic load to the load shaft. Due to the stiffness and

elastic deformation limit of the (selected) spring, the static load system currently has a maximum load capacity of 900 N. However, the load capacity can increase, as needed.

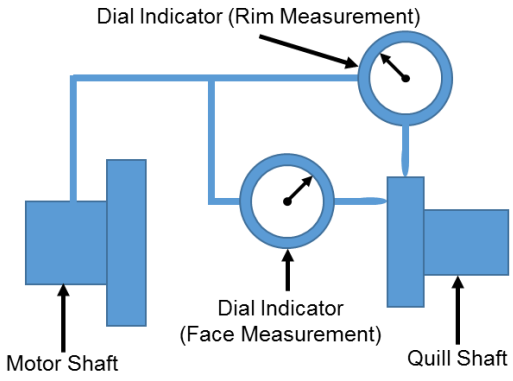

(a)

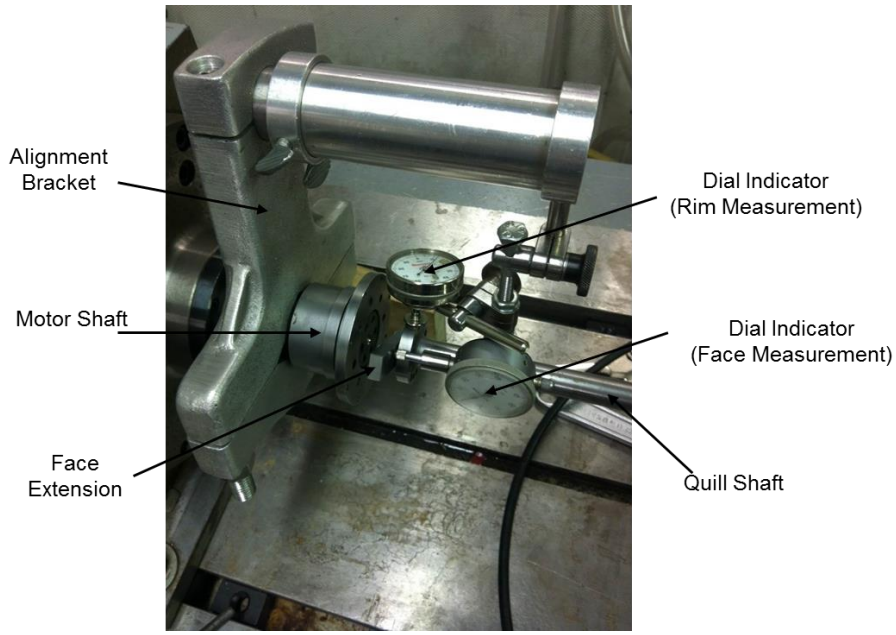

(b)

Figure 10. (a) Schematic view and (b) photograph of face and rim alignment method for aligning motor shaft and rotor/coupling quill shaft.

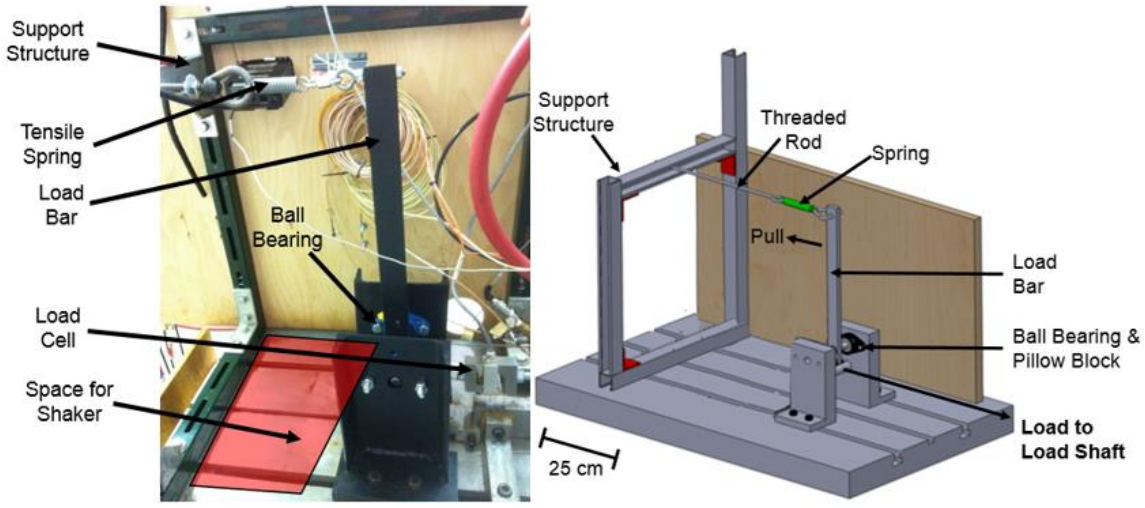

(a)

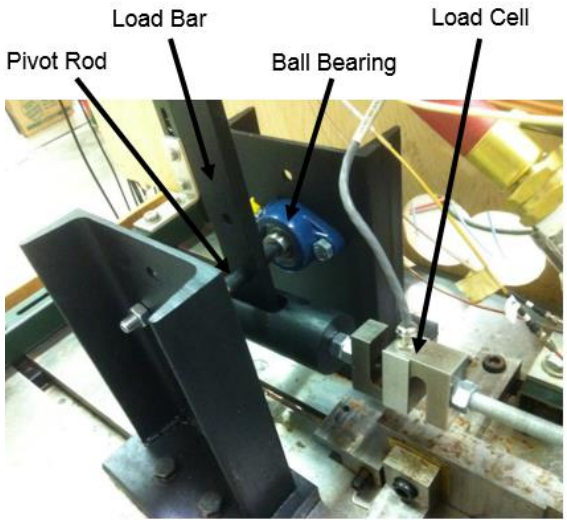

(b)

Figure 11. (a) Photograph and schematic view of static load system and (b) photograph of load mechanism.

Instrumentation and Data Acquisition

Table 1 shows the instrumentation presently installed on the thrust bearing test rig. Four eddy current sensors measure the lateral position (X,Y) of each thrust collar outer

diameter, and three (x 2) eddy current sensors measure the axial clearance of each thrust collar outer face at three angular locations relative to its respective bearing. Each eddy current sensor is calibrated to stainless steel, yielding a sensitivity of ~10.2 V/mm, different from the vendor specified sensitivity to 4140 steel (~7.9 V/mm). A signal conditioner removes the bias voltage from the eddy current sensors so that their output range is within the acceptable limits of the data acquisition (DAQ) system (±10V).

Table 1. Instrumentation on the thrust bearing test rig.

Sensor Type	Quantity	Range
Eddy Current Sensor	10	0 – 2 mm
Turbine Flow Meter	3	0.95 – 95 LPM
Static Pressure Transducer	7	0 – 20.7 bar
Strain Gauge Load Cell	1	0 – 2200 N
Optical Tachometer	1	0 – 250 krpm
K-Type Thermocouple	1	0 – 100 °C
Signal Conditioner	12	1-1000X, ±10 V
LabView cDAQ	16	±10 V
	8	0 – 20 mA

There are seven static pressure transducers (strain gauge type). Two sensors measure the water supply pressure into the journal bearings; two other sensors measure the supply pressure into each half of the slave thrust bearing; the fifth sensor records the supply pressure into the test TB; and the sixth and seventh sensors record the recess pressure in two pockets on the test TB. Individual turbine flow meters measure the supply flow rate into the journal bearings, the supply flow rate into the test TB, and the exhaust flow rate through the inner diameter of the test TB.

A thermocouple measures the temperature of the water supplied to the test thrust bearing. A strain gauge load cell records the load applied by the static load system onto the test TB. An optical tachometer measures the rotor speed. A LabView® program serves to acquire and record voltages and currents from the various instrumentation. Other available DAQ systems include signal analyzers, and a Bentley Nevada ADRE© system.

ROTOR-COUPLING FREE-FREE MODE NATURAL FREQUENCIES AND SHAPES

Prior work shows that the test rotor and the quill-shaft coupling operate as a single unit and must be considered as such for a sound rotordynamic analysis. Appendix B describes the set-up and procedure for measuring the free-free mode natural frequencies and mode shapes of the rotor-coupling assembly. Table 2 and Figure 12 show the first three measured and XLTRC^2 [14] predicted free-free mode natural frequencies and shapes of the rotor-coupling assembly. The predictions for the first two free-free mode shapes and natural frequencies are in close agreement with the test data.

Table 2. Measured and predicted free-free mode natural frequencies of rotor-coupling system.

	Measured Frequency [Hz]	Predicted Frequency [Hz]	Percent Difference
1st Free-Free Mode	104 ± 8	101	2.9
2nd Free-Free Mode	544 ± 8	555	2.0
3rd Free-Free Mode	1,280 ± 8	1,304	1.9

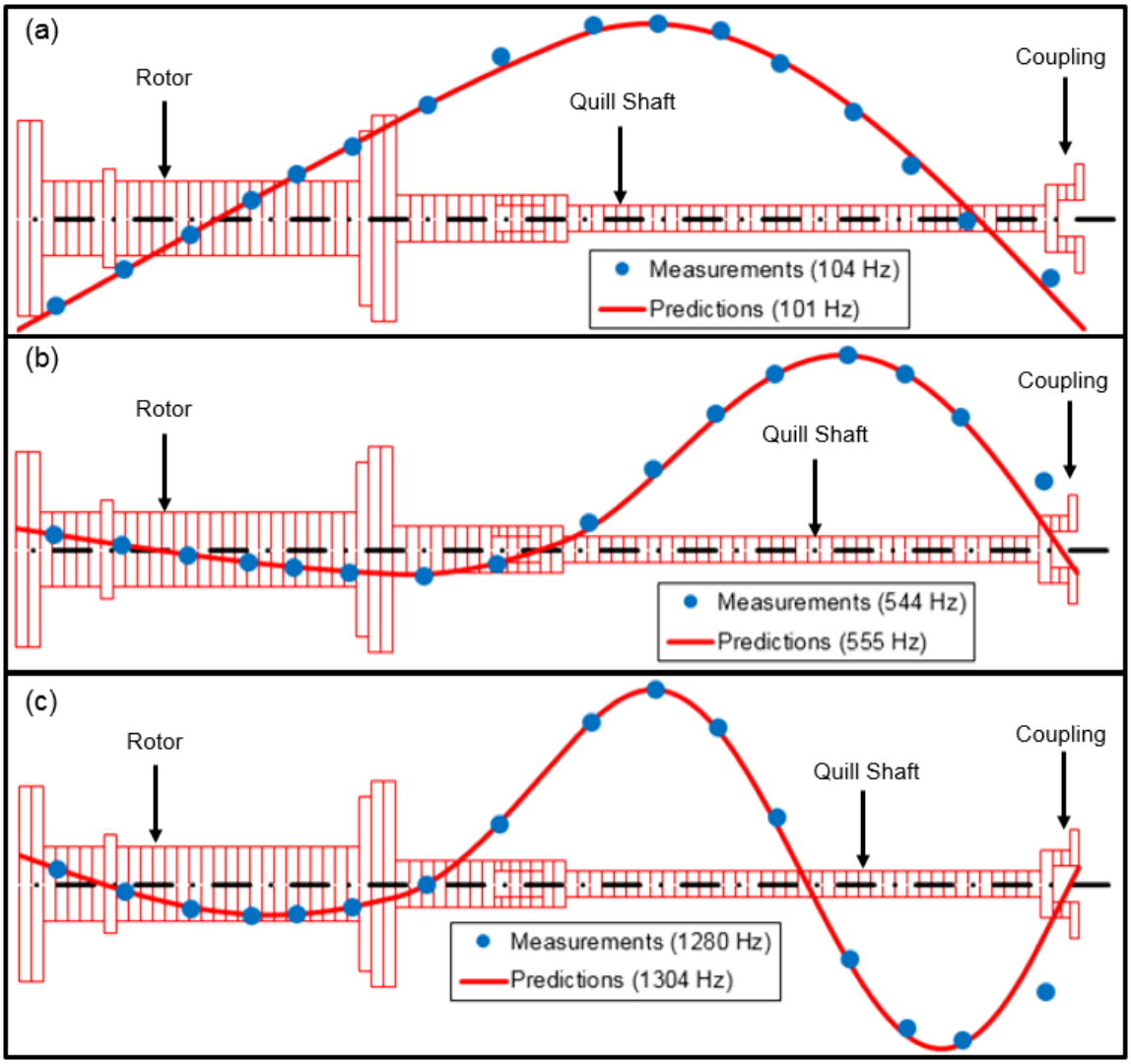

Figure 12. Measured and predicted (a) first, (b) second, and (c) third free-free mode shapes of the rotor-coupling system, respectively.

IMPACT LOAD TESTS ON ROTOR-COUPLING-BEARING SYSTEM OPERATING WITHOUT ROTOR SPEED

Apparatus and Procedure

With the rotor and coupling connected, water (24 °C) at 3.45 bar(g) supplies the hybrid journal bearings and lifts the rotor-coupling system without either thrust bearing active. An impact hammer strikes the center of the quill shaft, causing the rotor coupling system to vibrate at the (rotor-coupling-radial bearings) system fundamental natural frequency.

Pressure transducers and a turbine flow meter measure the (steady) supply pressure and flow rate into the journal bearings, respectively. Eddy current sensors measure the lateral displacement at each of the rotor thrust collars. A signal analyzer averages the displacement response in the frequency domain from 25 impacts. The frequency response and the half-power method aid to estimate the system natural frequency and damping ratio as the water supply delivered to the bearings increases in pressure and flow rate.

Flow Rate vs. Water Supply Pressure into Radial Bearings

Figure 13 shows the flow rate of the water delivered to both journal bearings vs. the water supply pressure into each journal bearing. The figure includes predictions from XLHydroJet® [15], which are in agreement with the measured flow rate, showing the flow to increase as the pressure supply into the bearings increases. Appendix C describes the input data required for XLHydoJet® [15] as well as the performance parameters that it predicts.

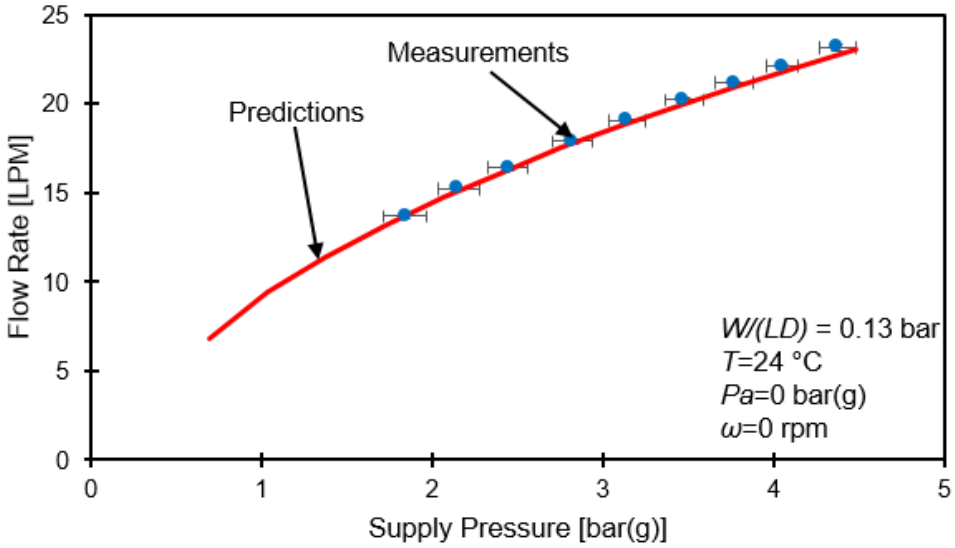

Figure 13. Measured and predicted water supply flow rate into both journal bearings vs. water supply pressure at room temperature (*T*=24 °C) for operation without rotor speed (ω). Ambient pressure (P_a) is 0 bar(g). Specific static load on each bearing (*W*/(*LD*)) = 0.13 bar.

Natural Frequency and Damping Ratio vs. Water Supply Pressure into Radial Bearings

Figure 14 shows the amplitude of rotor motion, normalized with respect to its peak amplitude, vs. frequency for operation with water (24 °C) supplied at 2.07, 3.45, and 4.83 bar(g) into the radial bearings. The ambient pressure is 0 bar(g). The lateral rotor displacement is recorded at the thrust collar on the opposite side of the motor. Recall the thrust bearings are not active.

Table 3 lists the hydrostatic journal bearing operating characteristics and force coefficients calculated using XLHydroJet® [15]. Figure 15 shows the predicted fundamental mode shape of the rotor-coupling assembly when water (24 °C) at 3.45 bar supplies the radial bearings. The inset table shows the relative amplitude and phase angle between measured displacements on each thrust collar corresponding to the predicted

mode shape. The fundamental mode shape shows the quill shaft bending while the rotor displaces as a rigid body in conical motion.

Figures 16 and 17 show the fundamental natural frequency and system damping ratio versus supply water pressure into the radial bearings. The natural frequency only increases slightly from 91 Hz to 95 Hz as the water lubricant supply pressure increases from 2 bar(g) to 6 bar(g) because the flexibility of the quill shaft controls the natural frequency. The damping ratio is rather low because the highly flexible quill shaft has no external damping. Nonetheless, the damping ratio increases from 4.8% ± 0.8% to 6.8% ± 0.7% as the water lubricant supply pressure increases from 2 bar(g) to 6 bar(g). Figures 16 and 17 also show XLTRC^2® structural model predictions obtained with bearing force coefficients supplied by XLHydrojet®, see Table 3.The predictions agree well with the measured natural frequency and identified damping ratio.

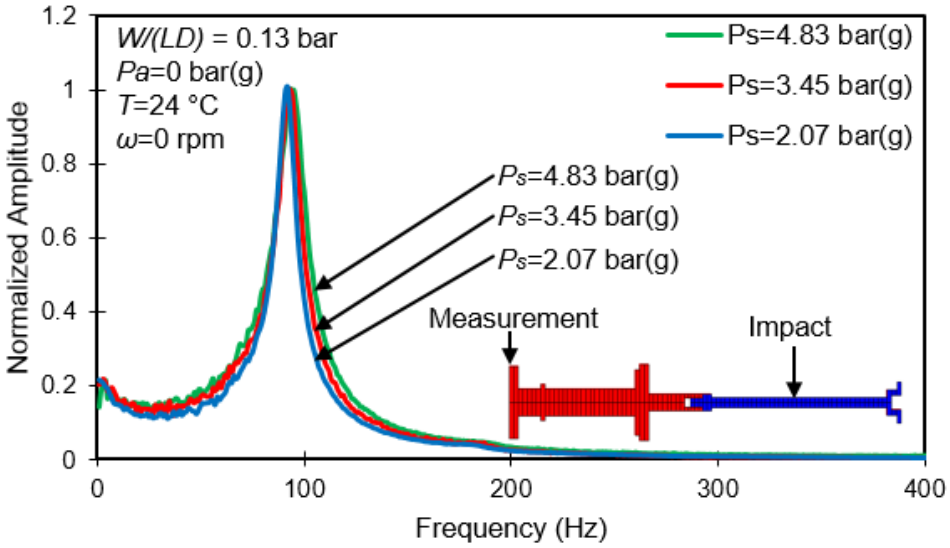

Figure 14. Amplitude of rotor motion, normalized with respect to peak amplitude, vs. frequency for operation without rotor speed, and with room temperature (*T*=24 °C) water at supply pressure (P_S) of 2.07, 3.45, and 4.83 bar(g). Ambient pressure (P_a) is 0 bar(g). Specific static load on each bearing (*W*/(*LD*)) = 0.13 bar. Measurement at 45° away from vertical plane on free end thrust collar. Inset shows impact and measurement locations.

Table 3. Predicted tilting-pad journal bearing coefficients obtained at null rotor speed. Water lubricates bearings. Radial clearance = 89 µm. Static load on each bearing = 18.9 N. Specific static load on each bearing (*W*/(*LD*)) = 0.13 bar. Frequency = 0 Hz. Pure hydrostatic operation. Model in Ref. [11].

Supply Press. P_S [bar(g)]	Static Eccent. e_S [µm]	Flow Rate Q_S [LPM]	Recess Press. P_R [bar(g)]	Horiz. Direct Stiffness K_{XX} [MN/m]	Vert. Direct Stiffness K_{YY} [MN/m]	Horiz. Direct Damping C_{XX} [Ns/m]	Vert. Direct Damping C_{YY} [Ns/m]
1.4	23	5.7	0.86	0.81	0.81	720	760
2.1	18	7.4	1.06	1.10	1.10	800	820
2.8	14	8.8	1.26	1.33	1.33	870	880
3.5	13	10.0	1.44	1.52	1.54	940	950
4.1	11	11.0	1.62	1.69	1.71	1000	1000
4.8	10	12.0	1.81	1.85	1.87	1060	1070
5.5	9	12.9	2.00	2.01	2.02	1120	1120
6.2	9	13.7	2.20	2.16	2.17	1180	1180
6.9	8	14.5	2.38	2.31	2.32	1230	1230

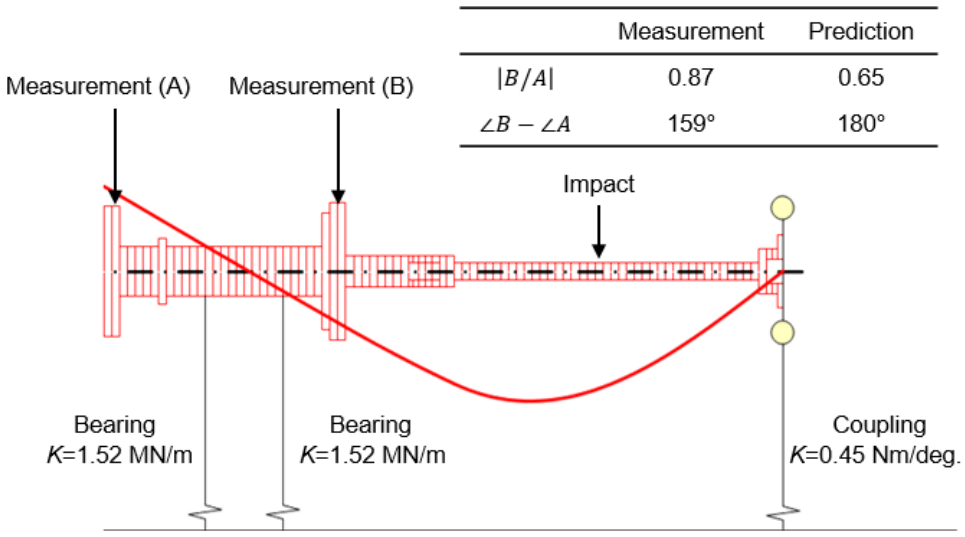

Figure 15. Predicted mode shape of rotor-coupling at its fundamental natural frequency for operation without rotor speed. Water at 3.45 bar(g) and *T*=24 °C supplies the radial bearings. Ambient pressure is 0 bar(g). Specific static load on each bearing (*W*/(*LD*)) = 0.13 bar. The relative amplitude ($|B/A|$) and phase angle ($\angle B - \angle A$) between measured displacements on each thrust collar correspond to the predicted mode shape.

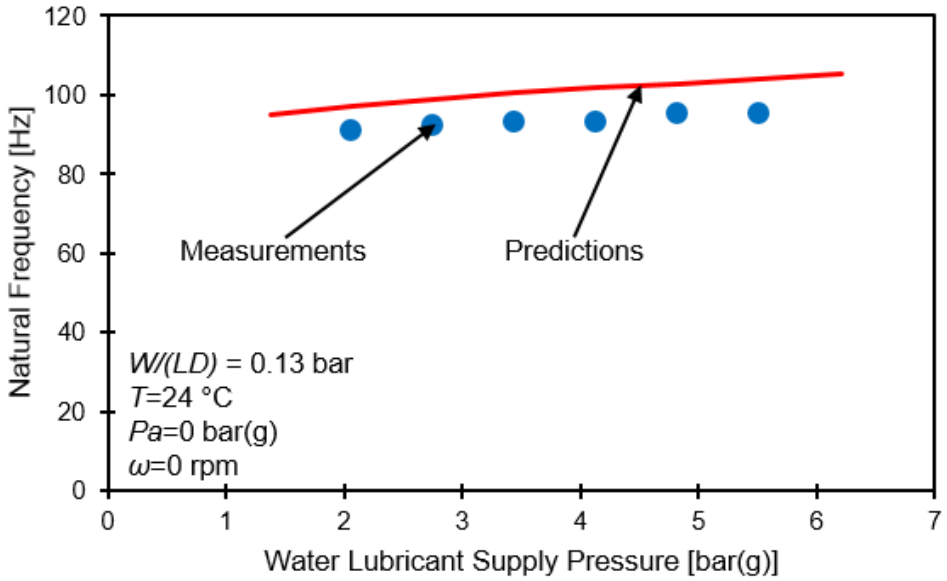

Figure 16. Measured and predicted natural frequency vs. water lubricant supply pressure into journal bearings. Water inlet temperature *T*=24 °C. Operation without rotor speed. Ambient pressure (P_a) is 0 bar(g). Specific static load on each bearing (*W*/(*LD*)) = 0.13 bar. Uncertainty in natural frequency is ±1 Hz.

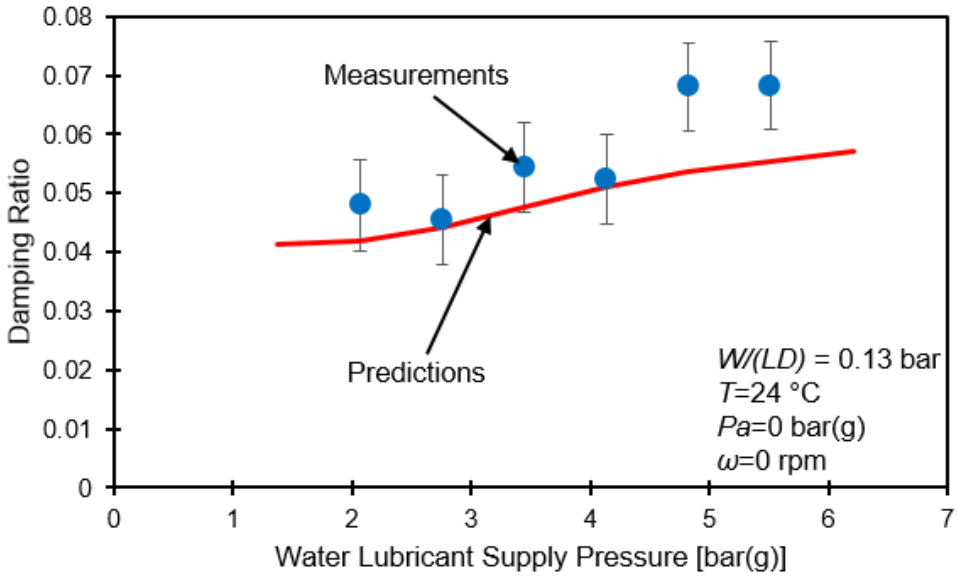

Figure 17. Measured and predicted damping ratio vs. water lubricant supply pressure into journal bearings. Water inlet temperature *T*=24 °C. Operation without rotor speed. Ambient pressure (P_a) is 0 bar(g). Specific static load on each bearing (*W*/(*LD*)) = 0.13 bar. Damping ratio estimated using the half-power method. Error bars show uncertainty in damping ratio.

ASSESSMENT OF LATERAL ROTORDYNAMIC RESPONSE DUE TO IMBALANCE DURING RAMP UP AND COAST DOWN

With the rotor and coupling connected, water (24 °C) at 3.45 bar(g) supplies the radial bearings and lifts the rotor-coupling assembly. Water at a low pressure (0.5 bar(g)) supplies the slave thrust bearing to prevent contact between the slave bearing and the rotor. The test thrust bearing is completely removed from the test rig to avoid any contact. The rotor-coupling system accelerates to 5.25 krpm ($R\omega = 10.5\ \mathrm{m/s}$ at the rotor surface supported by the radial bearings, R = 3.81 cm) in increments of 250 rpm. At each incremental shaft speed, an impact hammer strikes the rotor-coupling assembly where the rotor and coupling connect to each other.

Eddy current sensors measure the lateral displacement at each of the rotor thrust collars. A signal analyzer shows the frequency content of the displacement of each rotor thrust collar. While the rotor operates at a speed below 5.25 krpm (88 Hz), the impact hammer is unable to exert a high enough load to readily see the first natural frequency (93 Hz) on the signal analyzer because the bearings offer significant damping that quickly dissipates vibration at the first natural frequency.

While the bearings operate at the same conditions as listed above, the rotor accelerates to 5 krpm (83 Hz) and decelerates back to rest at a ramp rate 30 rpm/s, which is the slowest ramp rate allowed by the motor variable frequency drive. Four radially mounted eddy current sensors measure the X and Y positions of each rotor thrust collar. The ADRE® system records the measurements and performs several data analyses.

Figure 18 shows a cascade plot depicting the rotor response at the drive end thrust collar as the rotor accelerates to 5 krpm for operation with water supplying the radial bearings at 3.45 bar(g). Figure 19 shows a cascade plot of the rotor response at the free end thrust collar as the rotor accelerates to 5 krpm for operation with 3.45 bar(g) water supplying the radial bearings. Figure 20 shows a bode plot of the rotor response at the free end thrust collar as the rotor accelerates to 5 krpm with water at 3.45, 4.48, and 5.52 bar(g) water supplying the radial bearings.

The measurements show that for operation up to 5 krpm and various water supply pressure, the displacement is synchronous. As the rotor speed increases, the synchronous amplitude of rotor motion also begins to increase, but the system does not reach its first critical speed (93 Hz). As the water supply pressure into the radial bearings increases, the amplitude of rotor motion slightly decreases, evidencing an increased water lubricant supply pressure aids in constraining the rotor motion. The amplitude of rotor motion is larger on the free end thrust collar than it is on the drive end thrust collar. This is due to a conical mode shape at the fundamental natural frequency with a node that is located closer to the drive end thrust collar than the free end thrust collar. Please note, there are large run outs on each thrust collar, especially the free end thrust collar.

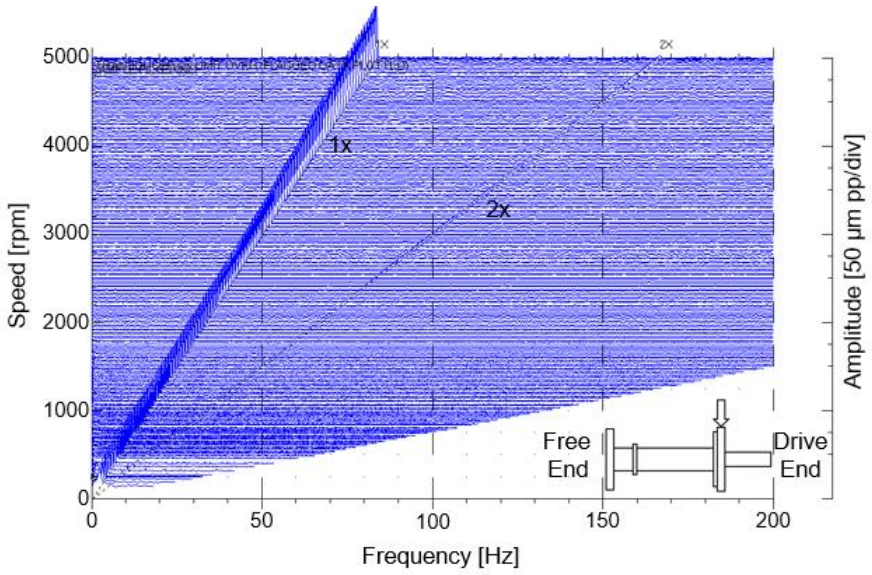

Figure 18. Cascade plot of lateral rotor displacement during ramp up to 5 krpm with 3.45 bar(g) water supplying the radial bearings. Water inlet temperature *T*=24 °C. Ambient pressure (P_a) is 0 bar(g). Operation without active thrust bearings. Inset shows measurement location is on drive end thrust collar.

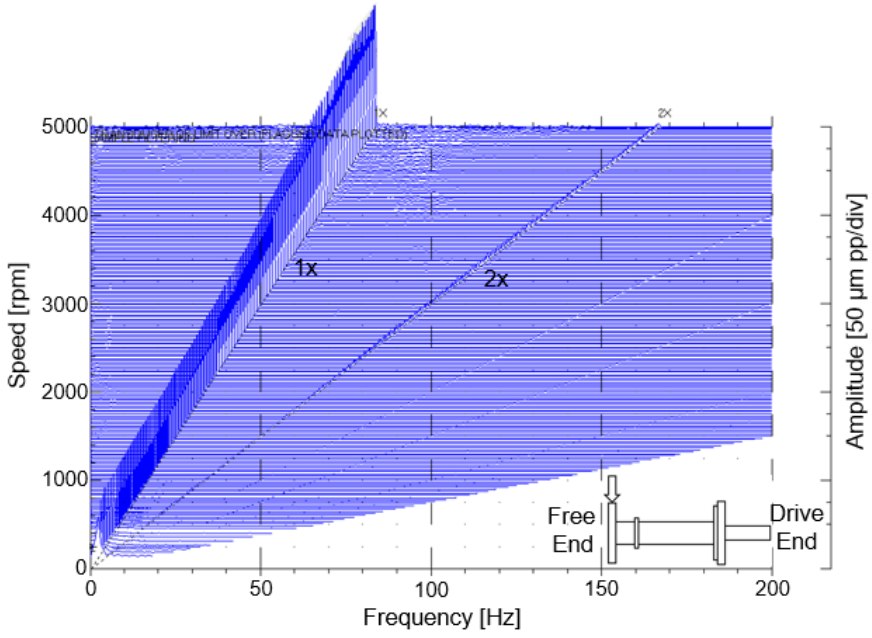

Figure 19. Cascade plot of lateral rotor displacement during ramp up to 5 krpm with 3.45 bar(g) water supplying the bearings. Water inlet temperature *T*=24 °C. Ambient pressure (P_a) is 0 bar(g). Operation without active thrust bearings. Inset shows measurement location is on free end thrust collar.

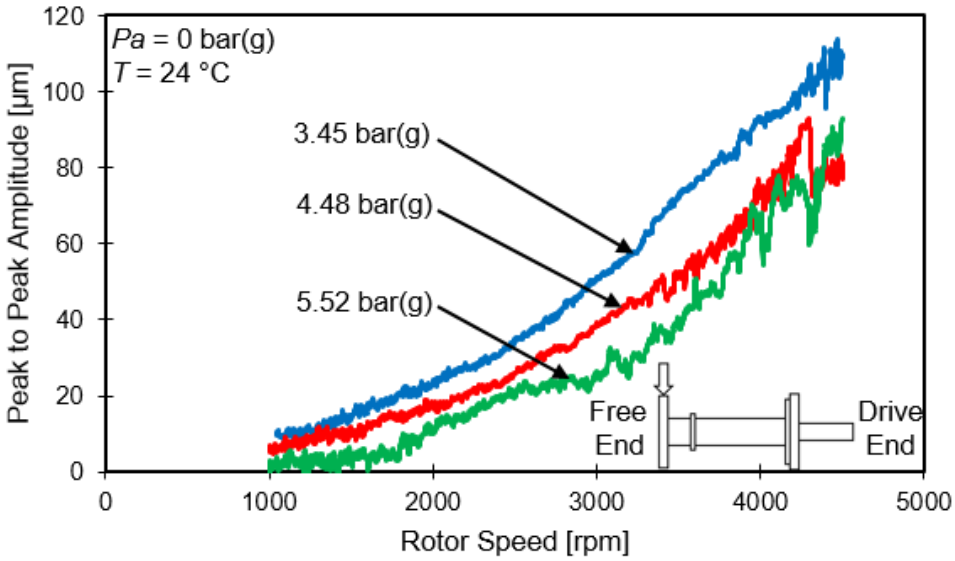

Figure 20. Bode plot of peak to peak amplitude of rotor motion vs. rotor speed for operation with water (24 °C) at 3.45, 4.48, and 5.52 bar(g) supplying the radial bearings. Ambient pressure (P_a) is 0 bar(g). Operation without active thrust bearings. Measurement taken on thrust collar on free end. Slow roll compensation at 1,000 rpm. Radial clearance of bearings is 91 µm.

THRUST BEARING PERFORMANCE FOR TESTS WITHOUT ROTOR SPEED

For reader convenience, Table 4 and Figure 21 present the geometric characteristics and a depiction of the hydrostatic thrust bearings, respectively. Recall, Ref. [4] fully details the rig components as well as other ancillary components. Note that Ref. [2] and Ref. [10] show the thrust bearings have equal diameter orifices; however, recent measurements show that the slave thrust bearing has larger diameter orifices than the test thrust bearing (1.80 mm > 1.55 mm). Measurements consisted of inserting increasing diameter drill bits into the orifices to determine the orifice diameter.

Without shaft rotation, pressurized water at T=24 °C feeds the journal bearings at 3.45 bar(g). Water at an increasing pressure supplies both the test and slave thrust bearings (max. 4.14 bar(g)). The load shaft pushes the test thrust bearing towards the rotor causing the thrust bearing to push a load onto the rotor thrust collar. The slave thrust bearing, rigidly affixed to the housing, reacts to the applied load.

Eddy current sensors face a thrust collar and measure the distance between each thrust collar and thrust bearing at three circumferential locations. The three gap measurements provide information to estimate the clearance between the thrust collar and the bearing surface at the center of the thrust bearing, as well as to estimate the tilt (misalignment) of the thrust collar relative to the corresponding thrust bearing. Equation (3) shows the clearance ($C(x,y)$) between the thrust bearing surface and the thrust collar can be estimated at any point on the thrust bearing surface by using the clearance between the thrust collar and the thrust bearing at the center of the thrust bearing (C_0), the tilt of the thrust collar relative to the thrust bearing about the y-axis (δ_y) and the x-axis (δ_x), and a rigid body

assumption where x and y are defined in Figure 21. Figure 22 depicts the clearance between the thrust collar and the thrust bearing at the center of the thrust bearing (C_0) and the tilt of the thrust collar about the x-axis (δ_x) and y-axis (δ_y) relative to the thrust bearing. Note that Appendix E presents more details on this analysis.

$$C(x, y) = C_0 + \delta_y x + \delta_x y \tag{3}$$

A pressure transducer measures the pressure (P_R) in a recess or pocket. As pressure regulators maintain a constant lubricant supply pressure into the thrust bearings, the static loader applies a decreasing load. The above procedure is repeated for water (24 °C) feeding the thrust bearings at a supply pressure (P_S) of 2.76, 3.45, and 4.14 bar(g).

Table 4. Dimensions and physical parameters of hydrostatic thrust bearings [12]. Material: 660 Bearing Bronze.

		Slave Thrust Bearing	Test Thrust Bearing
Thrust Face	Inner Diameter, D_{in}	40.64 mm	
	Outer Diameter, D_{out}	76.2 mm	
	Thrust Bearing Area, A	32.6 cm^2	
	Flange Outer Diameter	98.43 mm	
Pocket	Number of Pockets	8	
	Arc Length	20°	
	Radial Length	8.13 mm	
	Depth	0.44 mm	0.51 mm
	Pocket/Wetted Area Ratio	0.19	
Orifice	Number of Orifices per Pocket	1	
	Diameter, D_{orif}	1.80 mm	1.55 mm

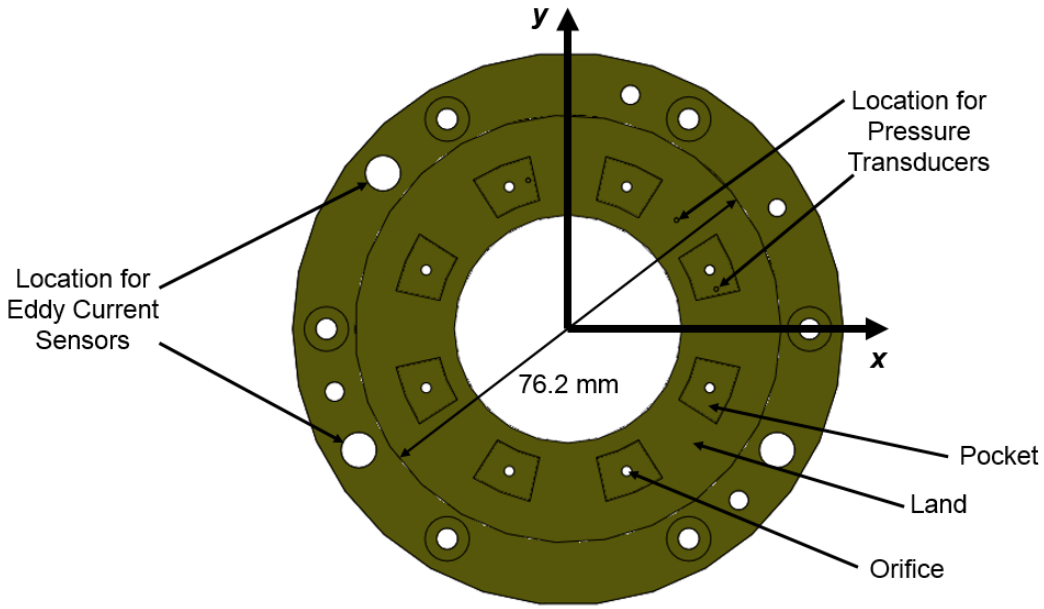

Figure 21. Depiction of water lubricated test thrust bearing. Orifice diameter = 1.55 mm. Reprinted from [12].

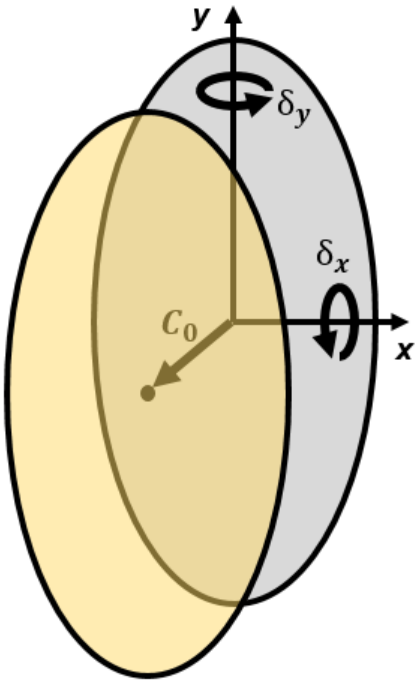

Figure 22. Depiction of axial clearance between thrust collar and thrust bearing at the center of the thrust bearing (C_0) and thrust collar tilt about the x-axis (δ_x) and y-axis (δ_y) relative to the thrust bearing.

For operation without rotor speed and water supplying the thrust bearings at 2.76, 3.45, and 4.14 bar(g), i.e. pure hydrostatic condition, Figures 23 and 24 show the misalignment of the test and slave thrust bearings about both axes relative to their corresponding thrust collars, respectively. The faces of both thrust bearings are parallel with the rotor thrust collars so that the maximum deviation in clearance across each thrust bearing is less than ±13 μm. However, the figures show that there is a large uncertainty in the misalignment and clearance of each measurement produced from the allowable run out on each rotor thrust collar (±5 μm). Appendix E shows more details pertaining to the uncertainty analysis.

Figure 25 shows the estimated axial clearance at the center of the test and slave thrust bearings versus applied axial load per unit area (*W/A*). Note A=32.6 cm^2 = $\frac{1}{4}\pi(D_{Out}^2 - D_{in}^2)$. Figure 26 shows the pocket pressure ratio (P_R/P_S) versus axial clearance and specific axial load (*W/A*). In both figures, water (24 °C) feeds the thrust bearings at a supply pressure (P_S) 2.76, 3.45, and 4.14 bar(g), and the rotor does not spin. The exhaust pressure is ambient (P_a) = 0 bar(g). For operation without rotor speed, there are no measurements of flow rate to correspond with clearance and recess pressure measurements.

For a constant load, the axial clearance of each thrust bearing increases and the recess pressure ratio decreases as the water lubricant pressure supply increases. The specific load (*W/A*) is less than half of the water lubricant supply pressure because the load cannot exceed $P_R * A$ in a hydrostatic bearing. Also, at a constant specific axial load and water lubricant supply pressure, the slave TB operates with a larger axial clearance than the test TB, since the slave TB has larger orifice diameters than the test TB.

At each lubricant supply pressure, the axial clearance of each thrust bearing decreases as the specific load increases. As the clearance decreases, the flow rate into the thrust bearings also decreases due to the increase in flow resistance across the film lands of the thrust bearing. As the flow rate decreases, the water lubricant has a lower pressure drop across the orifices of the thrust bearing, resulting in a higher pocket pressure. Thus, the pocket pressure ratio increases as the axial clearance decreases.

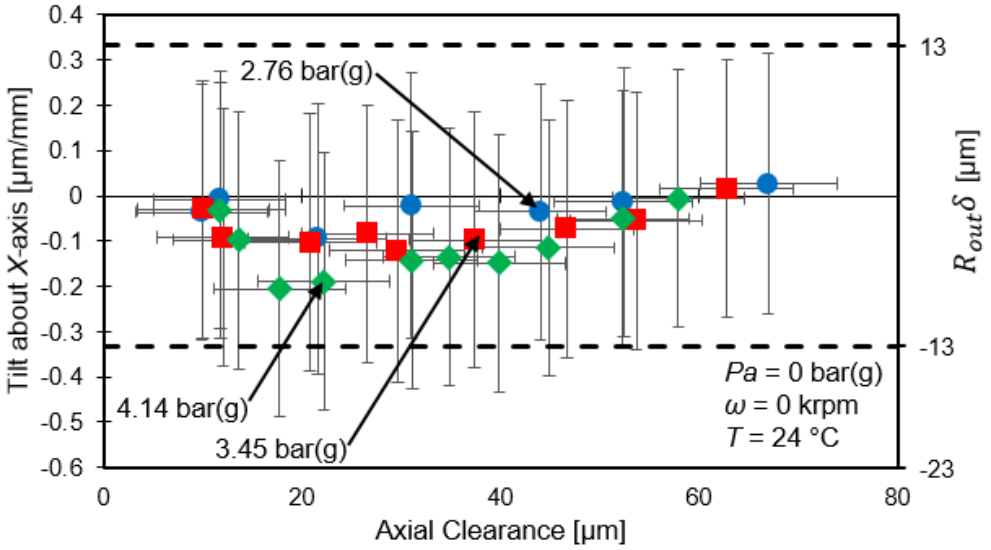

(a)

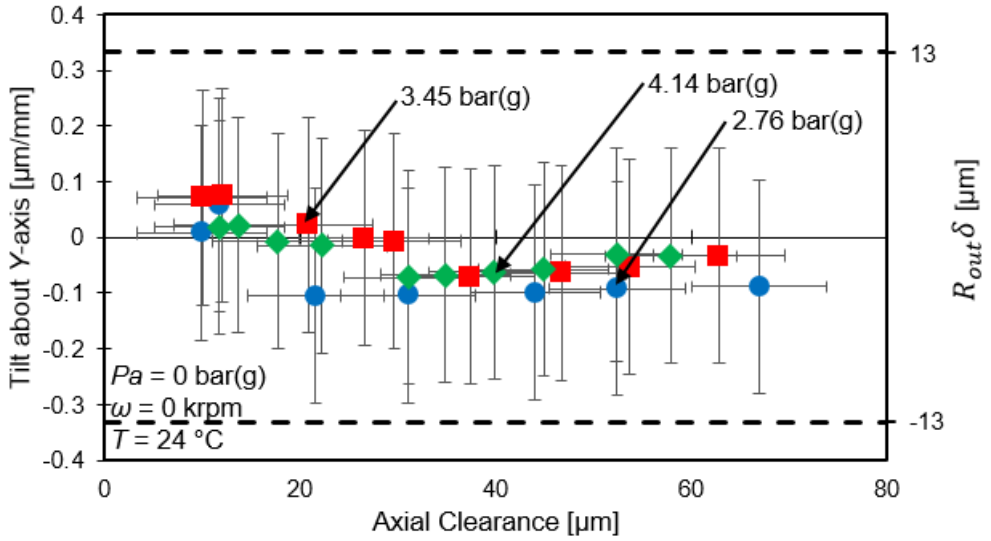

(b)

Figure 23. Estimated misalignment (µm/mm) between test thrust bearing and thrust collar about (a) *X*-axis and (b) *Y*-axis vs. estimated axial clearance at the center of the test thrust bearing for operation with water (24 °C) at a supply pressure (P_S) of 2.76, 3.45, and 4.14 bar(g) into the thrust bearing. No shaft rotation. Specific axial load (*W*/*A*) ranges from 0.39 bar to 1.76 bar. Water at 3.45 bar(g) feeds the journal bearings. Ambient pressure (P_a) is 0 bar(g). Vertical and horizontal error bars represent the uncertainty in the misalignment between the test thrust bearing and thrust collar and the uncertainty in the clearance at the center of the test thrust bearing at a 95% confidence level, respectively. Dashed lines indicate the misalignment slope that corresponds with ±13 µm deviation in axial clearance over the surface of the test thrust bearing.

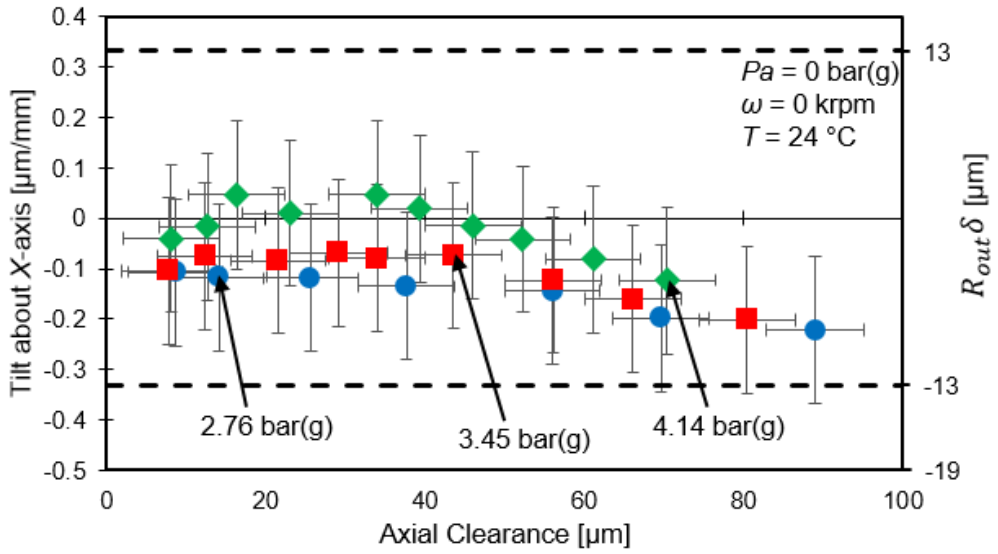

(a)

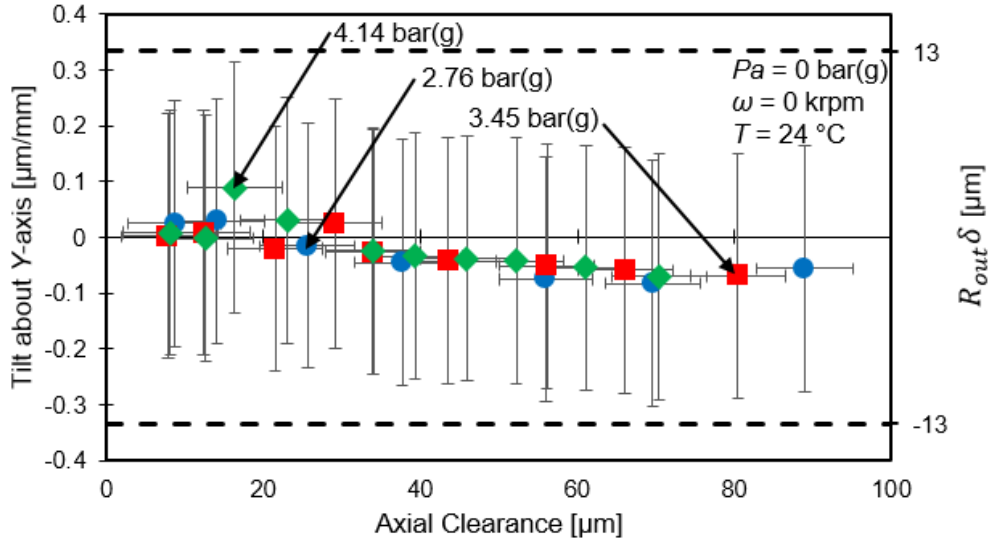

(b)

Figure 24. Estimated misalignment (µm/mm) between slave thrust bearing and thrust collar about (a) *X*-axis and (b) *Y*-axis vs. estimated axial clearance at the center of the slave thrust bearing for operation with water (24 °C) at a supply pressure (P_S) of 2.76, 3.45, and 4.14 bar(g) into the thrust bearing. No shaft rotation. Specific axial load (*W*/*A*) ranges from 0.39 bar to 1.76 bar. Water at 3.45 bar(g) feeds the journal bearings. Ambient pressure (P_a) is 0 bar(g). Vertical and horizontal error bars represent the uncertainty in the misalignment between the slave thrust bearing and thrust collar and the uncertainty in the clearance at the center of the slave thrust bearing at a 95% confidence level, respectively. Dashed lines indicate the misalignment slope that corresponds with ±13 µm deviation in axial clearance over the surface of the slave thrust bearing.

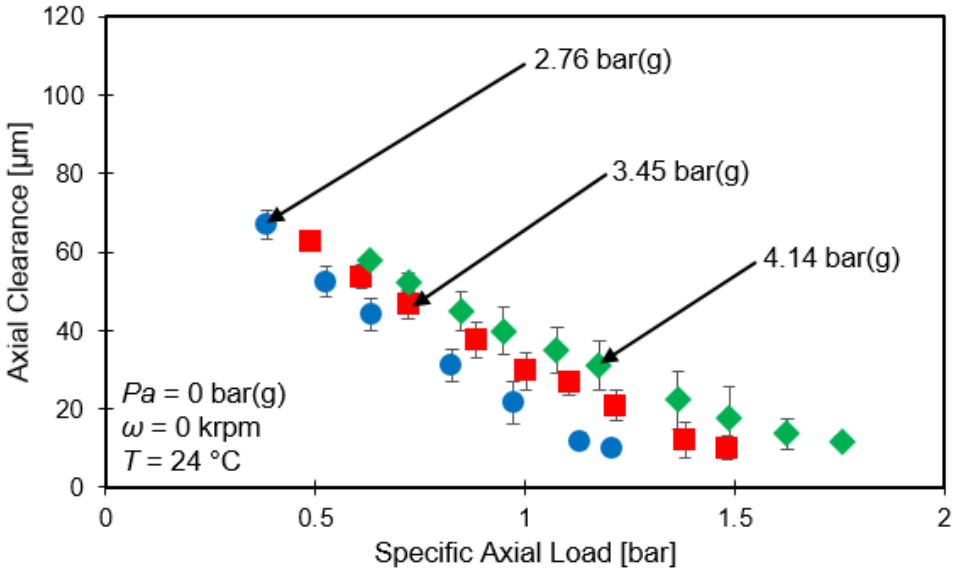

(a) Test Thrust Bearing

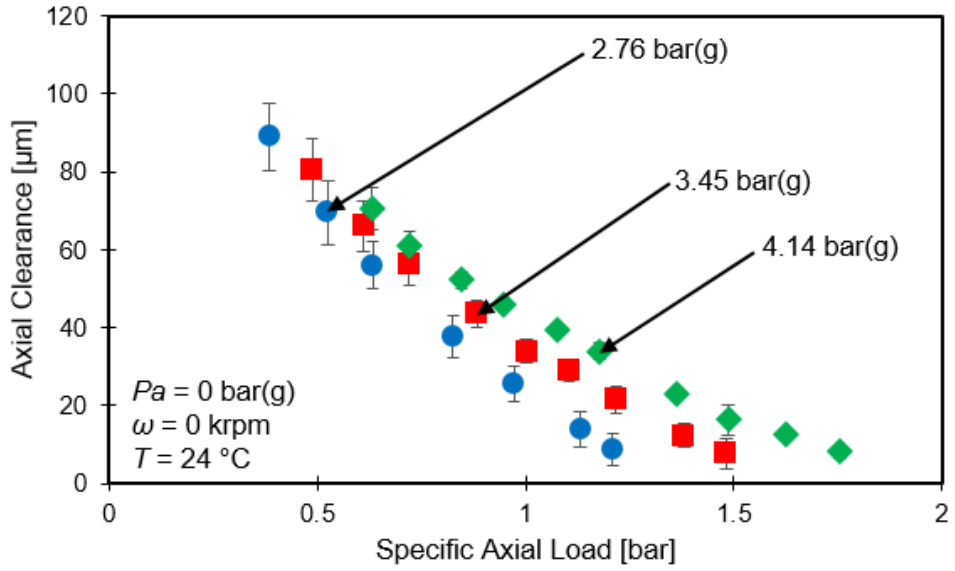

(b) Slave Thrust Bearing

Figure 25. Estimated axial clearance at the center of (a) test thrust bearing and (b) slave thrust bearing vs. specific load (*W/A*) for operation with water (24 °C) at a supply pressure (P_S) of 2.76, 3.45, and 4.14 bar(g) into the thrust bearing. No shaft rotation. Water at 3.45 bar(g) feeds the journal bearings. Ambient pressure (P_a) is 0 bar(g). Horizontal error bars represent the uncertainty in the axial load at a 95% confidence level. Vertical error bars indicate the maximum and minimum clearances on the face of the thrust bearing.

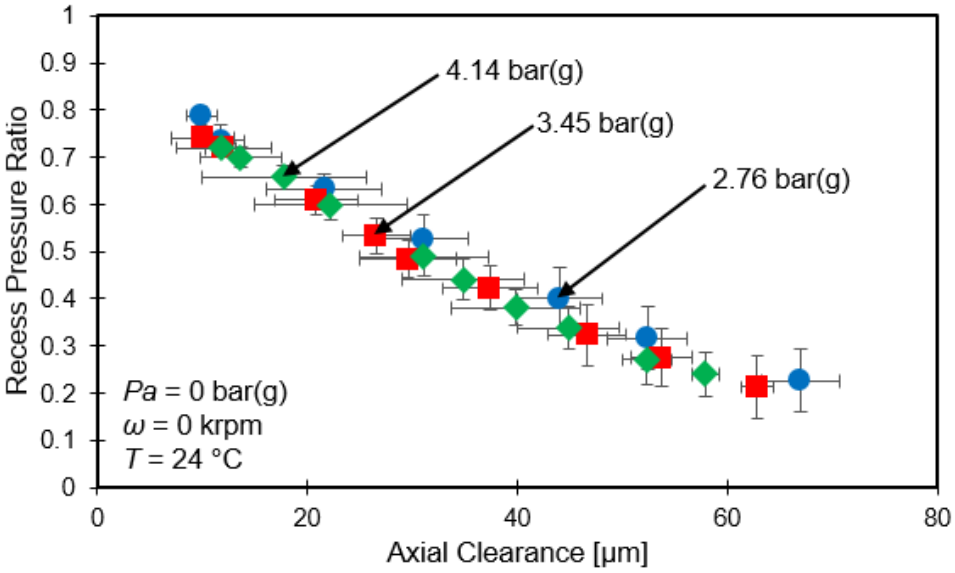

(a)

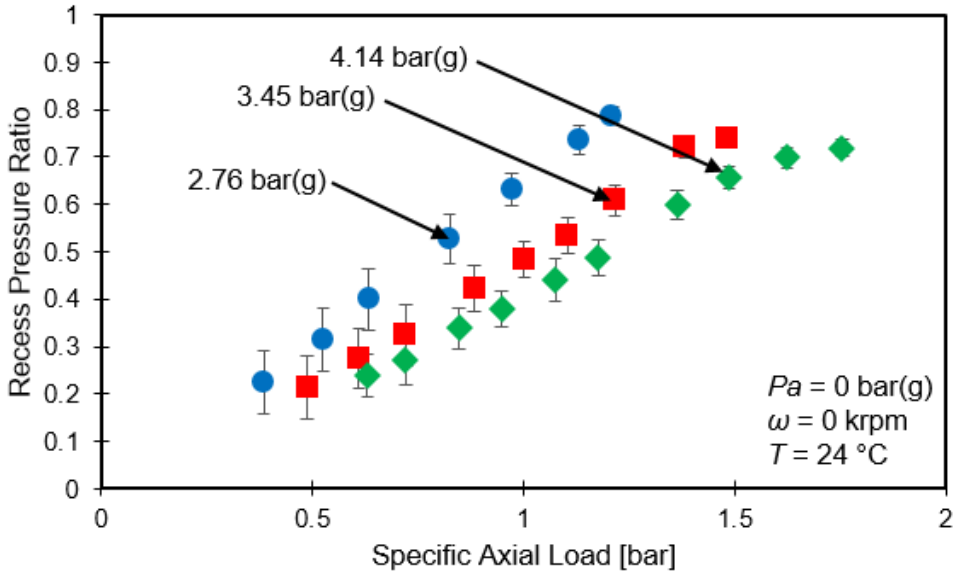

(b)

Figure 26. Derived recess pressure ratio (P_R/P_S) at test thrust bearing vs. (a) axial clearance at the center of the thrust bearing and (b) specific axial load, respectively, for operation with water (24 °C) at a supply pressure (P_S) of 2.76, 3.45, and 4.14 bar(g) into the thrust bearing. No shaft rotation. Water at 3.45 bar(g) feeds the journal bearings. Ambient pressure (P_a) is 0 bar(g). Vertical error bars represent the uncertainty in the recess pressure ratio at a 95% confidence level. Horizontal error bars indicate the maximum and minimum clearances on the face of the thrust bearing and the uncertainty in the axial load at a 95% confidence level, respectively.

THRUST BEARING PERFORMANCE FOR TESTS WITH A LOW ROTOR SPEED

Prior to initiating shaft rotation, pressurized water (T=31 °C) supplies the journal bearings at 3.45 bar(g) and lifts the rotor. Note that the water temperature is higher than in previous measurements (T=24 °C previously) without shaft rotation because the external temperature (pipes are located outdoors) is higher. Water at 2.76 bar(g) supplies the slave and test thrust bearings. The static loader applies a load onto the test thrust bearing, which transfers that load to the rotor thrust collar. The slave thrust bearing, rigidly affixed to the housing, reacts to the applied load. The static loader applies the maximum desired load (356 N) onto the thrust bearings without contact between the rotor and the thrust bearings.

Considering that the rotor spins freely (by hand), the motor accelerates the rotor/coupling assembly to 3 krpm (50 Hz), which corresponds to a surface speed of 16 m/s on the edge of the thrust collars (R_{out} = 5.08 cm). With a constant lubricant supply pressure into the thrust bearings, the static loader decreases the applied axial load. Note that the test procedure involves only decreasing the applied load, so the clearance of the thrust bearing only increases while the rotor is spinning at 3 krpm, thus avoiding potential contact between the rotor thrust collar and thrust bearing surfaces with rotor rotation. The above procedure is repeated for water (31 °C) feeding the thrust bearings at a supply pressure (P_S) of 2.76, 3.45, and 4.14 bar(g) with an axial load ranging from 90 to 450 N; the specific axial load (W/A) ranges from 0.3 to 1.4 bar.

Figures 27-30 show the clearance at the center of the test and slave thrust bearings, the axial load applied onto the thrust bearings, and the thrust collar tilt about each axis of the test and slave thrust bearings versus time and frequency, respectively. The test rig operates with 3.45 bar(g) water (31 °C) supplying the thrust bearing and an average specific load of 0.80 bar applied on the thrust bearing. The rotor spins at 3 krpm. The axial load remains relatively constant with respect to time and frequency. The axial clearance at the center of each thrust bearing is largely constant with a small amplitude at 50 Hz (3 krpm). However, the thrust collar tilt about each axis relative to each thrust bearing varies periodically at a frequency of 50 Hz (3 krpm). Thus, as the rotor spins, the orientation of the thrust collars change relative to the thrust bearings. The amplitude of the tilt is the same for both the test and slave thrust bearings, showing that the rotor moves as a rigid piece.

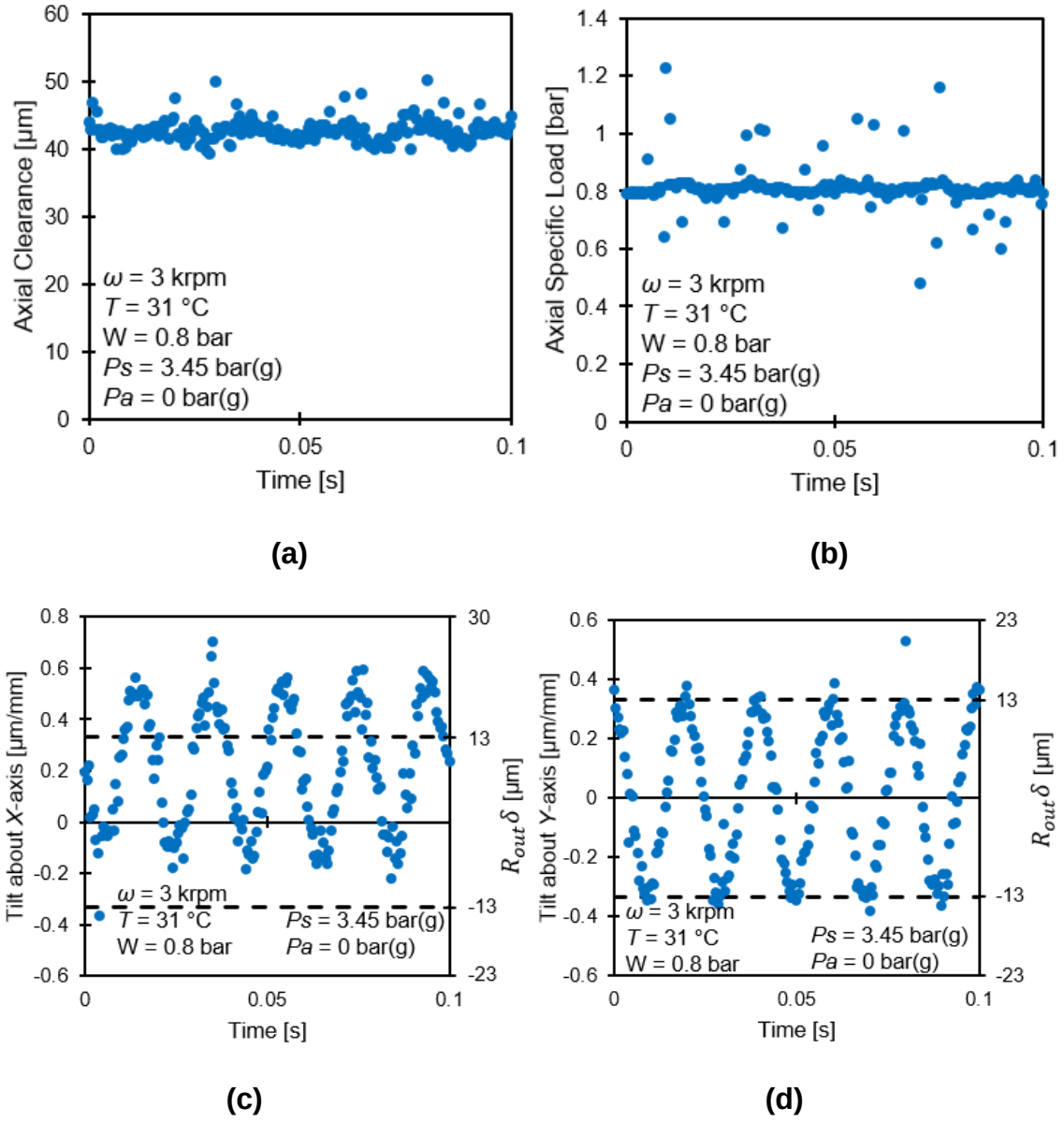

Figure 27. Estimated (a) axial clearance between test thrust bearing and thrust collar, tilt of thrust collar about (c) *X*-axis and (d) *Y*-axis relative to test thrust bearing, and (b) measured specific axial load vs. time for operation with water (31 °C) at a supply pressure (P_s) of 3.45 bar(g) into the thrust bearing. Shaft rotates at 3 krpm. Specific axial load (*W/A*) is 0.80 bar. Water at 3.45 bar(g) feeds the journal bearings. Ambient pressure (P_a) is 0 bar(g).

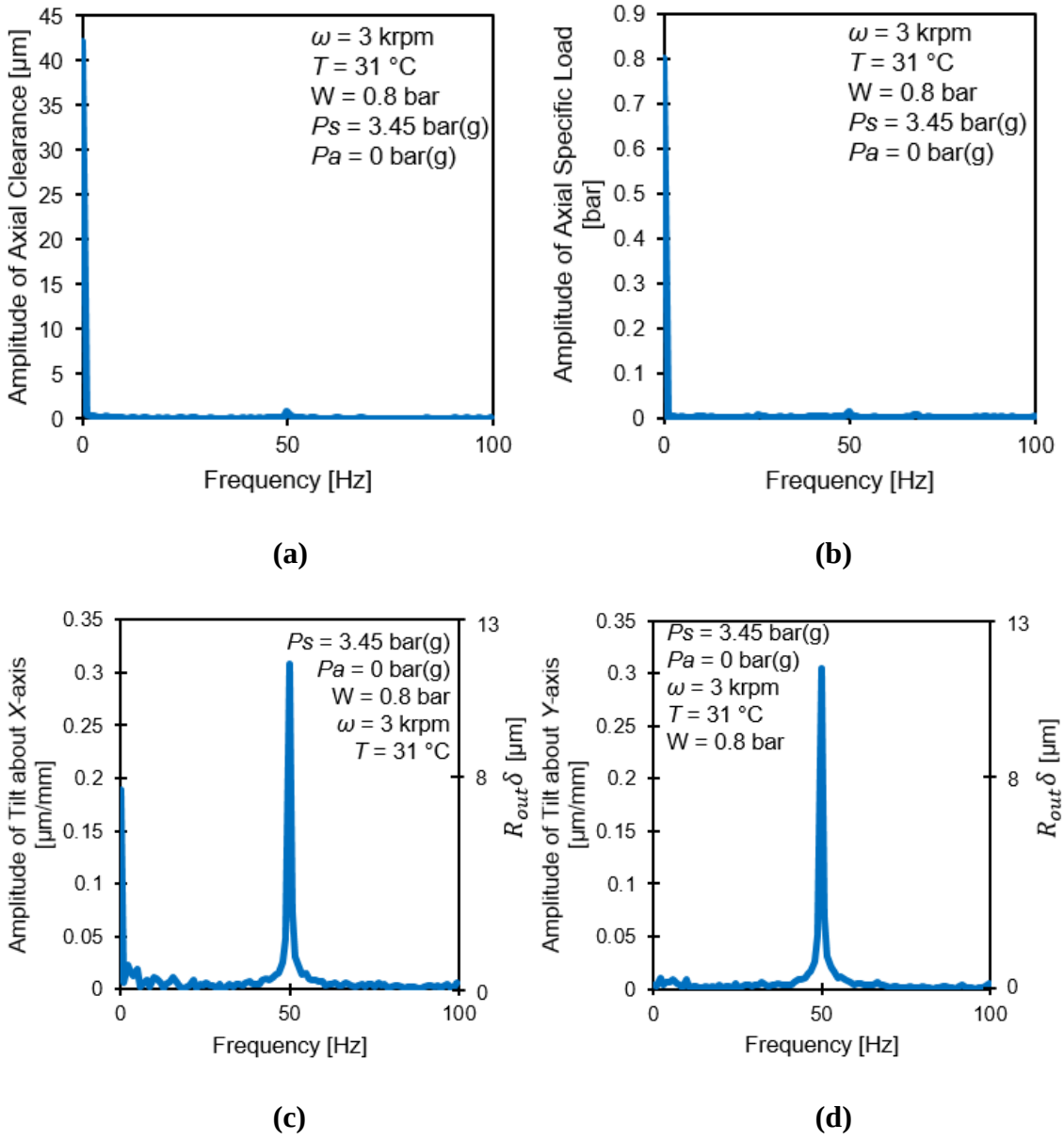

Figure 28. Amplitude of estimated (a) axial clearance between test thrust bearing and thrust collar, tilt of thrust collar about (c) *X*-axis and (d) *Y*-axis relative to test thrust bearing, and (b) measured specific axial load vs. frequency for operation with water (31 °C) at a supply pressure (P_S) of 3.45 bar(g) into the thrust bearing. Shaft rotates at 3 krpm. Specific axial load (*W/A*) is 0.80 bar. Water at 3.45 bar(g) feeds the journal bearings. Ambient pressure (P_a) is 0 bar(g).

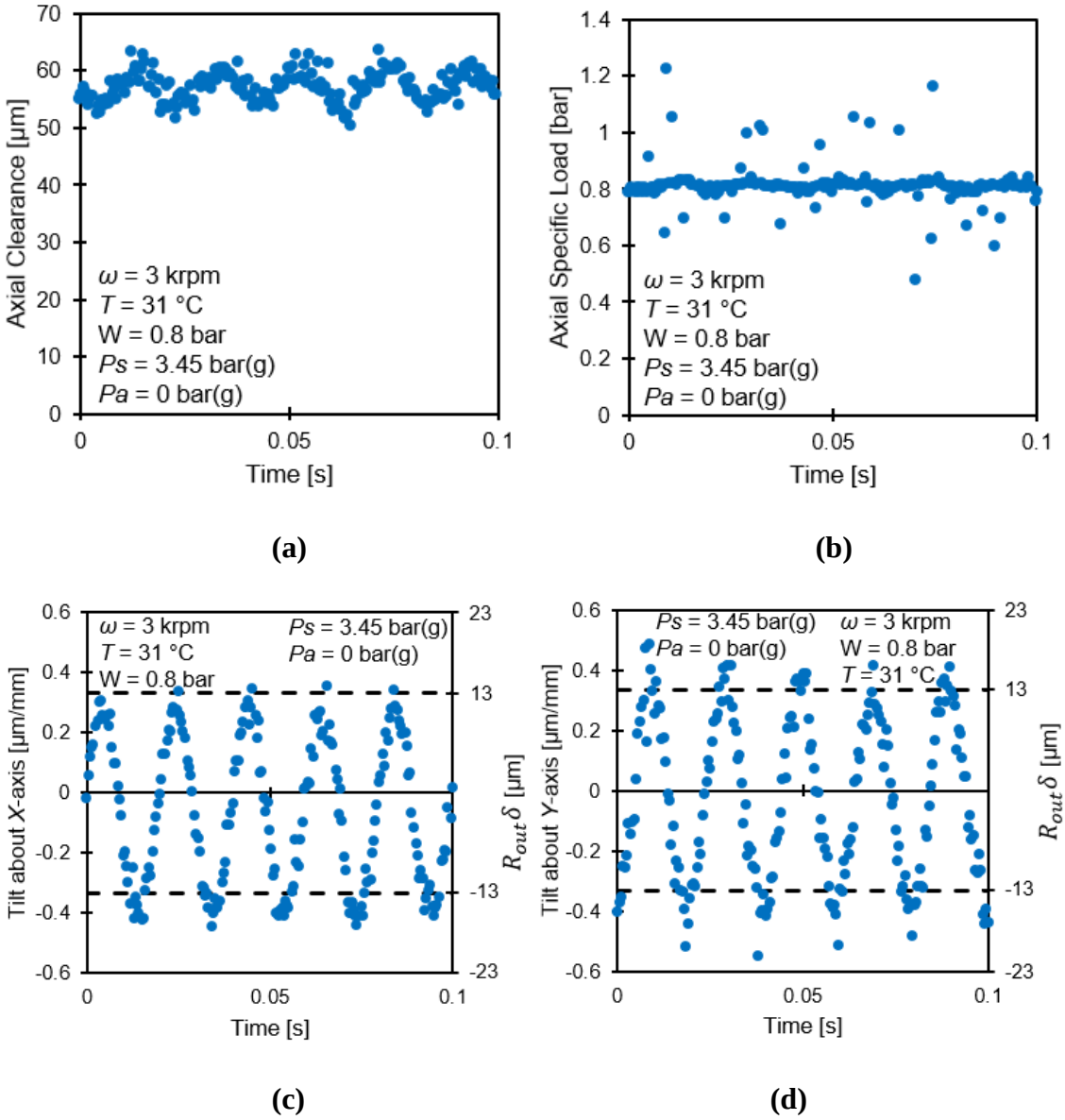

Figure 29. Estimated (a) axial clearance between slave thrust bearing and thrust collar, tilt of thrust collar about (c) *X*-axis and (d) *Y*-axis relative to slave thrust bearing, and (b) measured specific axial load vs. time for operation with water (31 °C) at a supply pressure (P_S) of 3.45 bar(g) into the thrust bearing. Shaft rotates at 3 krpm. Specific axial load (*W/A*) is 0.80 bar. Water at 3.45 bar(g) feeds the journal bearings. Ambient pressure (P_a) is 0 bar(g).

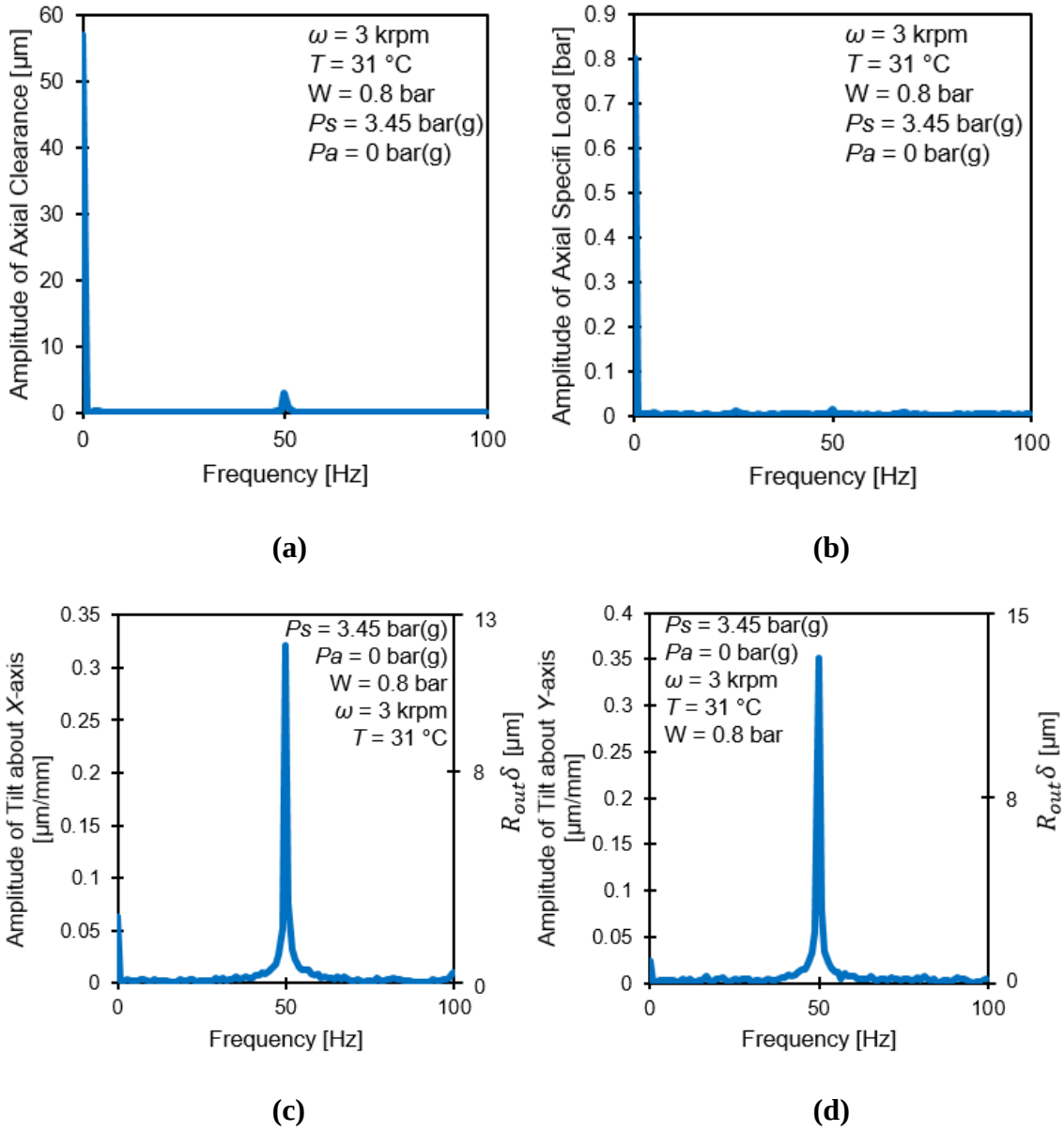

Figure 30. Amplitude of estimated (a) axial clearance between slave thrust bearing and thrust collar, tilt of thrust collar about (c) *X*-axis and (d) *Y*-axis relative to slave thrust bearing, and (b) measured specific axial load vs. frequency for operation with water (31 °C) at a supply pressure (P_S) of 3.45 bar(g) into the thrust bearing. Shaft rotates at 3 krpm. Specific axial load (*W/A*) is 0.80 bar. Water at 3.45 bar(g) feeds the journal bearings. Ambient pressure (P_a) is 0 bar(g).

For operation with water at 2.76, 3.45, and 4.14 bar(g) supplying the thrust bearings and with a rotor spinning at 3 krpm (50 Hz), Figures 31 and 32 show the misalignment of

the test and slave thrust bearings relative to their corresponding thrust collars, respectively. The faces of both thrust bearings are parallel with the rotor thrust collars so that the mean of the maximum deviation in clearance across each thrust bearing surface is less than ±13 μm for the vast majority of imposed loads.

However, Figures 31 and 32 show that there is a large difference between the maximum and minimum misalignment angles of each thrust bearing. The large difference indicates that the while the average orientation of each thrust collar is aligned with its corresponding thrust bearing, there are instances where the thrust collar may have a significantly different alignment than the average orientation. The large difference between the maximum and minimum misalignment angles arises from a synchronous rotor motion that causes the orientation of the thrust collar relative to the thrust bearing to change as the rotor spins. Stiffer radial and thrust bearings (higher supply pressure and lower clearance) would mitigate variations in the thrust collar orientation. Note that as axial clearance decreases, the difference between the maximum and minimum clearance on the face of the thrust bearing also decreases; showing that a smaller axial clearance provides more resistance to variations in the thrust collar orientation.

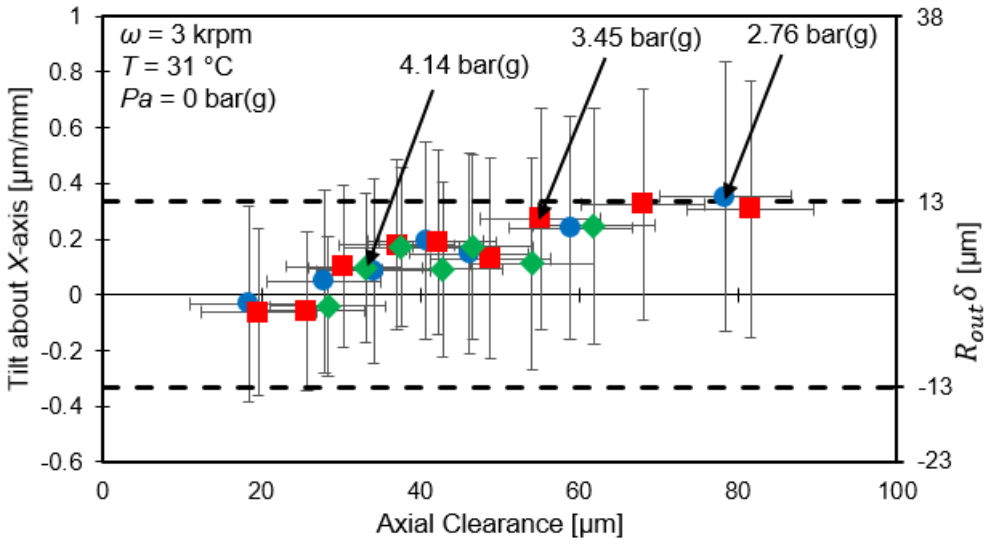

(a)

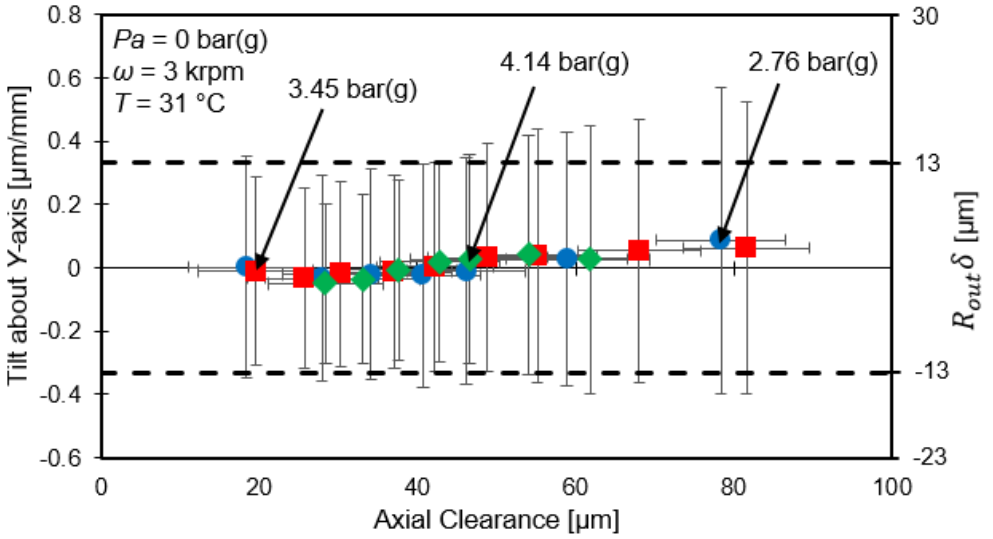

(b)

Figure 31. Estimated misalignment (µm/mm) between test thrust bearing and thrust collar about (a) *X*-axis and (b) *Y*-axis vs. estimated axial clearance at the center of the test thrust bearing for operation with water (31 °C) at a supply pressure (P_S) of 2.76, 3.45, and 4.14 bar(g) into the thrust bearing. Shaft rotates at 3 krpm. Specific axial load (*W*/*A*) ranges from 0.26 bar to 1.41 bar. Water at 3.45 bar(g) feeds the journal bearings. Ambient pressure (P_a) is 0 bar(g). Horizontal error bars represent the uncertainty in the clearance at the center of the test thrust bearing at a 95% confidence level. Vertical error bars indicate the maximum and minimum thrust collar tilt about each axis relative to the face of the thrust bearing. Dashed lines indicate the misalignment slope that corresponds with ±13 µm deviation in axial clearance over the surface of the test thrust bearing.

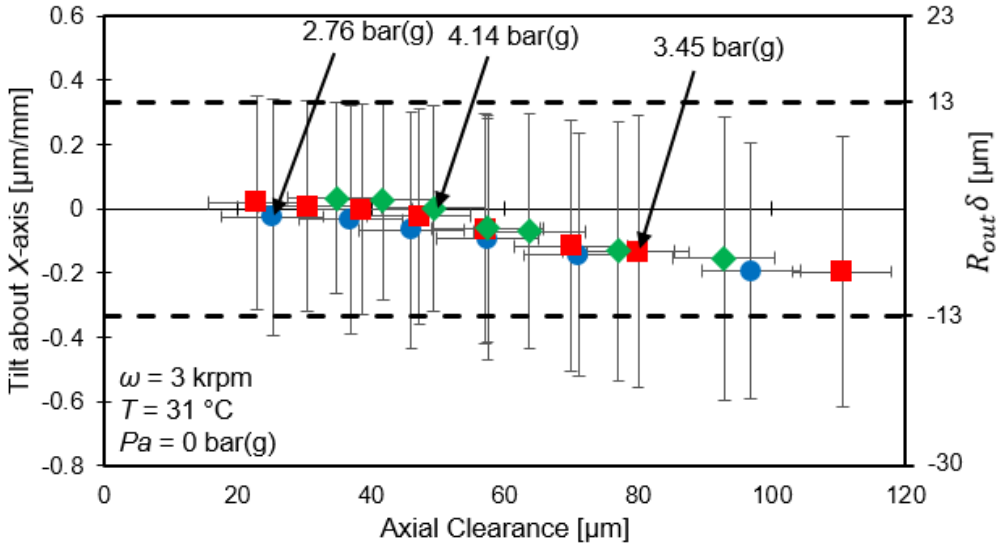

(a)

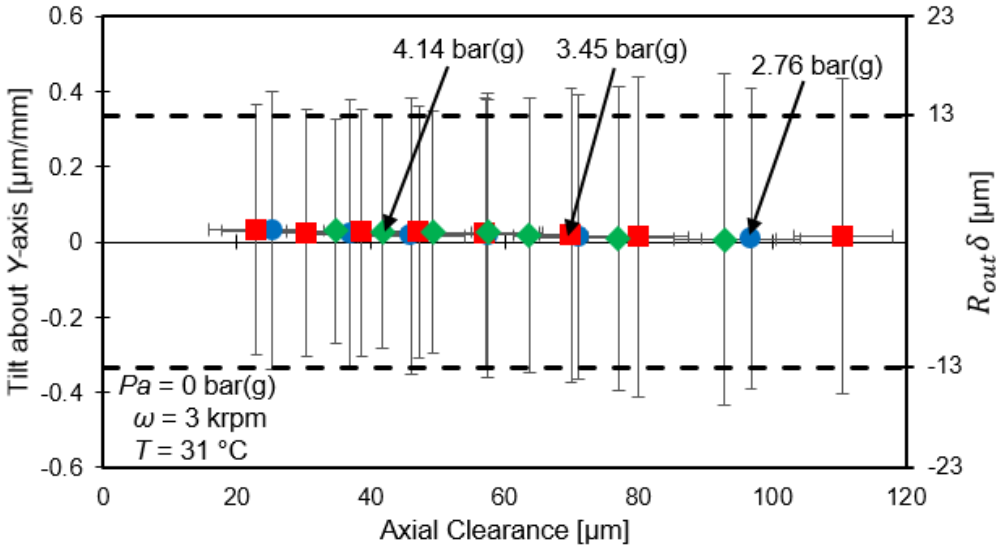

(b)

Figure 32. Estimated misalignment (µm/mm) between slave thrust bearing and thrust collar about (a) *X*-axis and (b) *Y*-axis vs. estimated axial clearance at the center of the slave thrust bearing for operation with water (31 °C) at a supply pressure (P_S) of 2.76, 3.45, and 4.14 bar(g) into the thrust bearing. Shaft rotates at 3 krpm. Specific axial load (*W*/*A*) ranges from 0.26 bar to 1.41 bar. Water at 3.45 bar(g) feeds the journal bearings. Ambient pressure (P_a) is 0 bar(g). Horizontal error bars represent the uncertainty in the clearance at the center of the slave thrust bearing at a 95% confidence level. Vertical error bars indicate the maximum and minimum thrust collar tilt about each axis relative to the face of the thrust bearing. Dashed lines indicate the misalignment slope that corresponds with ±13 µm deviation in axial clearance over the surface of the slave thrust bearing.

Figure 33 shows the axial clearance at the center of the test and slave thrust bearings, respectively, versus specific load (*W/A*) for operation with rotor speed at 3 krpm and a supply pressure of 2.76, 3.45, and 4.14 bar(g) into the thrust bearings. Note A=32.6 cm^2 = $\frac{1}{4}\pi(D_{out}^2 - D_{in}^2)$. At a constant load, the axial clearance of each thrust bearing increases as the water pressure supplied to the thrust bearings increases. However, the specific load (*W/A*) is only a fraction of the water pressure supplied to the thrust bearings. At each water supply pressure, the axial clearance of each thrust bearing decreases as the specific axial load increases. The slave thrust bearing operates with a much larger axial clearance than the test thrust bearing for operation at the same load and water supply pressure. The slave thrust bearing also operates at a larger clearance than the test thrust bearing when the rotor is not spinning (see Figure 25). This is because the slave thrust bearing has orifices with a diameter 16% larger than the orifices in the test thrust bearing (see Table 4). Measurements show a high uncertainty in the load measured by the strain gauge load cell while the motor is running. The strain gauge is more susceptible to electrical noise than other instruments because of its low voltage output (< 30 mV).

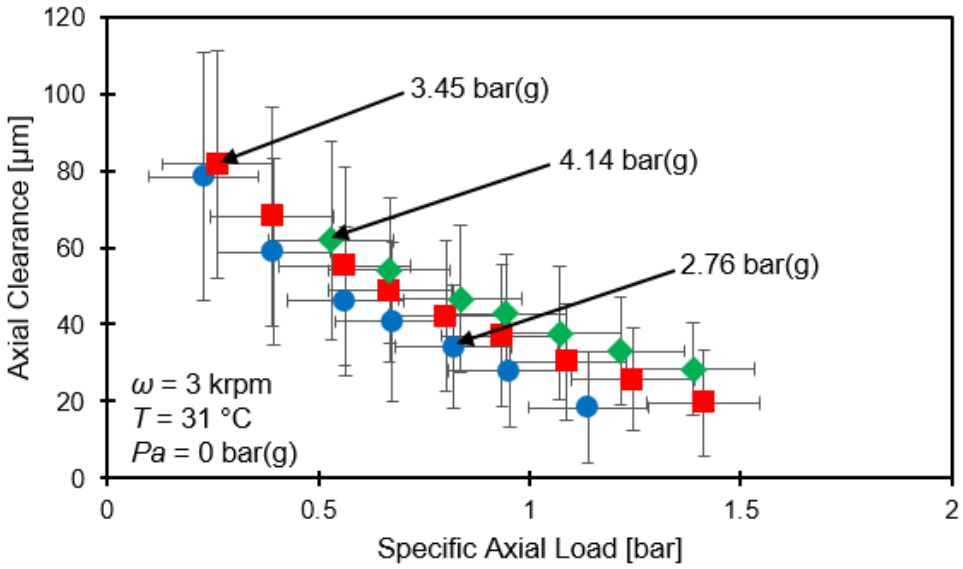

(a) Test Thrust Bearing

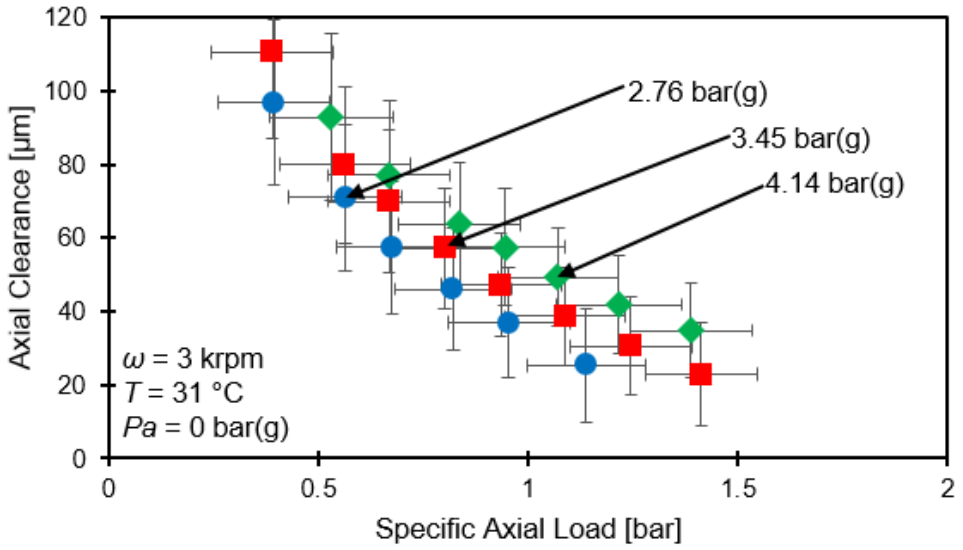

(b) Slave Thrust Bearing

Figure 33. Estimated axial clearance at the center of (a) test thrust bearing and (b) slave thrust bearing vs. specific load (*W/A*) for operation with water (31 °C) at a supply pressure (P_S) of 2.76, 3.45, and 4.14 bar(g) into the thrust bearing. Shaft rotates at 3 krpm. Water at 3.45 bar(g) feeds the journal bearings. Ambient pressure (P_a) is 0 bar(g). Horizontal error bars represent the uncertainty in the axial load at a 95% confidence level. Vertical error bars indicate the maximum and minimum clearances on the face of the thrust bearing.

Figure 34 shows the axial clearance at the center of the test and slave thrust bearings versus specific axial load, respectively, for operation at a rotor speed of 0 and 3 krpm as water at 2.76 bar(g), 3.45 bar(g), and 4.14 bar(g) supplies the thrust bearings, respectively. At each water supply pressure, the rotor speed does not have an effect on the axial clearance at a high axial clearance (low load). However, at a low axial clearance (high axial load), the thrust bearings operating with a rotor speed of 3 krpm operate at a slightly larger clearance. Overall, these figures show each thrust bearing operates mainly as a hydrostatic bearing. It should be noted that the water inlet temperature is several degrees cooler (7 °C) when measuring the thrust bearing performance at the zero rotor speed condition when compared to the measurements of thrust bearing performance at the low rotor speed (3 krpm) condition.

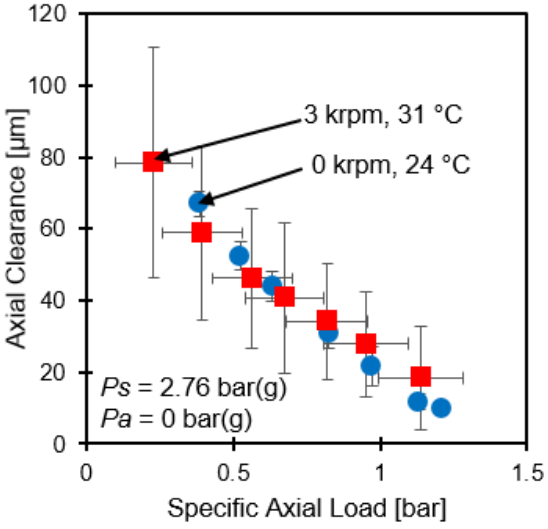

Test Thrust Bearing, P_S = 2.76 bar(g)

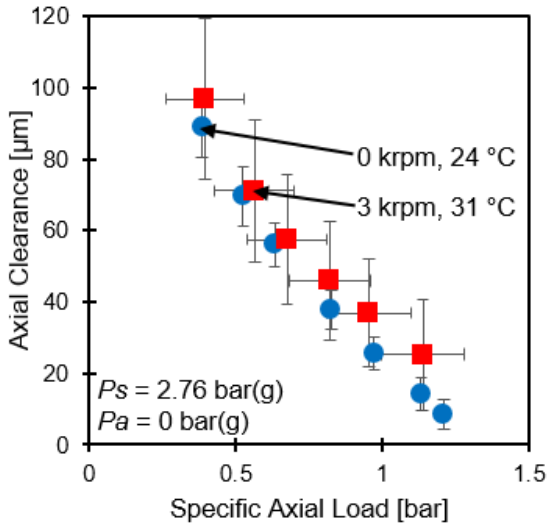

Slave Thrust Bearing, P_S = 2.76 bar(g)

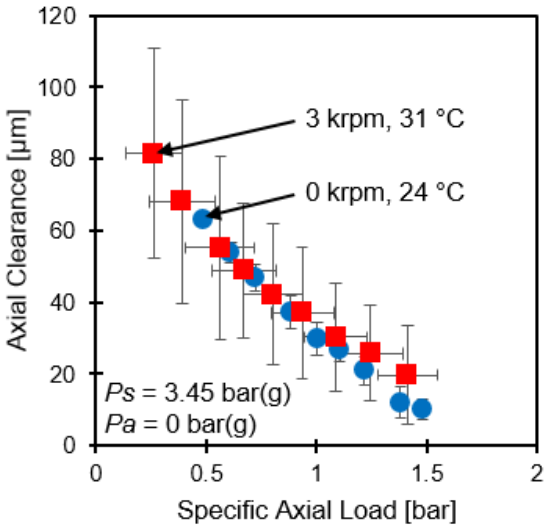

Test Thrust Bearing, P_S = 3.45 bar(g)

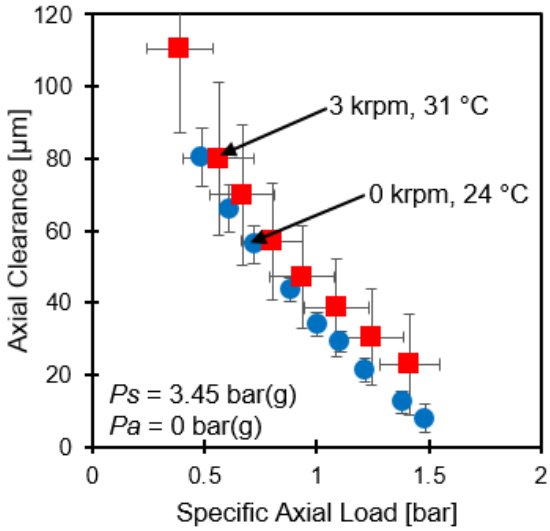

Slave Thrust Bearing, P_S = 3.45 bar(g)

Figure 34. Estimated axial clearance at the center of (left) test and (right) slave thrust bearings vs. specific load (*W/A*) for operation with water at a supply pressure (P_S) of 2.76, 3.45, and 4.14 bar(g) into the thrust bearing. Water is 24 °C and 31 °C as shaft rotates at 0 and 3 krpm, respectively. Water at 3.45 bar(g) feeds the journal bearings. Ambient pressure (P_a) is 0 bar(g). Horizontal error bars represent the uncertainty in the axial load at a 95% confidence level. Vertical error bars indicate the maximum and minimum clearances on the face of the thrust bearing.

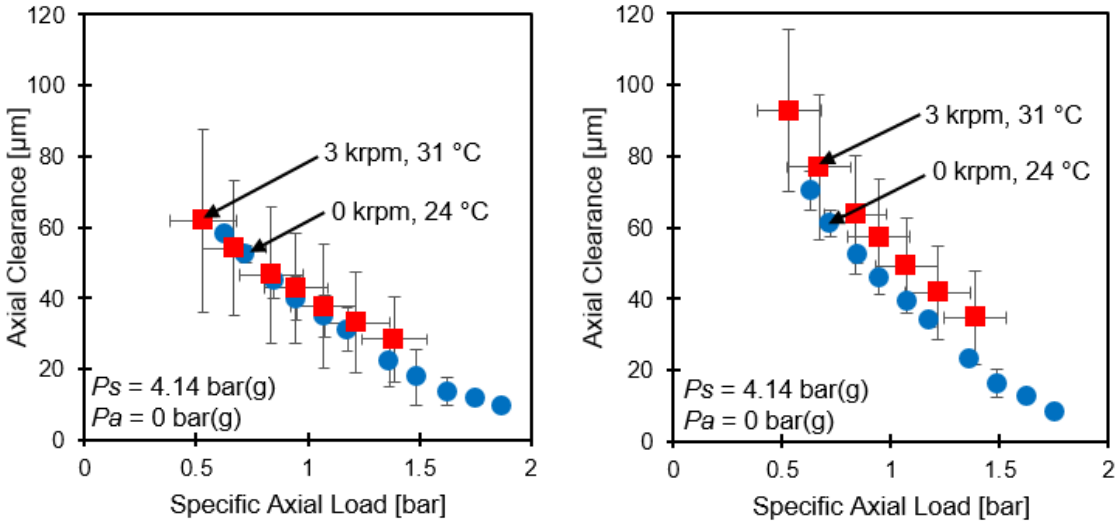

Test Thrust Bearing, P_S = 4.14 bar(g) **Slave Thrust Bearing, P_S = 4.14 bar(g)**

Figure 34. Continued.

For operation at 3 krpm, Figures 35-38 show the flow rate supplying the test thrust bearing (Q_S), the flow rate exhausting through the inner diameter of the test thrust bearing (Q_{ID}), the ratio of the flow exhausting from the inner diameter to the flow supplying the test thrust bearing (Q_{ID}/Q_s), and the recess pressure ratio (P_R/P_S) versus axial clearance at the center of the test thrust bearing, respectively, for operation with water at 2.76, 3.45, and 4.14 bar(g) supplying the thrust bearing. Note Figure 37 also shows the ratio of the flow exhausting from the inner diameter to the flow supplying the test thrust bearing (Q_{ID}/Q_s) versus specific axial load.

At a constant axial clearance, the flow rate supplying the thrust bearing and exhausting through the inner diameter of the thrust bearing increase as the water lubricant supply pressure increases. However, the magnitude of the water supply pressure does not affect

the ratio of flow exhausting through the inner diameter to the flow supplying the thrust bearing. At each water lubricant supply pressure, the flow rate supplying the thrust bearing and the flow rate exhausting though the inner diameter of the thrust bearing decrease as the axial clearance decreases because of the increased flow resistance across the (smaller thin) film lands of the thrust bearing. In addition, the ratio of flow exhausting through the inner diameter to the supply flow is fairly constant (~40%), decreasing slightly as the axial load increases (axial clearance decreases). A decrease in the flow rate causes a lower pressure drop across each orifice, resulting in higher pocket pressures at low axial clearance. At a constant axial clearance, the magnitude of the water supply pressure does not have a large influence on the recess pressure ratio while water supplies the bearing at 2.76-4.14 bar(g).

Figure 39 shows the radial Reynolds number of the flow exhausting from the inner and outer diameter of the thrust bearing versus axial clearance at the center of the test thrust bearing, respectively, for operation with water at 2.76, 3.45, and 4.14 bar(g) supplying the thrust bearings with the rotor spinning at 3 krpm. The radial Reynolds number of the radial flow through the inner diameter (Re_{ID}) is

$$Re_{ID} = \frac{\rho Q_{ID}}{\pi \mu D_{in}} \tag{3}$$

where Q_{ID} is the flow rate exhausting the thrust bearing through the inner diameter. The radial Reynolds number of the radial flow through the outer diameter (Re_{OD}) is

$$Re_{OD} = \frac{\rho Q_{OD}}{\pi \mu D_{out}} \tag{4}$$

where $Q_{OD} = Q_S - Q_{ID}$. Figure 39 indicates that the radial flow is laminar at the inner and outer diameter for operation at each water supply pressure and axial load. For operation at 3 krpm, the Reynolds number of the flow in the circumferential direction $\left(Re = \frac{\rho}{\mu}\omega RC\right)$ at the inner and outer diameters of the test thrust bearing increases from 160 to 650 and 300 to 1220, respectively, as the clearance increases from 20 μm to 80 μm. Note the Reynolds number of the flow in the circumferential direction is twice as high at the outer diameter compared to the inner diameter. At a constant axial clearance (constant applied load), Re_{ID} and Re_{OD} increase as the water lubricant supply pressure increases due to the increase in flow rate.

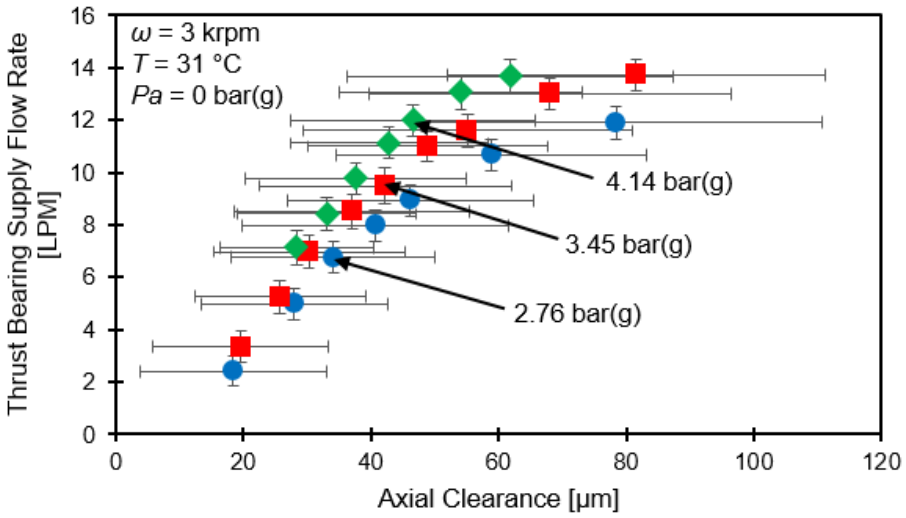

Figure 35. Measured supply flow rate of test thrust bearing vs. axial clearance at center of test thrust bearing for operation with water (31 °C) at a supply pressure (P_S) of 2.76, 3.45, and 4.14 bar(g) into the thrust bearing. Shaft rotates at 3 krpm. Water at 3.45 bar(g) feeds the journal bearings. Ambient pressure (P_a) is 0 bar(g). Vertical error bars represent the uncertainty in the supply flow rate at a 95% confidence level. Horizontal error bars indicate the maximum and minimum clearances on the face of the thrust bearing.

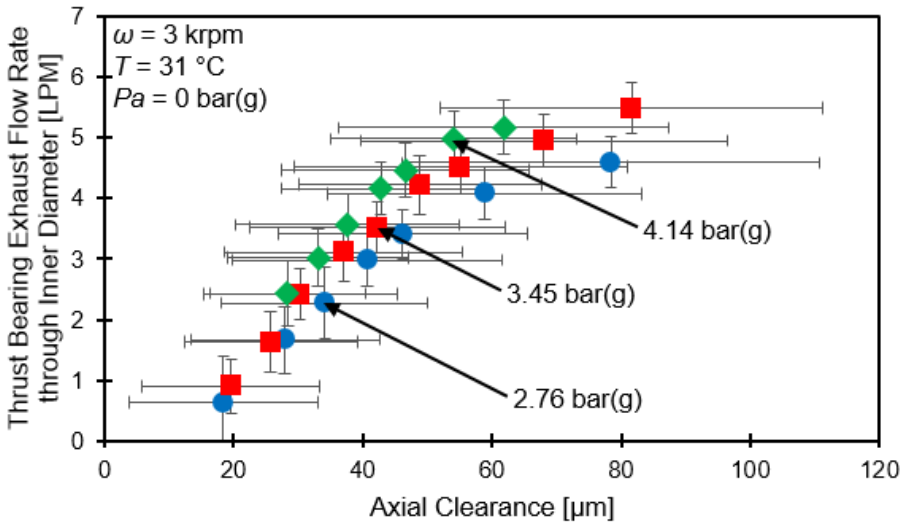

Figure 36. Measured exhaust flow rate through inner diameter of test thrust bearing vs. axial clearance at center of test thrust bearing for operation with water (31 °C) at a supply pressure (P_S) of 2.76, 3.45, and 4.14 bar(g) into the thrust bearing. Shaft rotates at 3 krpm. Water at 3.45 bar(g) feeds the journal bearings. Ambient pressure (P_a) is 0 bar(g). Vertical error bars represent the uncertainty in the flow rate through the inner diameter at a 95% confidence level. Horizontal error bars indicate the maximum and minimum clearances on the face of the thrust bearing.

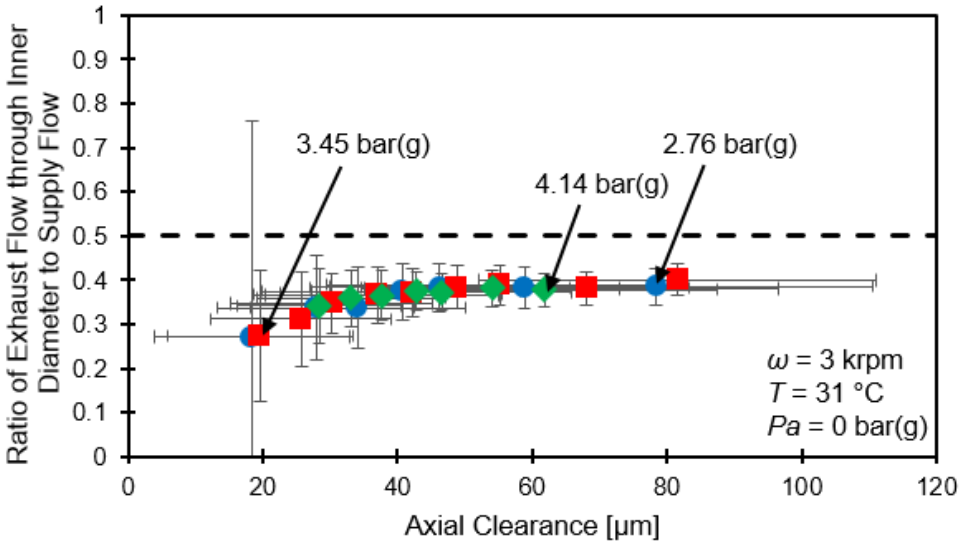

(a)

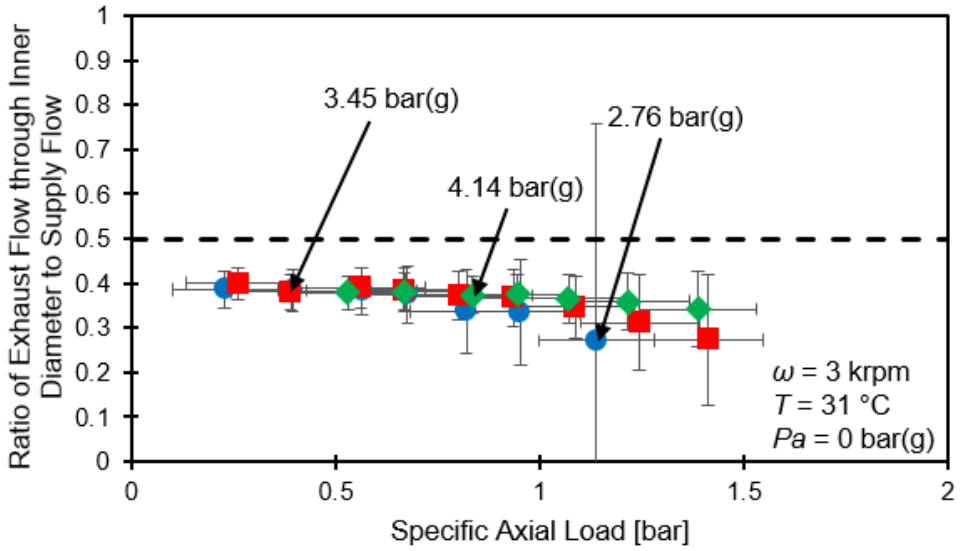

(b)

Figure 37. Ratio of exhaust flow through inner diameter to supply flow to test thrust bearing vs. (a) axial clearance at the center of the test thrust bearing and (b) specific axial load for operation with water (31 °C) at a supply pressure (P_S) of 2.76, 3.45, and 4.14 bar(g) into the thrust bearing. Shaft rotates at 3 krpm. Water at 3.45 bar(g) feeds the journal bearings. Ambient pressure (P_a) is 0 bar(g). Vertical error bars represent the uncertainty in the ratio of exhaust flow through inner diameter to supply flow at a 95% confidence level. Horizontal error bars indicate the maximum and minimum clearances on the face of the thrust bearing and the uncertainty in the specific axial load at a 95% confidence level, respectively.

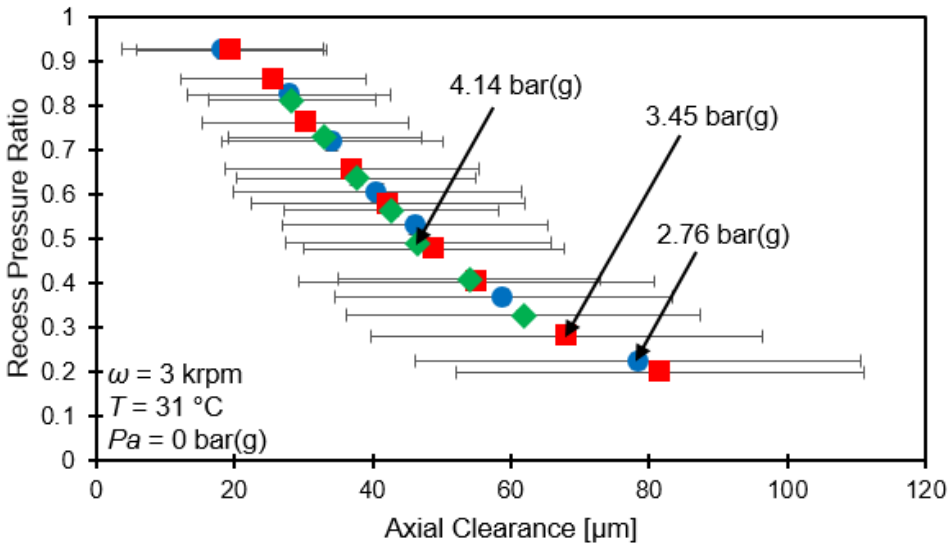

Figure 38. Derived recess pressure ratio (P_R/P_S) of test thrust bearing vs. axial clearance at center of test thrust bearing for operation with water (31 °C) at a supply pressure (P_S) of 2.76, 3.45, and 4.14 bar(g) into the thrust bearing. Shaft rotates at 3 krpm. Water at 3.45 bar(g) feeds the journal bearings. Ambient pressure (P_a) is 0 bar(g). Vertical error bars represent the uncertainty in the recess pressure ratio at a 95% confidence level. Horizontal error bars indicate the maximum and minimum clearances on the face of the thrust bearing.

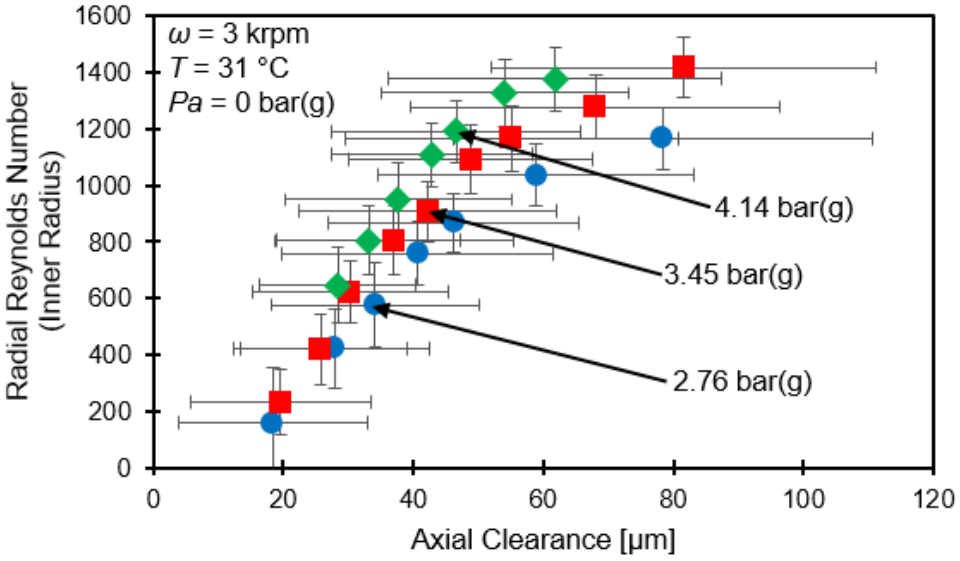

(a) Inner Diameter

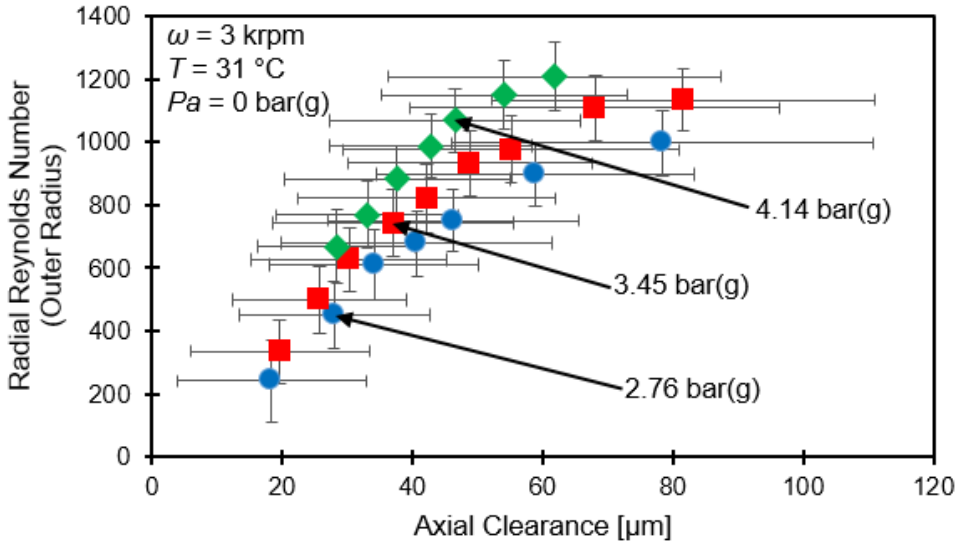

(b) Outer Diameter

Figure 39. Reynolds number of radial flow exhausting through the (a) inner and (b) outer diameter of the test thrust bearing vs. axial clearance at the center of the test thrust bearing for operation with water (31 °C) at a supply pressure (P_S) of 2.76, 3.45, and 4.14 bar(g) into the thrust bearing. Shaft rotates at 3 krpm. Water at 3.45 bar(g) feeds the journal bearings. Ambient pressure (P_a) is 0 bar(g). Vertical error bars represent the uncertainty in the Reynolds number at a 95% confidence level. Horizontal error bars indicate the maximum and minimum clearances on the face of the thrust bearing.

The flow through an orifice ($Q_O = Q_S / N_{pockets}$) is a function of its area (A_O), the pressure drop ($P_S - P_R$), and fluid density (ρ). From the data, one can obtain an empirical orifice discharge coefficient (C_d), as

$$C_d = \frac{Q_O}{A_O \sqrt{\frac{2}{\varrho}(P_S - P_R)}} \tag{4}$$

Note, Eq. (4) assumes the flow rate through all orifices is the same and the pressure in all recess is the same. Figure 40 shows the empirical discharge coefficient (C_d) versus axial clearance at the center of the test thrust bearing for operation with water at 2.76, 3.45, and 4.14 bar(g) supplying the thrust bearings as the rotor spins at 3 krpm. The magnitude of the water lubricant supply pressure does not have a large influence on C_d. However, the axial clearance does affect the orifice discharge coefficient. At a very low axial clearance, C_d is significantly lower and more uncertain than it is at a high axial clearance. As the axial clearance increases from 30 μm to 80 μm, C_d becomes relatively constant (~0.62), as shown in Table 5.

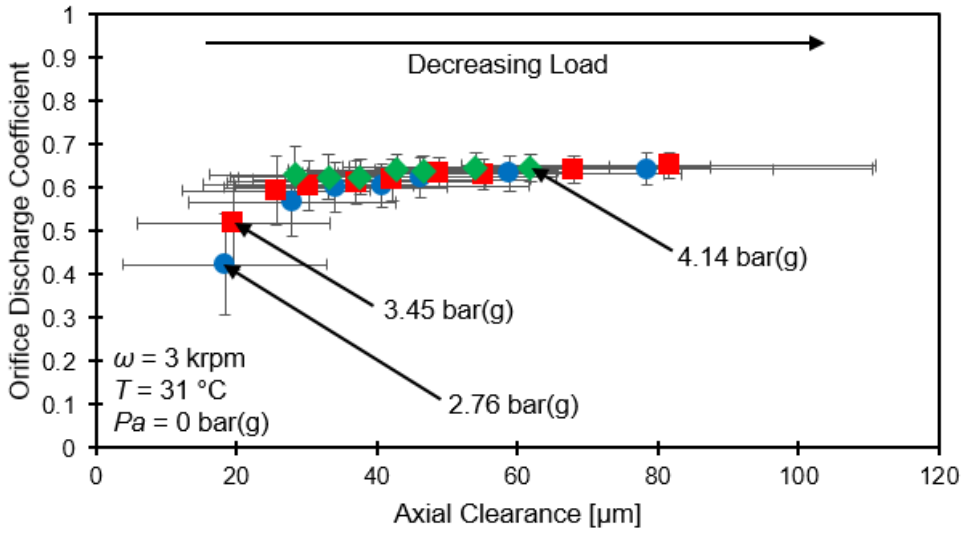

Figure 40. Empirical orifice discharge coefficient (C_d) vs. axial clearance at the center of the test thrust bearing for operation with water (31 °C) at a supply pressure (P_S) of 2.76, 3.45, and 4.14 bar(g) into the thrust bearing. Shaft rotates at 3 krpm. Water at 3.45 bar(g) feeds the journal bearings. Ambient pressure (P_a) is 0 bar(g). Vertical error bars represent the uncertainty in the empirical orifice discharge coefficient at a 95% confidence level. Horizontal error bars indicate the maximum and minimum clearances on the face of the thrust bearing.

Table 5. Estimated orifice discharge coefficient (C_d) for test thrust bearing operating with water (31 °C) at a supply pressure (P_S) of 2.76, 3.45, and 4.14 bar(g). Shaft rotates at 3 krpm. Water at 3.45 bar(g) feeds the journal bearings. Ambient pressure (P_a) is 0 bar(g). Uncertainty in the estimated orifice discharge coefficient is based on a 95% confidence level.

Water Supply Pressure (P_S)	Estimated Orifice Discharge Coefficient (C_d)
2.76 bar(g)	0.61 ± 0.07
3.45 bar(g)	0.62 ± 0.05
4.14 bar(g)	0.64 ± 0.02

Using the geometry of the thrust bearing and the average discharge coefficients shown in Table 5, XLHydroThrust® [11] predicts the bearing performance (C, Q_S, P_R, K) as a function of an applied axial load. Appendix C describes the input data required for XLHydoThrust® [11] as well as the performance parameters that it predicts. Figure 41

shows the predicted axial clearance and estimated axial clearance at the center of the thrust bearing for both the test and slave thrust bearing versus the specific axial load (*W/A*) for operation with water supplying the thrust bearing at 2.76, 3.45, and 4.14 bar(g) with the rotor spinning at 0 krpm and 3 krpm, respectively. Note that the predictions assume the orifices on the slave thrust bearing have the same discharge coefficient as the orifices on the test thrust bearing. However, there are no measurements for either the flow rate or recess pressure in the slave thrust bearing.

Figures 42-44 show the measured and predicted thrust bearing supply flow rate, exhaust flow rate through the inner diameter, and the recess pressure ratio (P_R/P_S) versus specific axial load (*W/A*), respectively, for operation with water (31 °C) supplying the thrust bearings at 2.76, 3.45, and 4.14 bar(g) as the rotor spins at 3 krpm.

The measured and predicted axial clearance increase as the water pressure supplied to the thrust bearing increases or the applied axial load decreases. The predicted axial clearance is consistently much larger than the estimated, experimental axial clearance at the center of the thrust bearing, especially when operating with a high axial load (low axial clearance). However, at a low axial load (high axial clearance), the maximum clearance on the face of the thrust collar is nearly equivalent to the predicted clearance when the rotor spins at 3 krpm. As the applied axial load increases (axial clearance decreases) from its minimum to its maximum magnitude (rotor spins at 3 krpm), the average percent difference in axial clearance increases from 25% to 53%. Thus, as the applied axial load increases (axial clearance decreases), the difference between the predicted and estimated axial clearances becomes more significant.

As the applied axial load decreases and the axial clearance increases, the flow resistance across the film land decreases resulting in a higher supply flow rate and a higher exhaust flow rate through the inner diameter of the thrust bearing for a constant water supply pressure. As the flow rate supplied to the thrust bearing increases, the flow experiences a larger pressure drop through the orifice resulting in a lower recess pressure. As the water pressure supplied to the thrust bearing increases at a constant applied axial load, the flow rate supplying the thrust bearing and exhausting through the inner diameter of the thrust bearing also increases, causing the recess pressure to decrease. The predictions accurately show the influence of the water supply pressure and specific axial load on the supply flow rate, the exhaust flow rate through the inner diameter, and the recess pressure ratio.

The predicted magnitudes of the thrust bearing supply flow rate, exhaust flow rate through the inner diameter, and recess pressure ratio versus specific axial load correlate well with the corresponding measured values at a low specific load (large axial clearance). However, the predicted magnitudes do not correlate well at a high specific load (low axial clearance). As the load increases from its minimum to maximum load (axial clearance decreases) at each supply pressure (rotor spins at 3 krpm), the average percent difference between the predicted and measured supply flow rate, flow rate through the inner diameter, and recess pressure ratio increases from 2% to 47%, 7% to 73%, and 7% to 18%, respectively. Overall, the predicted magnitudes show discrepancies with the measured magnitudes at high axial loads (low axial clearances). The misalignment of the thrust collar relative to the thrust bearing could have a magnified effect at a low axial clearance.

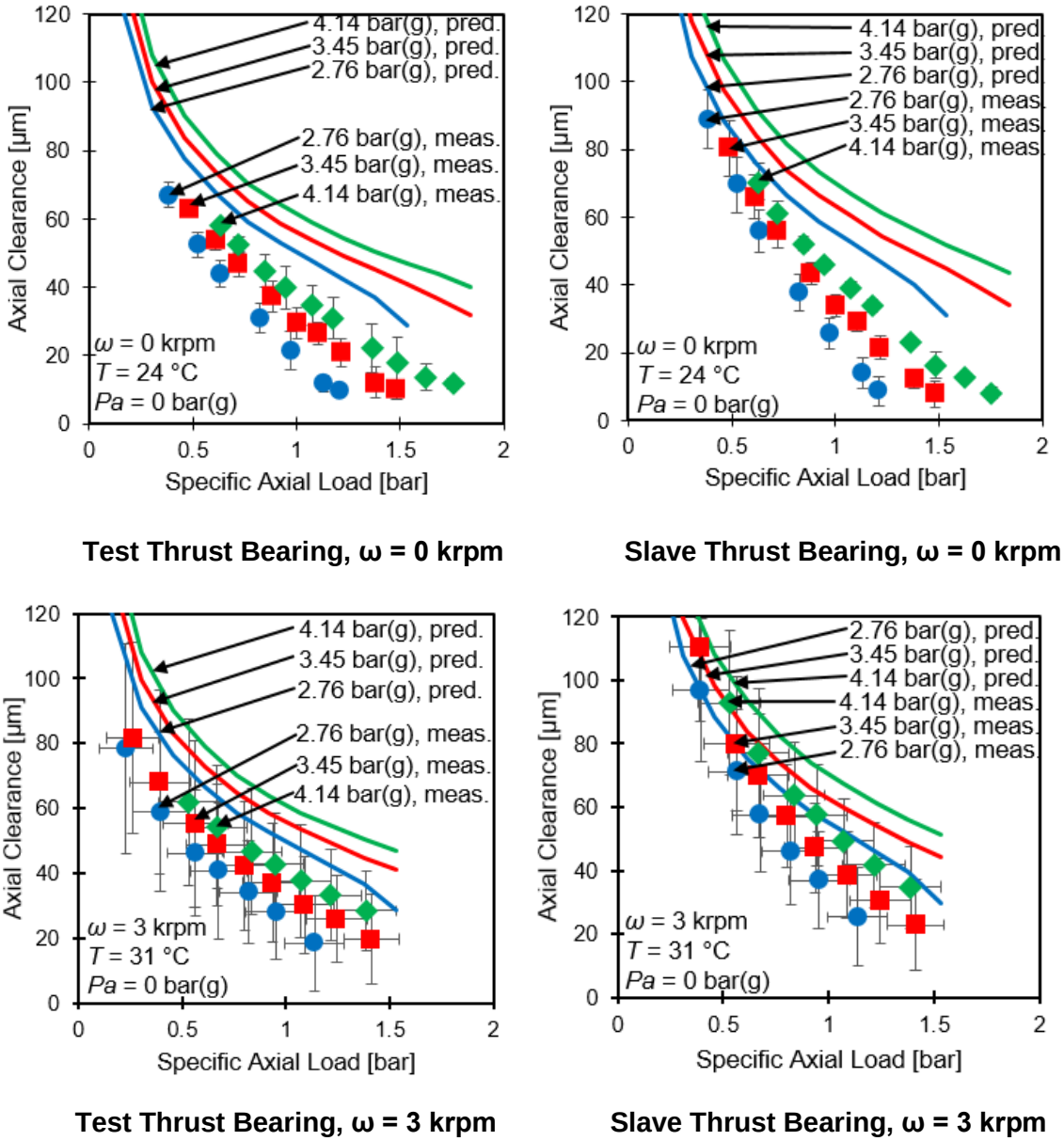

Figure 41. Measured and predicted axial clearance at center of (left) test thrust bearing and (right) slave thrust bearing vs. specific load (*W/A*) for operation with water at a supply pressure (P_s) of 2.76, 3.45, and 4.14 bar(g) into the thrust bearing. Shaft rotates at (top) 0 krpm and (bottom) 3 krpm. Water at 3.45 bar(g) feeds the journal bearings. Ambient pressure (P_a) is 0 bar(g). Horizontal error bars represent the uncertainty in the specific axial load at a 95% confidence level. Vertical error bars indicate the maximum and minimum clearances on the face of the thrust bearing.

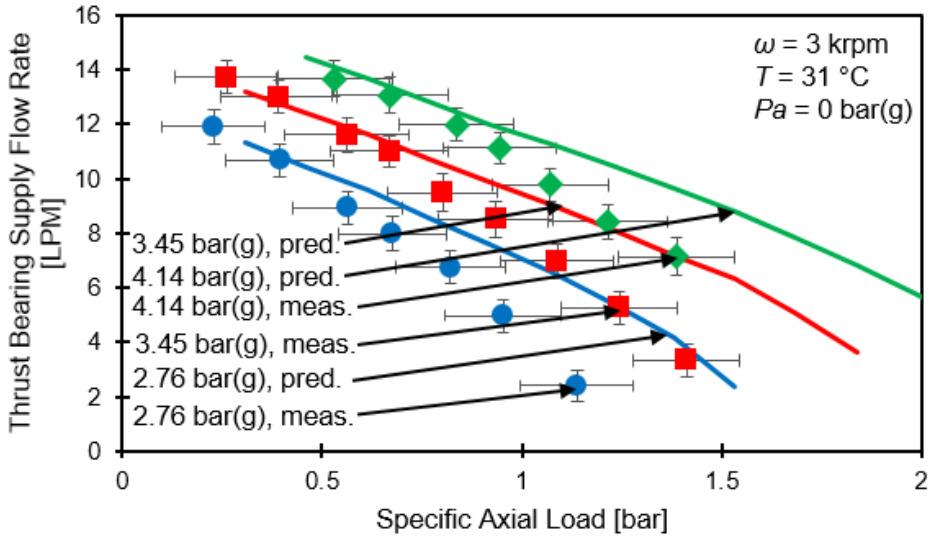

Figure 42. Measured and predicted thrust bearing supply flow rate vs. specific axial load for operation with water (31 °C) at a supply pressure (P_S) of 2.76, 3.45, and 4.14 bar(g) into the thrust bearing. Shaft rotates at 3 krpm. Water at 3.45 bar(g) feeds the journal bearings. Ambient pressure (P_a) is 0 bar(g). Vertical and horizontal error bars represent the uncertainty in the supply flow rate and the specific axial load at a 95% confidence level, respectively.

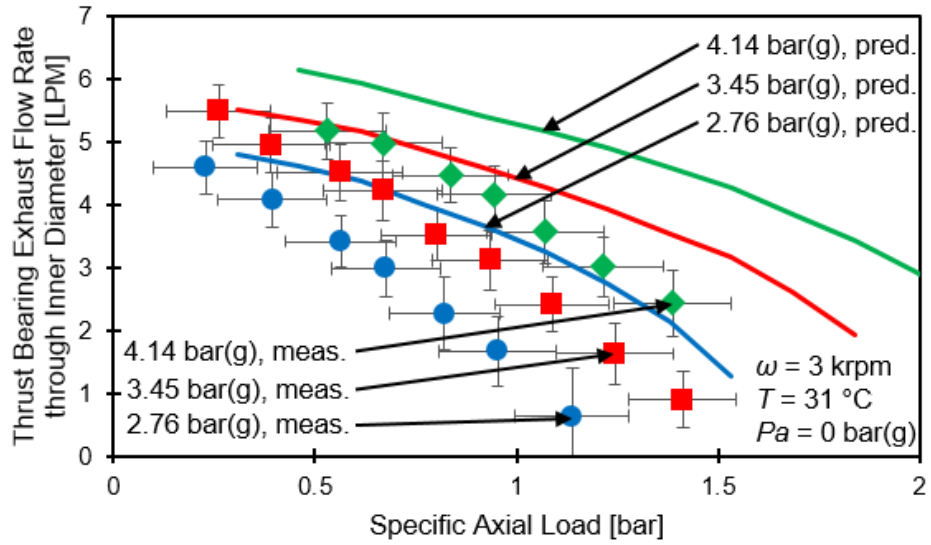

Figure 43. Measured and predicted thrust bearing flow rate through inner diameter vs. specific axial load for operation with water (31 °C) at a supply pressure (P_S) of 2.75, 3.45, and 4.14 bar(g) into the thrust bearing. Shaft rotates at 3 krpm. Water at 3.45 bar(g) feeds the journal bearings. Ambient pressure (P_a) is 0 bar(g). Vertical and horizontal error bars represent the uncertainty in the exhaust flow rate through the inner diameter and the uncertainty in the specific axial load at a 95% confidence level, respectively.

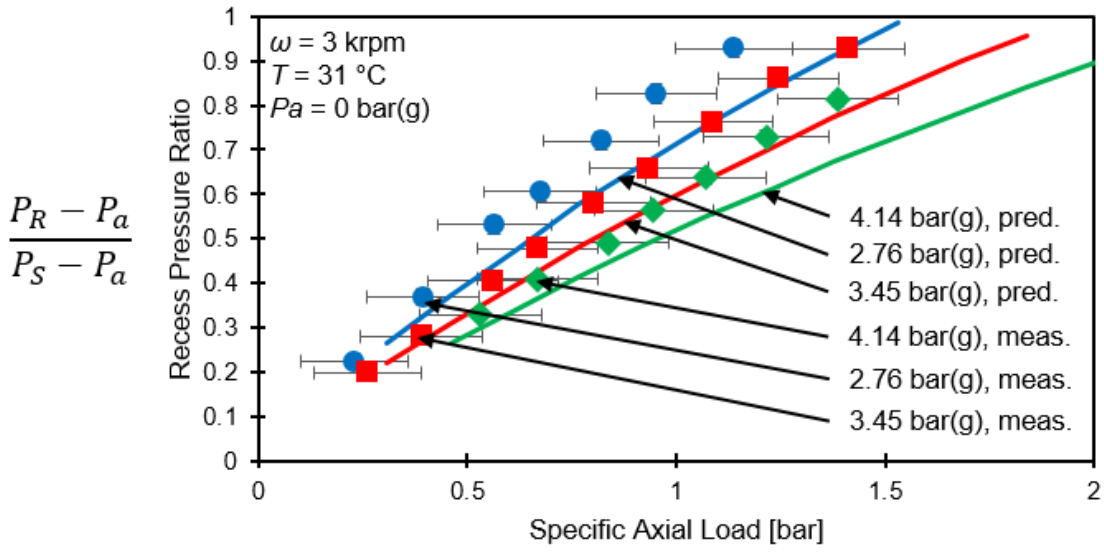

Figure 44. Measured and predicted recess pressure ratio vs. specific axial load for operation with water (31 °C) at a supply pressure (P_S) of 2.76, 3.45, and 4.14 bar(g) into the thrust bearing. Shaft rotates at 3 krpm. Water at 3.45 bar(g) feeds the journal bearings. Ambient pressure (P_a) is 0 bar(g). Vertical and horizontal error bars represent the uncertainty in the recess pressure ratio and the specific axial load at a 95% confidence level, respectively.

Figure 45 shows the axial load vs clearance and an exponential curve fit (function derivative provides an estimate of the static stiffness). Figure 46 shows the derived static stiffness versus the axial clearance for operation with water (31 °C) supplying the thrust bearing at 2.76, 3.45, and 4.14 bar(g). The rotor spins at 3 krpm. At a constant axial clearance, the axial stiffness and the load capacity increase as the water pressure supply increases. With a constant water lubricant supply pressure, the load capacity and axial stiffness decrease as the axial clearance increases.

As the clearance continues to increase, the load capacity and axial stiffness approach zero. The estimated axial stiffness is on the same order of magnitude as the predicted axial

stiffness. However, the estimated axial stiffness shows a high magnitude at a lower axial clearance than the predicted axial stiffness. Note that estimated axial stiffness, shown on Figure 46, is only valid for the range of clearances shown and cannot be extrapolated to any higher or lower axial clearance.

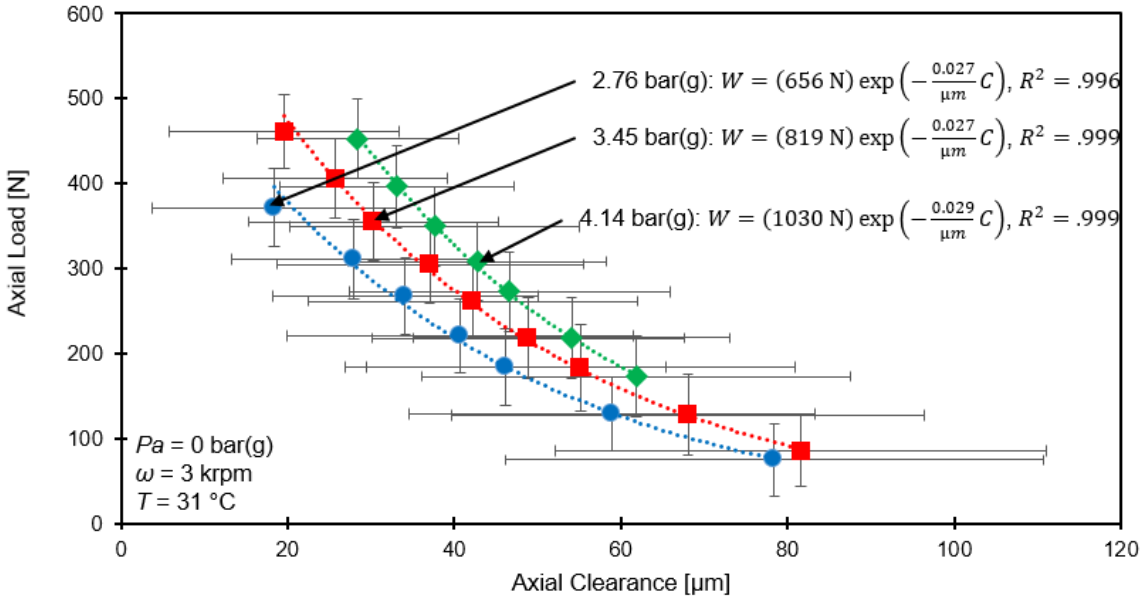

Figure 45. Measured axial load vs. axial clearance at the center of the test thrust bearing with exponential curve fit ([*C*]=µm, [*W*]=N) for operation with water (31 °C) at a supply pressure (P_S) of 2.76, 3.45, and 4.14 bar(g) into the thrust bearings. Shaft rotates at 3 krpm. Water at 3.45 bar(g) feeds the journal bearings. Ambient pressure (P_a) is 0 bar(g). Vertical error bars represent the uncertainty in the axial load at a 95% confidence level. Horizontal error bars indicate the maximum and minimum clearances on the face of the thrust bearing.

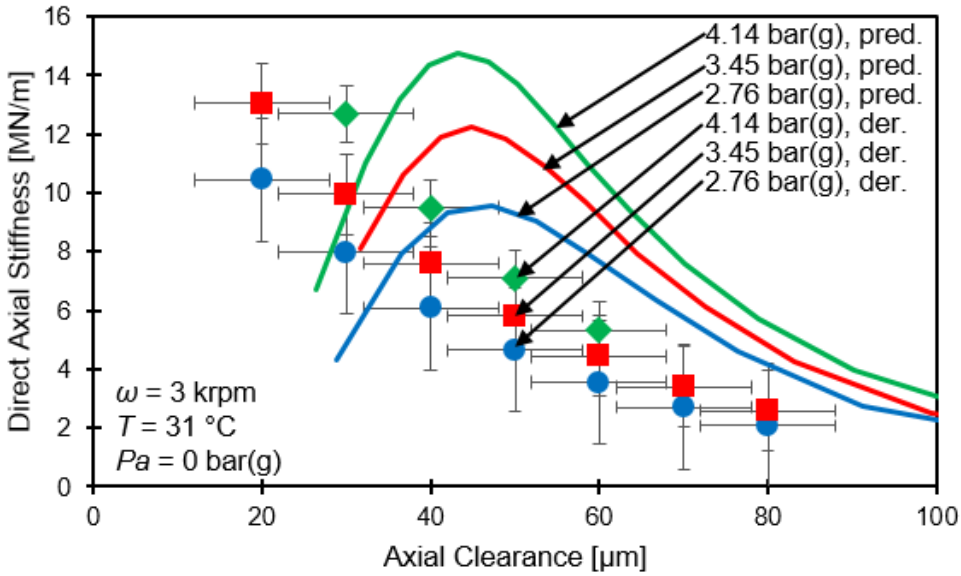

Figure 46. Derived and predicted axial stiffness vs. axial clearance at the center of the test thrust bearing for operation with water (31 °C) at a supply pressure (P_S) of 2.76, 3.45, and 4.14 bar(g) into the thrust bearings. Shaft rotates at 3 krpm. Water at 3.45 bar(g) feeds the journal bearings. Ambient pressure (P_a) is 0 bar(g). Estimated axial stiffness derived from exponential curve fit (shown in Figure 45). Vertical and horizontal error bars represent the uncertainty in the axial stiffness and the axial clearance at the center of the test thrust bearing at a 95% confidence level, respectively.

CONCLUSION

After a catastrophic failure in 2013, the thrust bearing test rig underwent extensive repairs and is presently operating with water as a lubricant. The rig is ready to provide experimental results to validate model predictions. The end objective of this work is to improve the design of thrust bearings. Previously, measurements on the same test rig showed remarkable correlation with predictions for water lubricated hybrid thrust bearings [3].

A number of modifications and enhancements were enacted on the thrust bearing test rig. A diagnostic procedure with the original rotor showed that the thrust collars are not orthogonal with the shaft centerline. Hence, a new stainless steel rotor was machined, balanced, and installed. A drill/tap process removed the remnant material from the housing, enabling the housing to hold air buffer seals and eddy current sensors. The refurbished water pipeline manifold has presently an increased inner diameter to minimize frictional losses in the fluid as it flows to supply the bearings. The motor shaft centerline and rotor centerline are presently aligned within the coupling vendor specifications using the face and rim alignment method. The instrumentation is in place with multiple eddy current sensors, various turbine flow meters, static pressure transducers, an optical tachometer, a strain gauge load cell, and a thermocouple. The sensors monitor the operating conditions of the test rig.

Measurements of the free-free mode natural frequencies and mode shapes of the rotor-coupling assembly show that the rotor and quill shaft operate as a single unit, and hence must be considered as such for an accurate rotordynamic analysis. With the test rig

completely assembled, water (24 °C) supplies the radial bearings at increasing supply pressure (max. 6 bar(g)) for operation without rotor speed or active thrust bearings. Impact loads are exerted on the quill shaft, and lateral displacements of the rotor-coupling assembly help to identify the rotor-coupling-radial bearing system fundamental natural frequency and damping ratio. The natural frequency increases little (91 Hz to 95 Hz) as the water supply pressure increases (2 bar(g) to 6 bar(g)) because the flexibility of the quill shaft commands the placement of the natural frequency. The damping ratio is rather low because the flexible quill shaft has no external damping. However, the damping ratio increases from 4.8% to 6.8% as the water supply pressure increases (2 bar(g) to 6 bar(g)). XLTRC^2® predictions agree well with the measured natural frequency and identified damping ratio.

Water (24 °C) supplies the journal bearings at increasing supply pressure (max. 5.5 bar(g)) for operation without active thrust bearings (slave bearing operates with minimal supply pressure to prevent contact with the rotor). The motor accelerates the rotor to 5 krpm (83 Hz). For operation with water at a supply pressure of 3.45, 4.48, and 5.52 bar(g) and rotor speed up to 5 krpm, the rotor displacement is synchronous. As the rotor speed increases towards 5 krpm, the amplitude of rotor motion increases, but the system does not reach its first critical speed. An increase in supply pressure aids in restricting lateral rotor motions.

Without and with low (3 krpm) shaft speed, water at room temperature (24 °C and 31 °C) feeds the journal bearings at 3.45 bar(g) and the thrust bearings at increasing supply pressure (max. 4.14 bar(g)). At each water lubricant supply pressure into the thrust

bearings, the test thrust bearing applies a decreasing load onto the rotor thrust collar. At a constant axial load, the axial clearance, the supply flow rate, and the central exhaust flow rate increase as the pressure of the water supplying the thrust bearing increases. However, the axial load per unit area [$A = \frac{\pi}{4}(D_{out}^2 - D_{in}^2)$] is a fraction of the supply pressure (P_S) to thrust bearings because the recess area is only a fraction of the load bearing area. At a constant supply pressure (P_S), the axial clearance (C) decreases as the axial load (W) increases. The reduced clearance causes an increased flow resistance across the film lands of the thrust bearing, ultimately amounting to a reduced flow rate at a high axial load (low axial clearance). As the flow rate decreases, the pressure drop across the orifice also decreases, which results in higher recess pressures. Therefore, as the axial load increases (axial clearance decreases) with a constant water lubricant supply pressure, the supply flow rate and the flow rate through the inner diameter decrease as the recess pressure ratio increases. In addition, as the axial clearance decreases or the water supply pressure increases, the axial load and stiffness increase. Overall, the measurements show to be repeatable but not accurate.

XLHydroThrust® [11] used the bearing geometry to calculate predictions of bearing performance. The predictions and measurements qualitatively agree on how the water supply pressure/axial load affect the bearing performance. However, there are discrepancies between the predicted and measured magnitudes at a high axial load (small axial clearance). At the lowest axial load for each water supply pressure administered to the test thrust bearing (3 krpm), the average percent difference between the predicted and measured supply flow rate, flow rate through inner diameter, axial clearance, and the

recess pressure ratio is 2%, 7%, 25%, and 18%, respectively. At the highest axial load for each water supply pressure on the test thrust bearing (3 krpm), the average percent difference between the predicted and measured supply flow rate, flow rate through inner diameter, axial clearance, and recess pressure ratio is 47%, 73%, 53%, and 18%, respectively. The discrepancy at low axial clearance is caused by the large thrust collar misalignment having a more dramatic influence at a small axial clearance.

Future work will measure the performance of a hybrid thrust bearing (eight pocket) lubricated with water. The test rig could also be used to test other thrust bearings with a 7.6-cm outer diameter at speeds up to 9 krpm ($\omega R_{out} = 35.9$ m/s). The first task will be to measure the axial response from single frequency axial loads over a range of rotor speed (max. 9 krpm), bearing supply pressure (max. 10 bar), thrust bearing clearance (min. 25 μm), and excitation frequency (max. 150 Hz). The second task is to estimate the thrust bearing stiffness and damping coefficients from transfer functions.

A recommendation for future work is to supply the radial bearings and the thrust bearings with water at a higher supply pressure (> 10 bar), so the bearings will restrict the rotor motion more effectively and lower the uncertainty in thrust collar face misalignment.

REFERENCES

[1] San Andrés, L., 2013, "A Test Rig for Evaluation of Thrust Bearings and Face Seals," Proposal to the Turbomachinery Research Consortium, Turbomachinery Laboratory, Texas A&M University, College Station, TX, May.

[2] Forsberg, M., 2008, "Comparison Between Predictions and Experimental Measurements for an Eight Pocket Annular HTB," M.S. Thesis, Mechanical Engineering, Texas A&M University, College Station, TX.

[3] Esser, P., 2010, "Measurements versus Predictions for a Hybrid (Hydrostatic plus Hydrodynamic) Thrust Bearing for a Range of Orifice Diameters," M.S. Thesis, Mechanical Engineering, Texas A&M University, College Station, TX.

[4] Rohmer, M. and San Andrés, L., 2014, "Revamping a Thrust Bearing Test Rig," Annual Progress Report to the Turbomachinery Research Consortium, TRC-B&C-03-2014, Turbomachinery Laboratory, Texas A&M University, College Station, TX, May.

[5] San Andrés, L., 2010, *Modern Lubrication Theory*, "Hydrostatic Journal Bearings," Notes 12b, Texas A&M University Digital Libraries, http://repository.tamu.edu/handle/1969.1/93197.

[6] Rowe, W., 1983, *Hydrostatic and Hybrid Bearing Design*, Textbook, Butterworths, London, England, pp. 1-20, 46-68.

[7] Sternlicht, B. and Elwell, R.C., 1960, "Theoretical and Experimental Analysis of Hydrostatic Thrust Bearings," ASME J. Basic Eng., **82**(3), pp. 505-512.

[8] Fourka, M. and Bonis, M., 1997, "Comparison between Externally Pressurized Gas Thrust Bearings with Different Orifice and Porous Feeding Systems," Wear, **210**(1-2), pp. 311-317.

[9] Belforte, G., Colombo, F., Raparelli, T., Trivella, A., and Viktorov, V., 2010, "Performance of Externally Pressurized Grooved Thrust Bearings," Tribol. Lett., **37**, pp. 553-562.

[10] San Andrés, L., 2000, "Bulk-Flow Analysis of Hybrid Thrust Bearings for Process Fluid Applications," ASME J. of Trib., **122**(1), pp. 170-180.

[11] San Andrés, L., 2002, "Effects of Misalignment on Turbulent Flow Hybrid Thrust Bearings," ASME J. of Trib., **124**(1), pp. 212-219.

[12] San Andrés, L., Phillips, S., and Childs, D., 2008, "Static Load Performance of a Hybrid Thrust Bearing: Measurement and Validation of Predictive Tool," 6th Modeling and Simulation Subcommittee / 4th Liquid Propulsion Subcommittee / 3rd Spacecraft Propulsion Subcommittee Joint Meeting. December 8-12, Orlando, Florida, JANNAF-120 Paper.

[13] Ramirez, F., 2008, "Comparison between Predictions and Measurements of Performance Characteristics for an Eight Pocket Hybrid (Combination Hydrostatic/Hydrodynamic) Thrust Bearing," M.S. Thesis, Mechanical Engineering, Texas A&M University, College Station, TX.

[14] XLTRC^2, 2002, Computational Rotordynamics Software Suite, Turbomachinery Laboratory, Texas A&M University, College Station, TX.

[15] San Andrés, L. and Childs, D., 1997, "Angled Injection – Hydrostatic Bearings, Analysis and Comparison to Test Results," ASME J. Tribol., **119**, pp. 179-187.

[16] San Andrés, L., Rohmer, M., and Park, S., 2015, "Failure of a Test Rig Operating with Pressurized Gas Bearings: A Lesson on Humility," ASME paper GT2015-42556.

[17] San Andrés, L. and Rohmer, M., 2014, "Measurements and XLTRC^2 Predictions of Mass Moments of Inertia, Free-Free Natural Frequencies and Mode Shapes of Rotor and Flexible Coupling," Internal Progress Report, *Turbomachinery Laboratory, Texas A&M University*, March.

[18] Coleman, H. and Steel, W., 1989, *Experimentation and Uncertainty Analysis for Engineers*, Textbook, John Wiley and Sons, Inc., New York, NY, pp. 1-71.

APPENDIX A: DESCRIPTION OF TAMU THRUST BEARING TEST RIG [12]

Figures 47 and 48 show a cross-sectional view and a photograph of the thrust bearing test rig, respectively. The test rotor is a long stainless steel shaft with two stainless steel thrust collars at its ends. Two flexure pivot type radial hydrostatic bearings support the test rotor (to avoid potential hydrodynamic instability induced by shaft rotation), whose center of mass is located between the two radial bearings.

The test rig has two water lubricated hydrostatic thrust bearings; one is the test bearing (on the right of Figure 47) and the other is a slave bearing, both facing the outer side of the thrust collars on the rotor. The slave thrust bearing is affixed rigidly to a bearing support, as shown on the left of Figure 47. A load device (not shown), through a non-rotating shaft, delivers a static axial load to the test thrust bearing. Two aerostatic radial bearings support the axial load shaft with minimal friction for motions in the axial direction. The test thrust bearing, depicted on the right of Figure 47, moves axially to impose a load on the rotor thrust collar. This axial load is also reacted by the slave thrust bearing. Figure 49 depicts a schematic view of the test rig with its bearings as mechanical elements providing stiffness and damping for load support and energy dissipation, respectively. Ref. [4] provides full details on the major components of the test rig.

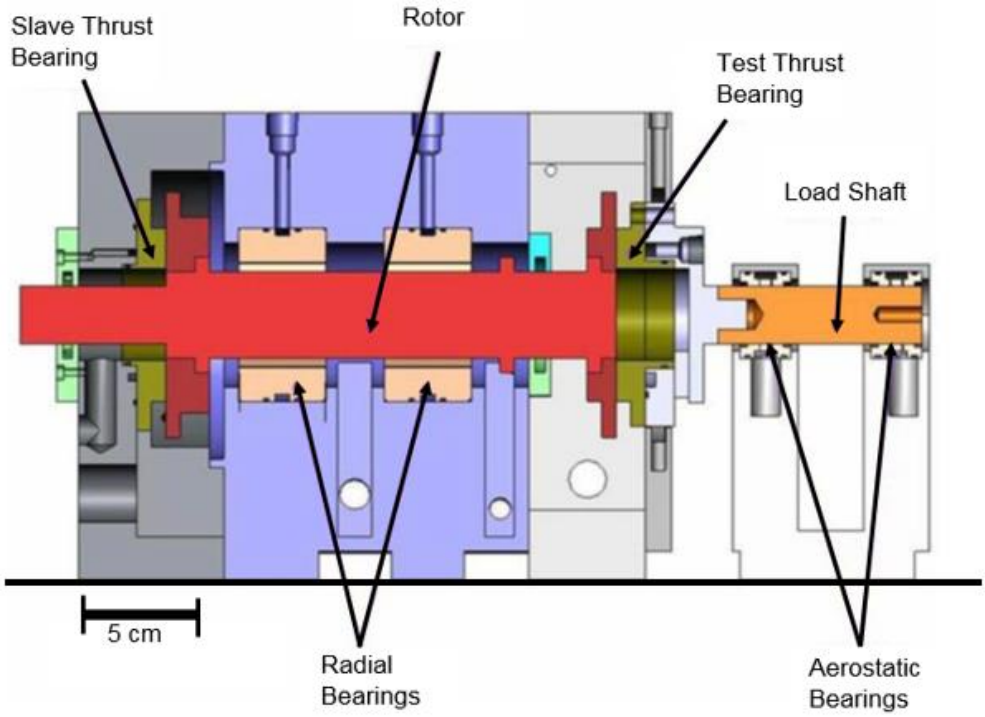

Figure 47. Cross sectional view of thrust bearing test rig. Reprinted from [12].

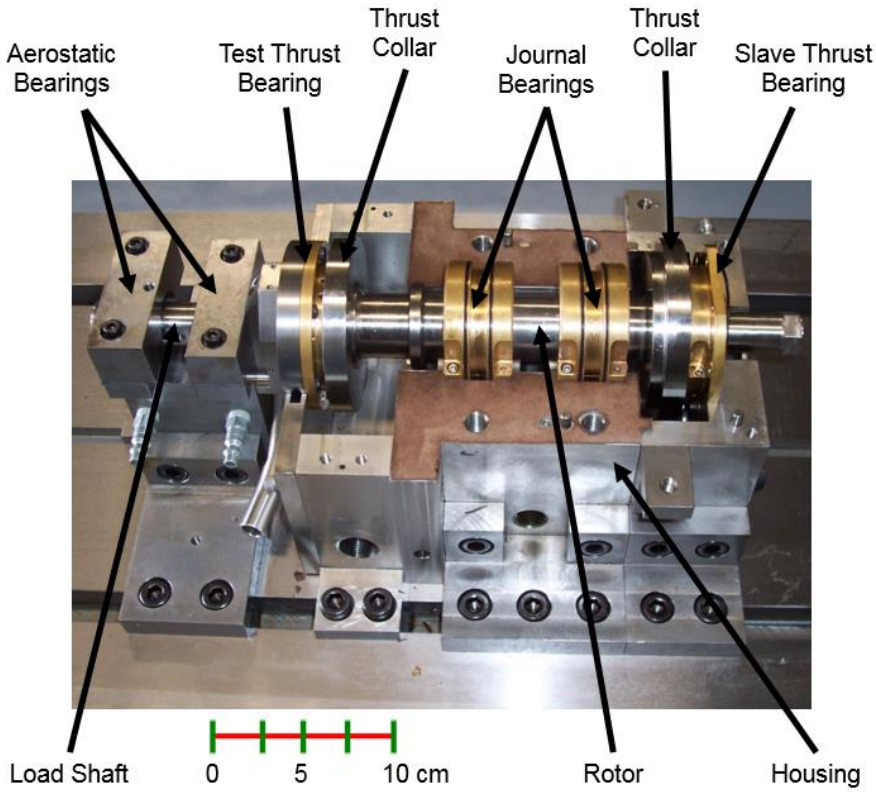

Figure 48. Photograph of hydrostatic thrust bearing test rig (2006). Reprinted from [16].

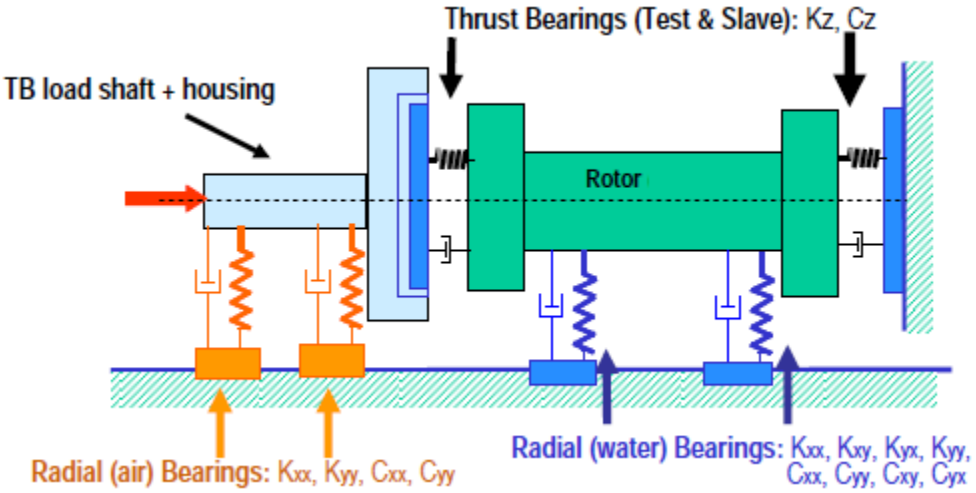

Figure 49. Schematic representation of test rig: thrust and radial bearings as mechanical elements with stiffness and damping characteristics. Reprinted from [3].

APPENDIX B: PROCEDURE FOR MEASURING ROTOR FREE-FREE MODE SHAPES AND NATURAL FREQUENCIES [17]

Figure 50 shows the (ad-hoc) set up to measure the free-free mode natural frequencies and mode shapes of the rotor-coupling assembly. Two inextensible strings suspend the rotor-coupling assembly. The strings provide negligible stiffness in the direction orthogonal to their length. Wax affixes two 1 gram piezoelectric accelerometers to the rotor. One reference accelerometer remains stationary on the assembly, while the other accelerometer roams to various positions on the rotor-coupling assembly.

An impact hammer strikes the rotor-coupling assembly and excites it. The dynamic signal analyzer records the amplitude of acceleration, the natural frequency, and the phase angle between the two accelerometers. The dynamic signal analyzer averages the response of twenty-five impulses. Wax affixes the roaming accelerometer to nineteen other locations, and the process listed above is repeated. The relative amplitudes and phase angles between the two accelerometers at different locations determine the mode shape at each natural frequency.

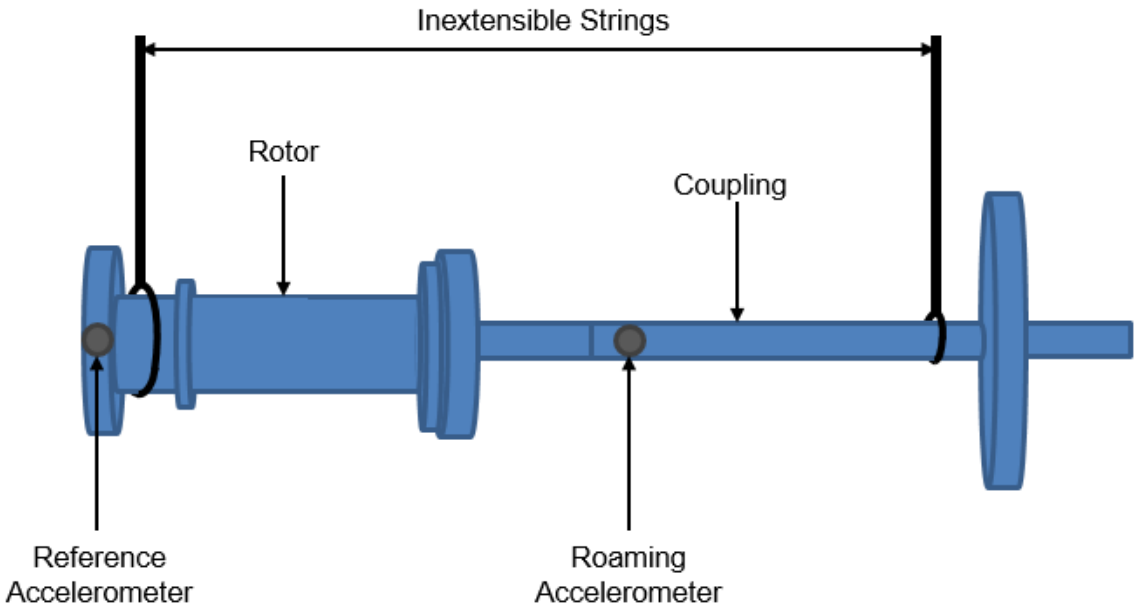

Figure 50. Schematic view of rotor-coupling assembly suspended with two accelerometers mounted to measure free-free mode natural frequencies and mode shapes of the system.

APPENDIX C: PREDICTIVE CODES FOR BEARING PERFORMANCE

In this thesis, XLHydroJet® and XLHydroThrust® predict the force coefficients as well as other performance parameters for hydrostatic journal bearings and hydrostatic thrust bearings, respectively. Tables 6 and 7 show the required inputs and the outputs for XLHydroJet® [15] and XLHydroThrust® [11], respectively. XLHydroJet® links with XLTRC^2® [14], a rotordynamic suite, to produce predictions for a rotordynamic system, such as natural frequency, damping ratio, and imbalance response.

Table 6. Required inputs and outputs for XLHydoJet® [15].

Inputs	Outputs
Bearing Geometry	Stiffness (Direct and Cross-Coupled)
Pad Geometry	Damping (Direct and Cross-Coupled)
Pocket Geometry	Added Mass (Direct and Cross-Coupled)
Orifice Geometry	Impedances (Direct and Cross-Coupled)
Lubricant Properties	Static Eccentricity
Thermal Options	Mass Flow Rate
Supply Pressure	Static Reaction Force
Exit Pressure	Power Loss
Rotor Speed	Equivalent Stiffness
Excitation Frequency	Whirl Frequency Ratio
Static Load/Static Eccentricity	Drag Torque
Fluid Inertia Presence	Maximum Pressure
Mesh Size	Maximum Temperature

Table 7. Required inputs and outputs for XLHydroThrust® [11].

Inputs	Outputs
Bearing Geometry	Force and Moment Stiffness (Direct and Angular Displacements)
Pad Geometry	Force and Moment Damping (Direct and Angular Displacements)
Pocket Geometry	Force and Moment Added Mass (Direct and Angular Displacements)
Orifice Geometry	Clearance
Lubricant Properties	Mass Flow Rate
Thermal Options	Static Reaction Force
Supply Pressure	Power Loss
Exit Pressure	Equivalent Stiffness
Rotor Speed	Whirl Frequency Ratio
Excitation Frequency	Drag Torque
Static Load/Clearance	Maximum Pressure
Fluid Inertia Presence	Maximum Temperature
Mesh Size	

APPENDIX D: REPEATABILITY OF MEASUREMENTS

During three separate tests, Figures 51-53 show the specific axial load, supply flow rate, and the recess pressure ratio versus axial clearance, respectively, for operation with water (31 °C) at 3.45 bar(g) supplying the radial and thrust bearings as the rotor spins at 3 krpm. Each of these figures demonstrates the repeatability of the tests; thus, evidencing that the results are not dependent on a particular trial.

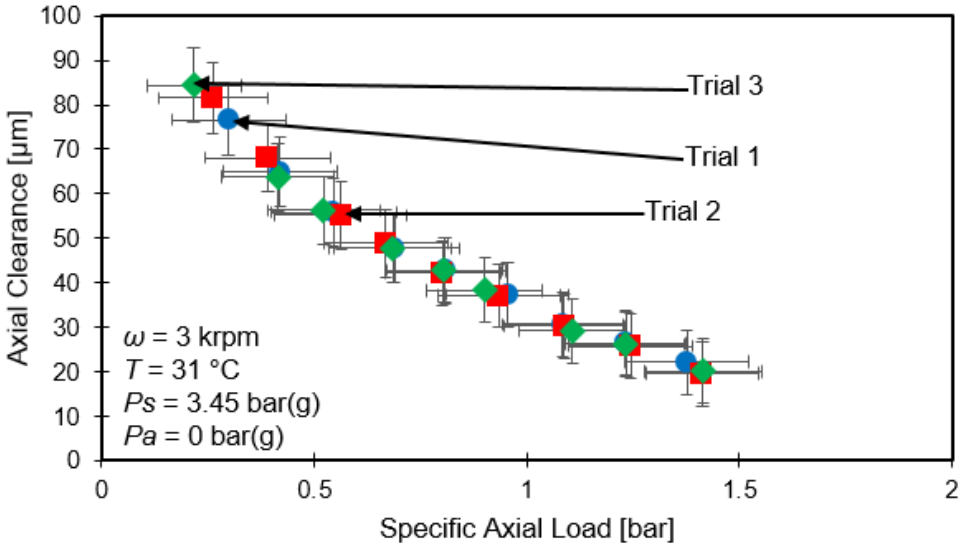

Figure 51. Measured axial clearance of test thrust bearing vs. specific load (*W/A*) for operation with water (31 °C) at a supply pressure (P_S) of 3.45 bar(g) into the thrust bearing. Shaft rotates at 3 krpm. Figure shows three separate trials. Water at 3.45 bar(g) feeds the journal bearings. Ambient pressure (P_a) is 0 bar(g). Vertical and horizontal error bars represent the uncertainty in the axial clearance and the specific axial load at a 95% confidence level, respectively.

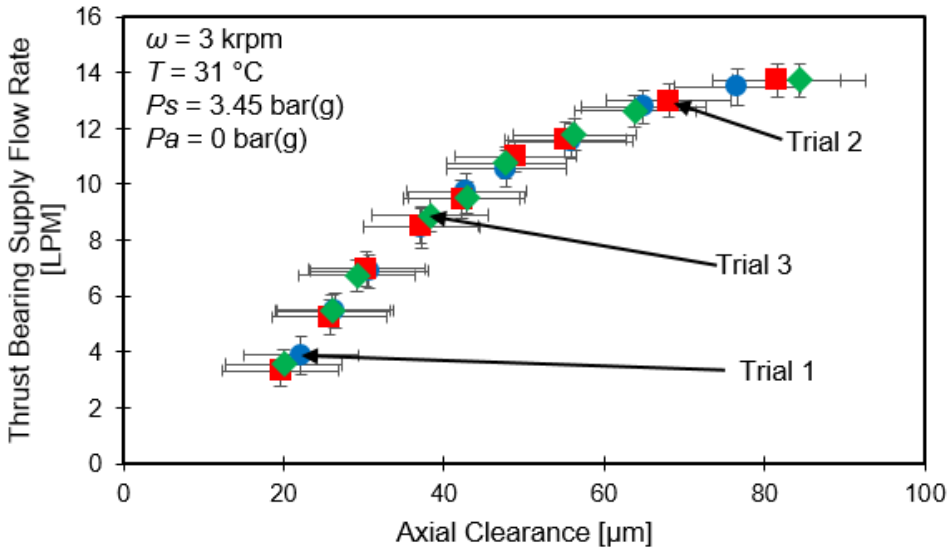

Figure 52. Measured thrust bearing supply flow rate vs. axial clearance for operation with water (31 °C) at a supply pressure (P_S) of 3.45 bar(g) into the thrust bearing. Shaft rotates at 3 krpm. Figure shows three separate trials. Water at 3.45 bar(g) feeds the journal bearings. Ambient pressure (P_a) is 0 bar(g). Vertical and horizontal error bars represent the uncertainty in the thrust bearing supply flow rate and the axial clearance at a 95% confidence level, respectively.

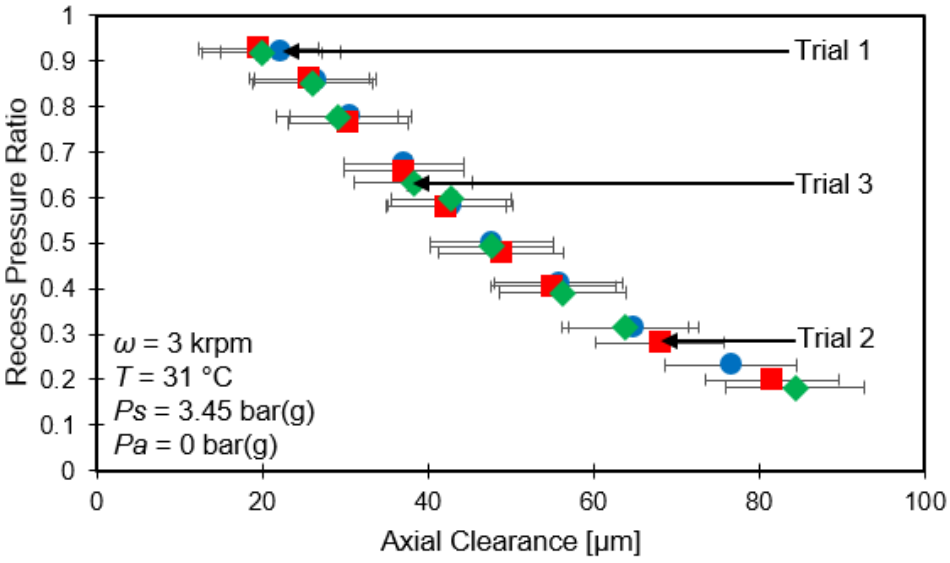

Figure 53. Measured recess pressure ratio vs. axial clearance for operation with water (31 °C) at a supply pressure (P_S) of 3.45 bar(g) into the thrust bearing. Shaft rotates at 3 krpm. Figure shows three separate trials. Water at 3.45 bar(g) feeds the journal bearings. Ambient pressure (P_a) is 0 bar(g). Vertical and horizontal error bars represent the uncertainty in the recess pressure ratio and the axial clearance at a 95% confidence level, respectively.

APPENDIX E: ROTOR THRUST COLLAR PLANE EQUATION DERIVATION AND UNCERTAINTY ANALYSIS [2]

Thrust Collar Plane Equation Derivation

Forsberg [2] prepared the following original analysis. Eddy current sensors face a thrust collar and measure the axial gap between the thrust collar and thrust bearing surface at three circumferential locations, as shown in Figure 54. Using the gap clearances and the geometry to determine the clearance between the thrust collar and the thrust bearing surface at the center of the thrust bearing and the tilt of the thrust collar relative to the thrust bearing is critical in order to estimate the thrust bearing performance.

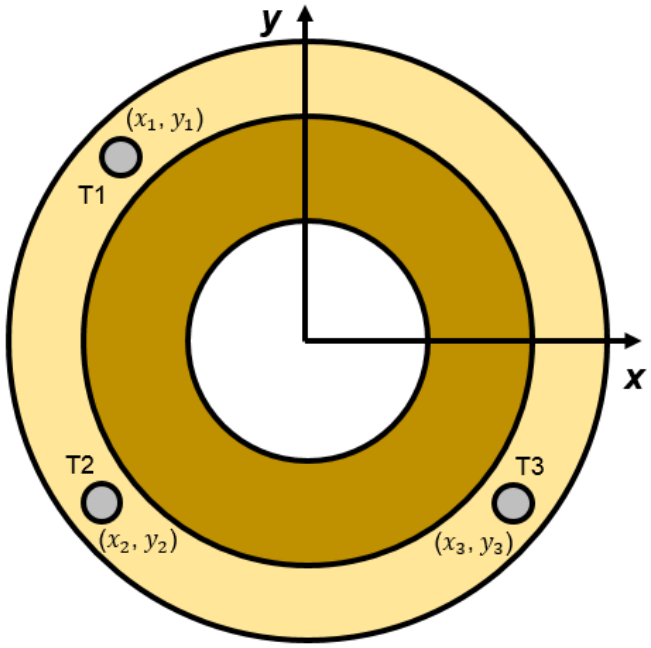

Figure 54. Schematic view of position of eddy current sensors on test thrust bearing.

Table 8 describes the horizontal and vertical position of each eddy current sensor relative to the center of the thrust bearing.

Table 8. Horizontal and vertical positions of each eddy current sensor relative to the center of the thrust bearing.

	x	*y*
Probe T1	x_1 = -33.02 mm	y_1 = 27.69 mm
Probe T2	x_2 = -37.34 mm	y_2 = -21.59 mm
Probe T3	x_3 = 37.34 mm	y_3 = -21.59 mm

Assuming the thrust bearing and the thrust collar act as rigid planes, the gap between the thrust collar and the thrust bearing surface at each eddy current sensor can be used with the position of each eddy current sensor to determine the equation of the plane of the rotor thrust collar relative to the thrust bearing. Table 9 describes three points on the rotor thrust collar plane relative to the surface of the thrust bearing using the three gap measurements from the eddy current sensors. In Table 9, z_1, z_2, and z_3 represent the gap between the thrust collar and the thrust bearing at Points T1, T2, and T3 on the thrust collar, respectively.

Table 9. Coordinates of three points on the rotor thrust collar plane relative to the thrust bearing using gap measurements from the eddy current sensors.

Point on Thrust Collar	Coordinates on Thrust Collar (*x*,*y*,*z*)
Point T1	(x_1, y_1, z_1)
Point T2	(x_2, y_2, z_2)
Point T3	(x_2, y_2, z_3)

Figure 55 shows that the coordinates of the three points on the thrust collar plane can be used to generate two vectors located on the rotor thrust collar plane. One vector ($\vec{V}_{12}$) defines the displacement from Point T1 to Point T2 on the thrust collar plane. The other vector ($\vec{V}_{13}$) defines the displacement from Point T1 to Point T3 on the thrust collar plane.

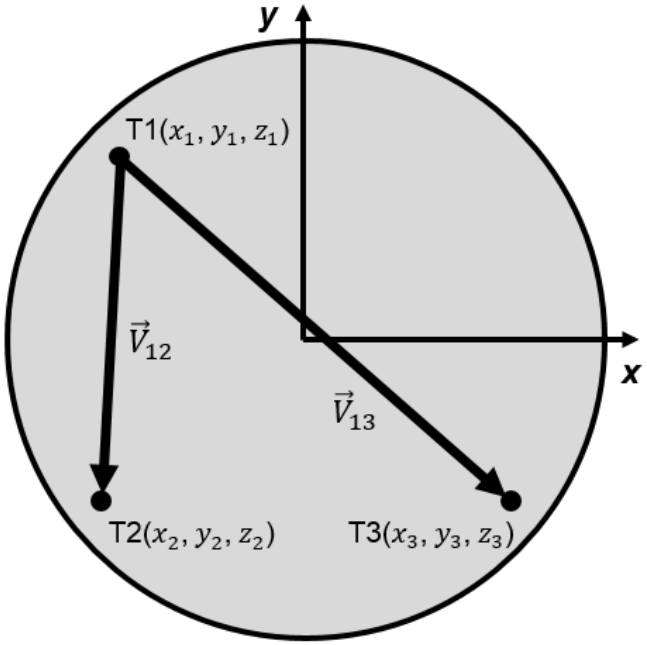

Figure 55. Two vectors produced from three points located on rotor thrust collar plane.

$$\vec{V}_{12} = \text{Point T2} - \text{Point T1} = (x_2 - x_1)\hat{\imath} + (y_2 - y_1)\hat{\jmath} + (z_2 - z_1)\hat{k}$$

$$\vec{V}_{13} = \text{Point T3} - \text{Point T1} = (x_3 - x_1)\hat{\imath} + (y_3 - y_1)\hat{\jmath} + (z_3 - z_1)\hat{k}$$

The cross product of two vectors produces a vector that is orthogonal to each vector. Therefore, if two vectors lie on the same plane, then the cross product of these two vectors

produces a vector that is orthogonal to that plane. Hence, the normal vector ($\vec{N}$) of the thrust collar plane is defined as the resultant cross product of $\vec{V}_{12}$ and $\vec{V}_{13}$ (see Figure 56).

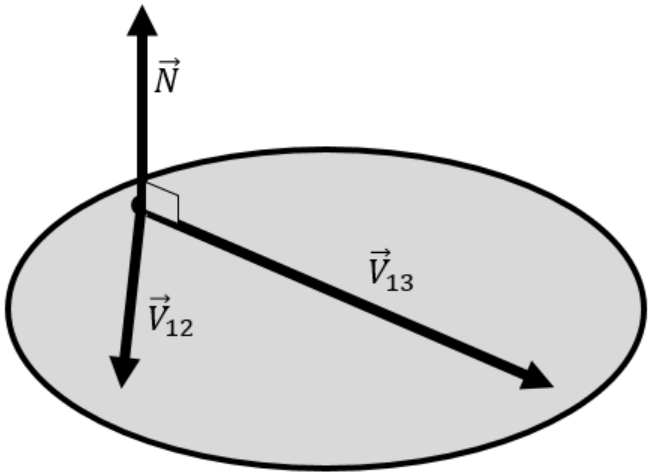

Figure 56. Normal vector produced from cross product of two vectors on rotor thrust collar plane.

$$\vec{N} = \vec{V}_{12} \times \vec{V}_{13}$$

$$\vec{N} = a\hat{\imath} + b\hat{\jmath} + c\hat{k}$$

Where

$$a = (y_2 - y_1)(z_3 - z_1) - (y_3 - y_1)(z_2 - z_1)$$

$$b = (z_2 - z_1)(x_3 - x_1) - (x_2 - x_1)(z_3 - z_1)$$

$$c = (x_2 - x_1)(y_3 - y_1) - (y_2 - y_1)(x_3 - x_1)$$

A generic vector ($\vec{V}_{gen}$) defines the displacement from Point T1 to a generic point (*x*, *y*, *z*) on the rotor thrust collar plane.

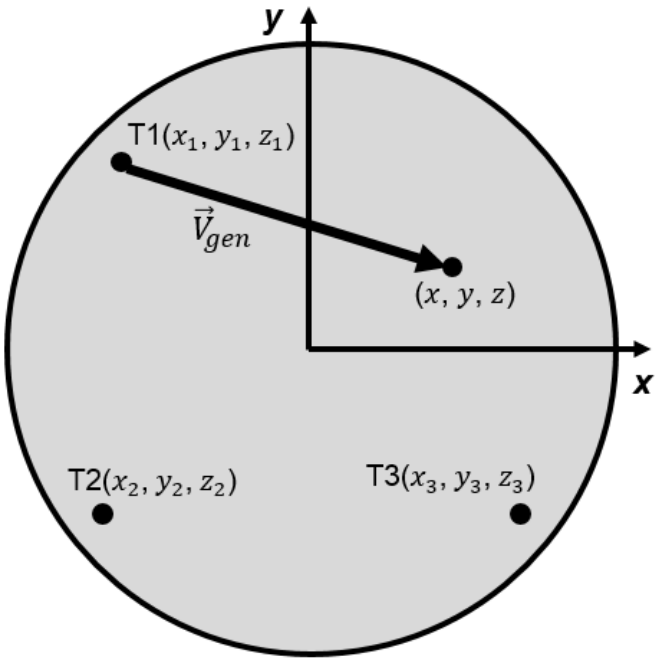

Figure 57. Generic vector on the rotor thrust collar plane.

$$\vec{V}_{gen} = \text{Generic Point} - \text{Point T1} = (x - x_1)\hat{\imath} + (y - y_1)\hat{\jmath} + (z - z_1)\hat{k}$$

The normal vector ($\vec{N}$) and the generic vector ($\vec{V}_{gen}$) must be orthogonal (see Figure 58). Therefore, the dot product of the normal vector ($\vec{N}$) and the generic vector ($\vec{V}_{gen}$) must equal zero. Hence, equating the dot product of the normal vector ($\vec{N}$) and the generic vector ($\vec{V}_{gen}$) to zero defines the equation of the plane.

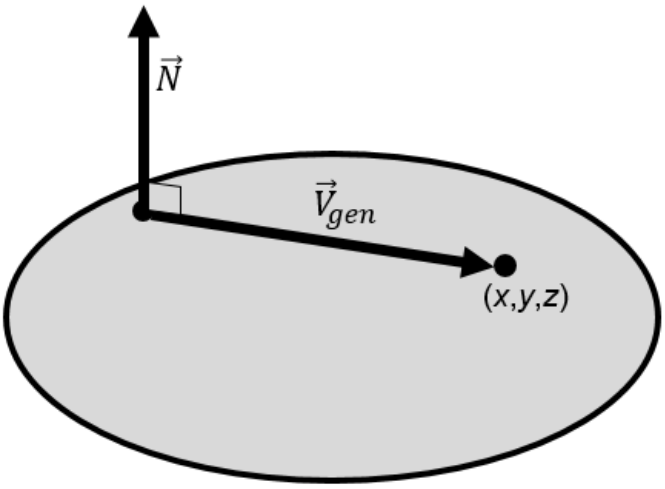

Figure 58. Generic vector and normal vector on rotor thrust collar plane.

$$0 = \vec{N} \cdot \vec{V}_{gen}$$

$$0 = a(x - x_1) + b(y - y_1) + c(z - z_1)$$

$$ax + by + cz = ax_1 + by_1 + cz_1$$

The equation of the thrust collar plane can be reduced into a more useful form (shown below) that shows the clearance at the center of the thrust bearing (C_0) as well as the tilt of the rotor thrust collar about the *x*-axis (δ_x) and *y*-axis (δ_y) relative to the thrust bearing. With the equation of the thrust collar plane in its reduced form, the axial clearance between the thrust collar and the thrust bearing can be determined at any point on the thrust collar surface.

$$z(x, y) = \frac{ax_1 + by_1 + cz_1 - ax - by}{c}$$

$$z(x, y) = C_0 + \delta_y x + \delta_x y$$

Uncertainty Analysis of Clearance and Misalignment between Rotor Thrust Collar and Thrust Bearing [18]

The allowable run out in each thrust collar is 5 μm. Therefore, there will be an uncertainty of ±5 μm when defining the null clearance at each eddy current sensor and an uncertainty of ±5 μm when measuring the clearance at each sensor, equating to a total bias uncertainty of ±10 μm for each eddy current sensor. The Kline McClintock method, shown below, determine the bias uncertainty in the axial clearance at the center of the thrust bearing (β_{C_0}) and the bias uncertainty in the tilt of the thrust collar about the *x*-axis (β_{δ_x}) and *y*-axis (β_{δ_y}) relative to the thrust bearing based off the bias uncertainty in each sensor ($\beta_{z_1}, \beta_{z_2}, \beta_{z_3}$).

$$\beta_{C_0} = \sqrt{\left(\frac{dC_0}{dz_1}\beta_{z_1}\right)^2 + \left(\frac{dC_0}{dz_2}\beta_{z_2}\right)^2 + \left(\frac{dC_0}{dz_3}\beta_{z_3}\right)^2}$$

$$\beta_{\delta_x} = \sqrt{\left(\frac{d\delta_x}{dz_1}\beta_{z_1}\right)^2 + \left(\frac{d\delta_x}{dz_2}\beta_{z_2}\right)^2 + \left(\frac{d\delta_x}{dz_3}\beta_{z_3}\right)^2}$$

$$\beta_{\delta_y} = \sqrt{\left(\frac{d\delta_y}{dz_1}\beta_{z_1}\right)^2 + \left(\frac{d\delta_y}{dz_2}\beta_{z_2}\right)^2 + \left(\frac{d\delta_y}{dz_3}\beta_{z_3}\right)^2}$$

The standard of deviation and the t-Distribution Table determine the precision uncertainty of each measurement at a 95% confidence level.

$$\xi = t_{\alpha=0.025, df=1000} * \sigma$$

Where

ξ = Precision uncertainty based off 95% confidence level

σ = Standard of deviation

$t_{\alpha=0.025,df=1000}$ = t-table factor for 1000 degrees of freedom at a 95% confidence level

The root sum square of the precision uncertainty and the bias uncertainty defines the total uncertainty of each measurement.

$$\varepsilon = \sqrt{\xi^2 + \beta^2}$$

Where

ε = Total uncertainty based off 95% confidence level

ξ = Precision uncertainty based off 95% confidence level

β = Bias uncertainty